Effect of Alloy Composition on the Hot Deformation Behavior, Extrudability and Mechanical Properties of AA6XXX Aluminum Alloys

by

Daniel Oghenekewhe Odoh

A thesis
presented to the University of Waterloo
in fulfillment of the
thesis requirement for the degree of
Doctor of Philosophy
in
Mechanical & Mechatronics Engineering

Waterloo, Ontario, Canada, 2017

Examining Committee Membership

The following served on the examining committee of this thesis. The decision of the committee is by majority vote.

Supervisor(s)	Mary A. Wells PhD, P.Eng Professor, Mechanical & Mechatronics Engineering
	Michael J. Worswick PhD, P.Eng Professor, Mechanical & Mechatronics Engineering
External Examiner	Daolun Chen PhD, P.Eng Professor, Mechanical & Industrial Engineering Ryerson University
Internal Examiner	Kaan Inal PhD Associate Professor, Mechanical & Mechatronics Engineering
Internal Examiner	Adrian Gerlich PhD, P.Eng Associate Professor, Mechanical & Mechatronics Engineering
Internal External Examiner	Maria Anna Polak PhD, P.Eng Professor, Civil & Environmental Engineering

AUTHOR'S DECLARATION

This thesis consists of research which I authored or co-authored: see Statement of Contributions included in this thesis. This is a true copy of the thesis as accepted by my examiners. I understand that my thesis may be made electronically available to the public.

Statement of Contributions

The following have contributed to the current work:

Professor Mary Wells supervised this PhD thesis.

Professor Michael Worswick served as the co-supervisor.

Dr. Yahya Mahmoodkhani developed a Matlab code to predict the Mg-Si solute content in alloy 4 as a function of hold time and also performed finite element modeling of the extrusion using the commercial FE package Deform 2D using constitutive parameters obtained from the hot deformation compression flow stress curves.

The balance of this work is my own

Abstract

As automotive companies adjust to stricter environmental legislations, there is increased interest in the application of high specific strength alloys such as the AA6xxx aluminum alloys. In the near term, light weighting of vehicles through the use of high strength aluminum alloys is one solution to improve fuel efficiency. This research was performed to help understand the extrudability of some Al-Mg-Si alloys as well as the effect of extrusion conditions on final mechanical properties. The alloys studied were designed by General Motors (GM) and include variations in the Mg, Si and Cr contents. The research is primarily experimental in nature and consisted of measuring and modelling the hot flow stress behaviour of these alloys, performing both laboratory scale and industrial extrusion trials as well as mechanical and microstructural characterization of the extruded materials.

The well-known Sellars-Tegart model was applied in development of constitutive equations for predicting the hot flow stress behavior of Al-Mg-Si alloys. The influence of hold time on Mg-Si solute content level during pre-deformation heating of an as-cast and homogenized Al-Mg-Si alloy was determined and the Mg-Si solute content (X) integrated into a constitutive equation for predicting the alloy's flow stress behavior during hot compression testing. The constitutive model predictions were observed to agree well with experimental data for the aluminum alloys tested in this research.

The effect of extrusion processing condition, alloy composition and aging time on the extrudability, mechanical properties and fracture morphology as well as microstructure of Al-Mg-Si alloys was studied. The extrudability of the Al-Mg-Si alloys was observed to reduce with an increase in the Mg-Si content, presence of 0.2 wt % Cr and reduction in extrusion temperature. For laboratory extrusion trials, peripheral coarse grains were not observed in alloys

containing Cr and Mn. The strength property in the T4, T5 and T6 conditions was observed to increase with Mg-Si content while 0.2 wt % Cr addition favors improved ductility. The alloys containing Cr were observed to exhibit ductile dimple fracture and a transgranular morphology while an intergranular fracture was observed in the Al-Mg-Si alloys with no Cr content. The strain rate sensitivity and anisotropic behaviors of an Al-Mg-Si alloy were determined by performing quasi-static tensile test at 0.001, 0.01 and 0.1 s^{-1} on heat treated (T4 and T6) profiles extruded in industrial scale extrusion equipment. The T4 alloy samples were observed to exhibit reduced anisotropic behavior in comparison with T6 samples.

In this thesis, a more effective constitutive model for predicting the hot flow stress behavior of Al-Mg-Si alloys has been developed. The developed constitutive relation can be an effective tool for modeling forming processes such as extrusion and rolling, Also, a systematic through process (from extrusion processing to aging) investigation of the effect of alloy composition, extrusion and aging conditions on the final mechanical properties of Al-Mg-Si alloys has been performed.

Acknowledgments

"For I can do all things through Christ who strengthens me-Philippians 4:13"

Many thanks go to my supervisor, Professor Mary A. Wells who accepted to supervise my doctoral study. I am so grateful for the tutelage, encouragement and help. Her patience has taught me that all things can be achieved in the world of research with just a little more patience. I thank my co-supervisor, Professor Michael J. Worswick for the material and time resources put into my doctoral study.

I acknowledge the efforts of Dr. Yahya Mahmoodkhani who helped with the development of the Matlab code for Mg_2Si particle dissolution model as well as being a constant source of help throughout my doctoral study. Financial support provided by such organizations as Natural Sciences and Engineering Research Council of Canada (NSERC) and General Motors through the Automotive Partnership Canada network is greatly appreciated. Professor Inho Jung is acknowledged for providing phase fraction diagrams for the aluminum alloys studied in this research. The effort of Dr. Abhijit Brahme in providing answers to my many questions during the course of this study is acknowledged. The thesis committee members are also appreciated for agreeing to serve on my doctoral thesis team.

I am appreciative of the support provided by the staff of the department of Mechanical and Mechatronics engineering at the University of Waterloo who helped with machining of samples and providing needed technical support always. I am also thankful for group members and colleagues with whom I was opportune to hold many useful discussions.

Eternal gratitude is all I have for my parents who have given me all I ever needed in life even at their own inconvenience. To my brothers and sister: this is for you, you are always my backbone. I am grateful for the gift of my friend and partner – my wife who has always been my steady hand through life's journey. Finally, I am thankful to God for the most precious gift of all– my

son Nathan who has helped create a greater sense of responsibility in my life. This degree is your starting point son!

Dedication

To my parents

Table of Contents

List of Figures

List of Tables

List of Symbols

E_R – Extrusion ratio
V_{max} – Maximum extrusion speed (mm/s)
ε_c – Critical deformation strain
θ_c – Critical misorientation angle (^{o})
A – Material constant
σ – Flow stress (MPa)
n_1 – Stress exponent
$\dot{\varepsilon}$ – Strain rate (s^{-1})
α – Stress Multiplier (MPa^{-1})
Z – Zener Hollomon parameter
Q – Activation energy for hot deformation (kJ/mol)
σ_o – Flow stress at start of plastic flow (MPa)
n – Work hardening coefficient
ε_R – Transient strain
σ_{ss} – Steady state flow stress (MPa)
m – Strain rate sensitivity parameter
μ – Shear modulus (Pa)
K – Boltzmann constant (JK^{-1})
R – Universal gas constant (J/ mol. K)
b – Burger's vector
Q_D – Activation energy for self-diffusion (kJ/mol)
D_i – Temperature dependent diffusion coefficient (m^2/s)
C_i – Concentration of element i (wt %)
r – Distance from centre of dissolving particle (nm)
R_{al} – Radius of aluminum matrix cell (μm)
f_v – Volume fraction (vol. %)
r_o – Average initial Mg_2Si particle radius (nm)
k_o – Pre exponential factor
Q_{sol} – Activation energy for solubility (kJ/mol)
D_i^o – Diffusion parameter for element i (m^2/s)
k_1 – Material constant
k_2 – Material constant (wt. $\%^{-1}$)
X – Solute content
t –Time (Sec)
ε_p – Effective plastic strain
ε – Strain
σ_T – True stress (MPa)
E – Young modulus (N/m^2)
r_α – Flow stress ratio

σ_f^{α} – Flow stress ratio in α direction (MPa)

CHAPTER 1
Introduction

1.1 Aluminum alloys in automotive applications

The global oil crisis and increased concern about global warming are some of the reasons why manufacturers have begun to explore the possibility of reducing fuel consumption in automobiles [1]. The use of aluminum alloys in automobile applications has increased rapidly over the last 35 years due in part to efforts towards production of light weight and fuel efficient automobiles. Figure 1.1 shows the evolution of aluminum content in automobiles over the last 40 years.

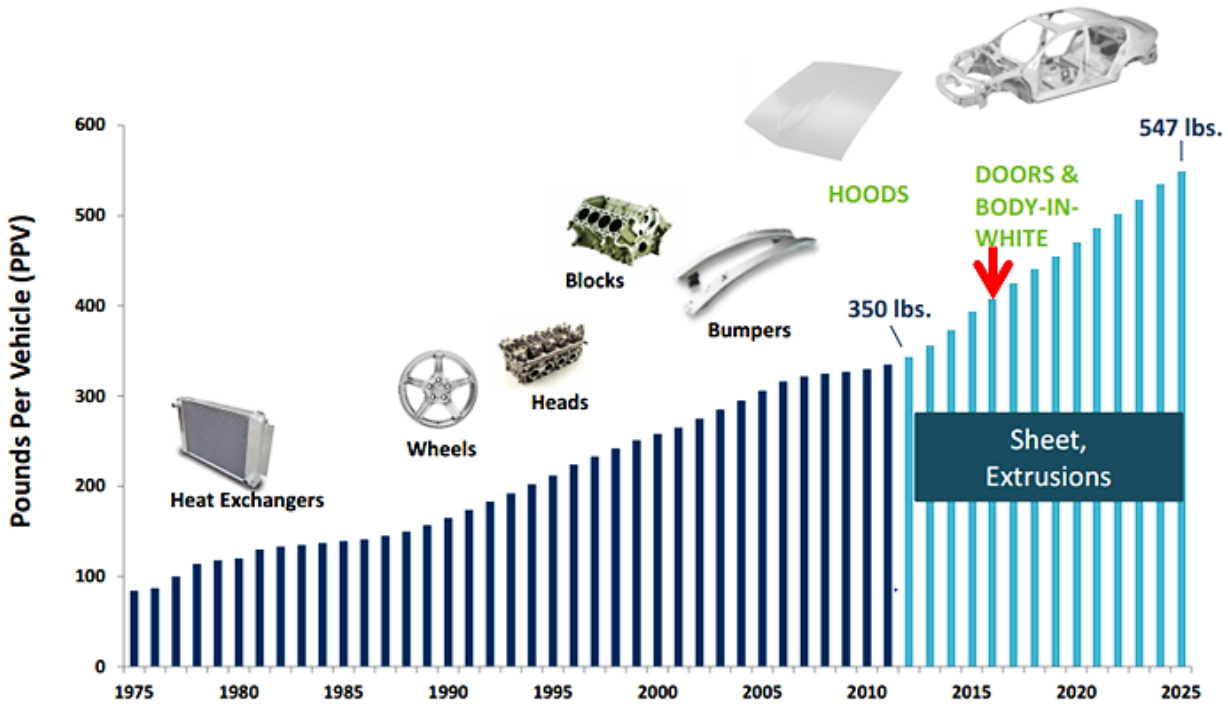

Figure 1.1: Evolution of aluminum content in European cars [2]

As seen in Figure 1.1, the use of aluminum and its alloys is expected to continue to grow in the automotive industry in the future as usage is projected to increase by about 40% over the next decade. Aluminum is a material of choice in the automobile industry due to its low density

(2.70g/cm^3) and excellent specific strength. Hence, aluminum can be considered a good replacement for mild steel (ρ = 7.75-8.05g/cm^3) in the design and production of light weight automobiles. The lower density and high specific strength of aluminum in comparison to mild steel can lead to weight savings of about 24 % in automobiles thus allowing for a reduction in fuel consumption by ~2 liters per 100 kilometers [3].

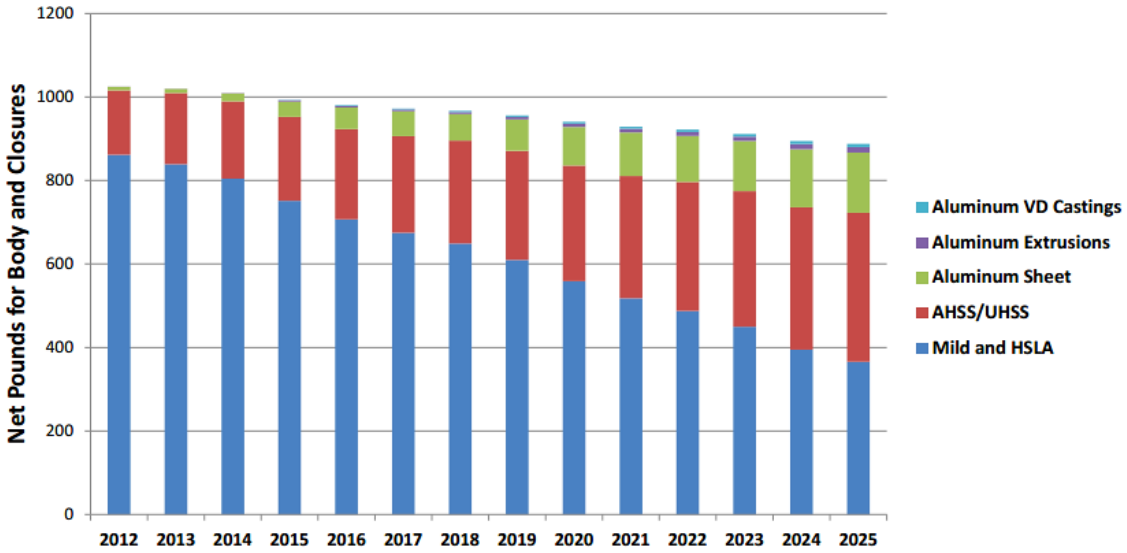

Figure 1.2: Projected trends in the usage of aluminum and steel for body and closure parts in automobiles [4]

The projected trend in the usage of aluminum and steel for automotive body and closure parts is shown in Figure 1.2. It is apparent that aluminum and its alloys will continue to gain approval in applications where steel has historically been the preferred material. As shown in Figure 1.2, aluminum usage is expected to grow in all forms: castings, sheet and extrusions. The alloys of aluminum are some of the most important commercially available metallic alloys used for a wide variety of automotive applications today. Such applications include: outer body panels, bumpers, vehicle chassis and suspension systems as well as the drive train [5-8]. Extrusion, rolling and casting are some of the manufacturing processes used for production of aluminum alloys.

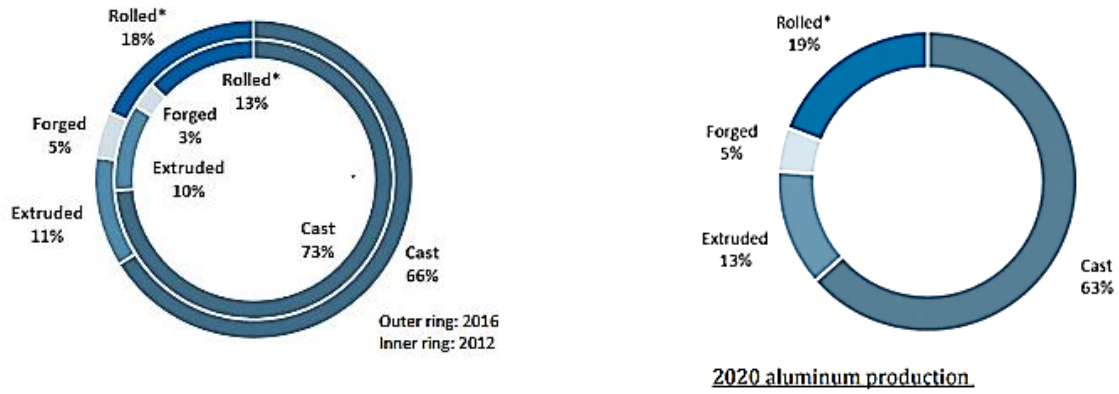

Figure 1.3: Processing method of aluminum alloys used for automotive application [9]

Figure 1.3 shows different manufacturing processes for aluminum alloys used for automotive applications. The use of extruded aluminum alloy in automobile applications is expected to increase within the next 4 years. Figure 1.4 shows typical locations where different aluminum alloy products are used in an automotive structure.

Figure 1.4: Frame of F150 showing parts manufactured with processed aluminum [10]

General Motors (GM), one of the leading manufacturers in the automobile industry is interested in the development of metals and alloys that have improved crash and impact resistance properties and high specific strength while also satisfying light weighting requirements. The development of such materials is central to GM's strategic plan to be the global leader in the

production of fuel efficient and cost effective automobiles. This research is part of a larger collaborative research project funded through NSERC's Automotive Partnership Program (APC) entitled: "High strength high crush efficiency extruded aluminum front rails for lightweight bodies". The research project team includes groups from SAPA Canada, the Universities of Waterloo, McGill, McMaster and Sherbrooke with the responsibility of developing an optimized aluminum front rail profile that satisfies crashworthiness criterion, extrusion requirements and light weighting demands. The major objectives include but are not limited to designing of optimum front rail geometry, alloy composition development and manufacturing route design for the new AA6xxx extrusion alloys. Key aspects of this research include elemental composition design and casting of the AA6xxx alloys, determination of suitable homogenization condition as well as understanding the influence of alloy composition, extrusion parameters and subsequent age hardening on the resulting microstructure and mechanical properties of the extruded profiles.

1.2 AA6xxx aluminum alloys

The mechanical properties of the various alloys of aluminum are a function of the elements present and their amounts within the alloy. A number of major alloying elements such as Mg, Mn, Si, Cu and Zn are added to aluminum in commercial alloys [11-13]. Table 1.1 shows the major alloying elements as well as tensile properties of some well-known wrought aluminum alloys.

Table 1.1 Composition and properties of aluminum alloy series [14]

Alloy Designation	1xxx (Al)	3xxx (Al-Mn)	5xxx (Al-Mg-Cr)	6xxx (Al-Mg-Si)	7xxx (Al-Zn-Mg)	2xxx (Al-Cu)
Typical alloy	1050	3004	5083-H116	6063-T6	7075-T6	2024-T4
Ultimate tensile Strength (UTS) (MPa)	110	215	317	241	572	469
Elongation (%)	12	10	12	18	3	5
Yield strength (MPa)	105	172	228	214	503	324

As seen in Table 1.1, AA6xxx alloys have lower strength than typical AA7xxx and AA2xxx alloys but find wide application due to their high corrosion resistance, good formability and machinability. The AA6xxx series alloys are referred to as medium to high strength, heat treatable and age-hardenable aluminum alloy series [5]. Some properties that make AA6xxx alloys useful in the automobile industry include: high strength to weight ratio (ensures fuel economy as well as ease in design and production of crashworthy but light structural components), high electrical and thermal conductivity potential [5, 7, 14-15]. AA6xxx alloys contain Mg and Si as major alloying elements and gain their strength through precipitation of Mg-Si-phases during age hardening treatment. These alloying elements are included up to about 0.2-1.5 weight % (% wt.) and combine to form Mg_2Si particles which are the primary hardening phase in the alloy series [5, 16]. These Mg_2Si phases impart hardening by precipitating out in the alloy matrix through a process called precipitation hardening. The Mg and Si content of AA6xxx alloys usually determines the level of precipitation strengthening during the age hardening process. Figure 1.5 shows the range of Mg and Si in some AA6xxx alloys.

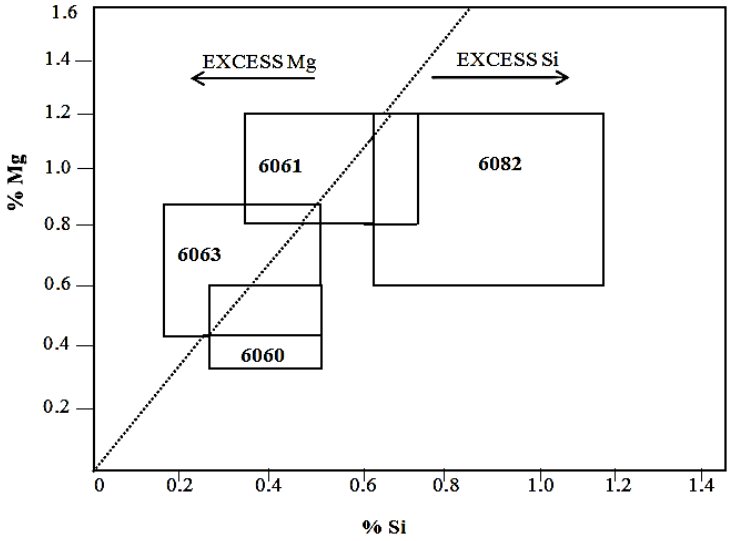

Figure 1.5: Mg/Si ratio of some 6xxx series alloys [17]

The Mg_2Si precipitates and constituent Fe containing particles present in these alloys have a strong influence on their mechanical properties [14]. Table 1.2 shows the mechanical properties and application as well as the maximum Mg and Si content of some AA6xxx alloys.

Table 1.2: Composition, strength and application of select 6xxx alloys

Alloy (Composition by % weight)	**Yield (MPa)**	**Application**
AA6060-T6 (0.35-0.6Mg, 0.3-0.6 Si)	150	Used for production of automobile doors and windows
AA6061-T6 (0.8-1.2 Mg, 0.4-0.8 Si)	276	Finds application in the manufacture of automotive parts such as wheel spacers
AA6063-T6 (0.45 - 0.9 Mg, 0.2 - 0.6 Si)	214	For the manufacture of automobile front rails due to high extrudability
AA6082 (0.6 - 1.2 Mg, 0.7 - 1.3 Si)	250	Used for structural parts in cars

Silicon addition contributes to the strength by precipitation of Mg_2Si precipitates; however, it also results in a reduction of ductility [13]. Copper when present in aluminum alloys is an important alloying element due to its appreciable solubility, strengthening effect and improvement of alloy aging response without a detrimental effect to toughness [11, 13]. Iron combines with Si in aluminum to form intermetallics such as α and β- AlFeSi. Transition elements such as chromium and manganese when present in AA6xxx alloys help to reduce the embrittling effect of excess silicon by incorporating the Si in dispersoid particles and therefore increase the alloy toughness [13]. They also help to suppress recrystallization by forming dispersoids that pin grain boundaries and promote formation of a fibrous grain structure. The dispersoids are usually formed during high temperature homogenization of AA6xxx alloys. When present in small particle sizes, dispersoids are known to allow for homogenous distribution of dislocations therefore reducing the number of possible nucleation sites for recrystallized grains [18]. It is noted that the type of iron rich phases present in aluminum alloys depend on

the presence of manganese and chromium [13]. In AA6xxx alloys where manganese and chromium are not present, Fe_3SiAl_{12} and Fe_2SiAl_9 are usually the iron-rich phases present. In contrast, when manganese and chromium are present they stabilize the $(Fe, Mn, Cr)_3SiAl_{12}$ phase [11].

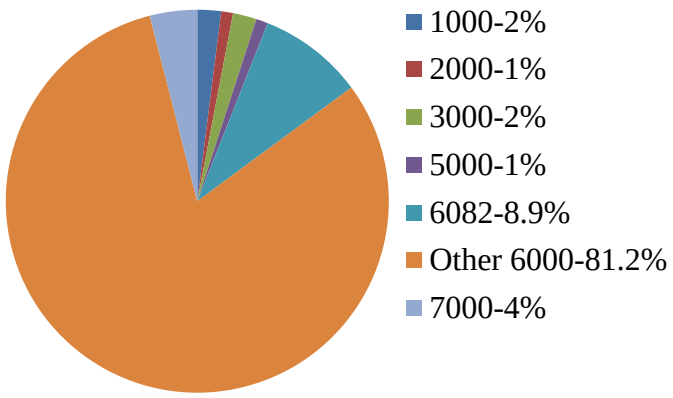

Figure 1.6: Aluminum alloys used for extrusion [19]

AA6xxx alloys are some of the most widely used in the manufacture of extruded products due to their ease of extrusion, relative low cost, versatility, superior surface finish quality and strength [20-22]. Figure 1.6 shows that approximately 90% of extruded profiles are made from AA6xxx aluminum alloys.

1.3 Manufacturing process for extruded AA6xxx alloys

The manufacturing of extruded AA6xxx alloys is a multi-step process that involves traditional direct chill (DC) casting of a billet followed by homogenization, extrusion and then post extrusion heat treatment as well as other finishing operations. The final mechanical properties of the extruded profile are a function of each stage of the manufacturing process; therefore great attention is required in performing and understanding the linkages and dependencies of these processes. The manufacturing process used to produce extruded AA6xxx aluminum profiles is shown in Figure 1.7.

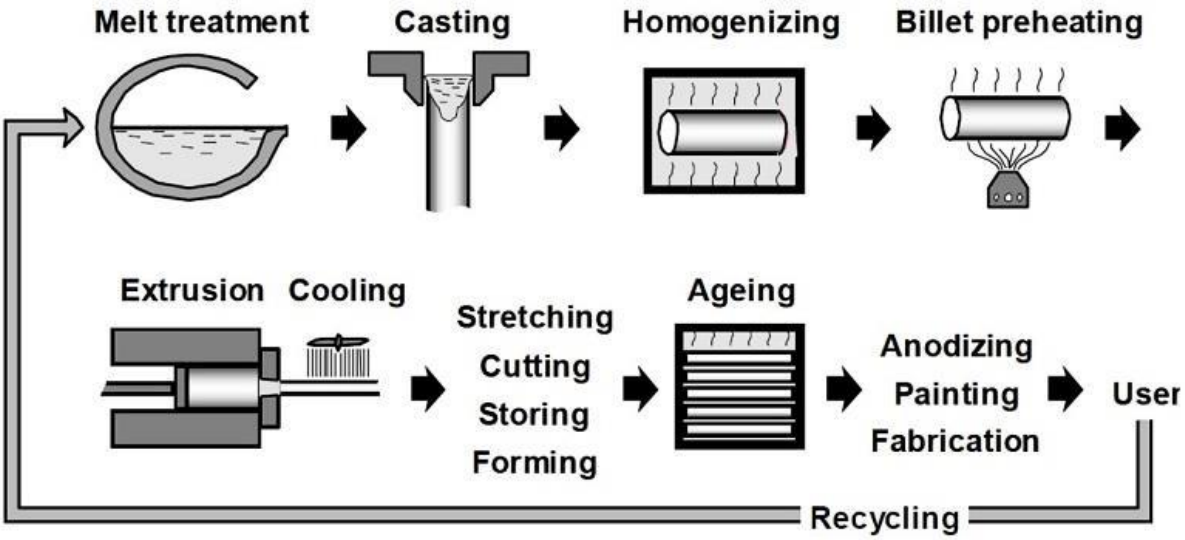

Figure 1.7: Manufacturing process of extruded AA6xxx aluminum alloys [23]

Prior to the extrusion process, the material is subjected to casting, homogenization and pre-heating to the extrusion temperature. These processes have been reported to influence the microstructure of aluminum alloys [24]. Figure 1.8 shows the microstructure changes that occur during manufacturing process of extruded AA6063 alloy.

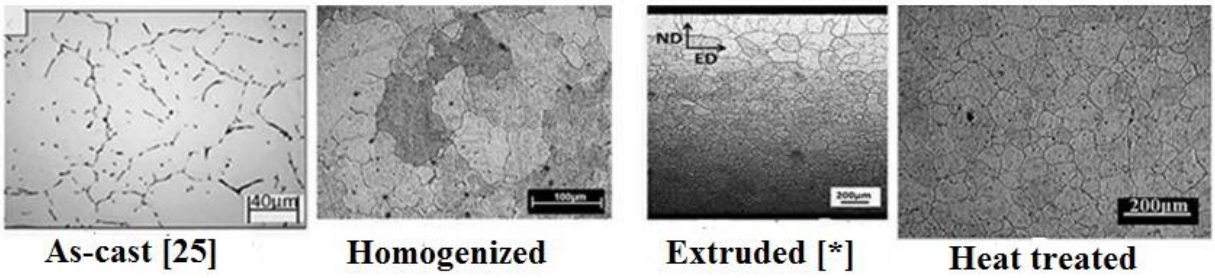

Figure 1.8: Microstructure changes during manufacturing process of extruded AA6063 alloy
[*] – Provided by Julie Levesque

Microsegregation of atoms and concentration gradients of Mg and Si which result during the casting process are usually mitigated by the homogenization process. After homogenization, the billets are rapidly heated to the extrusion temperature and then extruded. Cooling after extrusion can be quite important especially in quench sensitive AA6xxx grades where solute may precipitate out if the cooling rates are not fast enough [7]. Typically, the extruded profiles are

stretched out to remove curving and waving created as the extrudate exits the die. The profiles may then be solutionized and naturally aged to T4 temper condition. Natural aging is a step that involves allowing the extruded profile to gain its full strength at room temperature. The profiles may otherwise be solutionized and subsequently heat treated through an artificial aging process to T6 condition in order to achieve desired maximum mechanical properties. Artificial aging is an heat treatment procedure that involves heating the extrusions in an oven in the temperature range 170-190 ^{o}C for 4 to 8 hours [24]. The alloy profiles are designated as being in T5 condition if extruded and artificially aged without solutionizing.

1.4. Thesis Outline

In chapter 2, the current state of knowledge on the hot deformation behavior of Al-Mg-Si alloys as well as present understanding of the effect of processing parameters on the mechanical properties and fracture behavior of these alloys are presented. Empirical and physical based models available in the literature for predicting the hot deformation flow stress behavior of aluminum alloys are also discussed. The specific objectives of the research performed as the central theme of this thesis are identified in chapter 3. Chapter 4 presents the detailed methodology (experiment and modeling approach) implemented in order to achieve the identified objectives. The results obtained are presented and discussed in chapters 5. Each of the sections in the result chapter is either published work, under peer review or soon to be submitted for publication consideration. The summary of major contributions to knowledge, conclusion and future work are discussed in chapter 6.

CHAPTER 2
Literature review

This chapter summarizes the current state of knowledge on the extrusion of AA6xxx aluminum alloys, constitutive modeling of the hot deformation behavior of these alloys as well as the effect of alloy composition on their hot deformation behavior. Research efforts towards understanding the effects of alloy composition, extrusion and aging conditions on the mechanical properties of extruded AA6xxx alloys are also highlighted. Knowledge gaps within the subject of extrusion manufacturing process as well as hot deformation behavior of AA6xxx aluminum alloys are identified.

Manufacturing of AA6xxx extrusion involves multiple processing steps. It is important that the effects of the various extrusion process parameters are adequately understood in order to be able to optimize the desired properties of the final product. Figure 2.1 shows a typical thermo-mechanical processing history for extrusion of AA6xxx aluminum alloys.

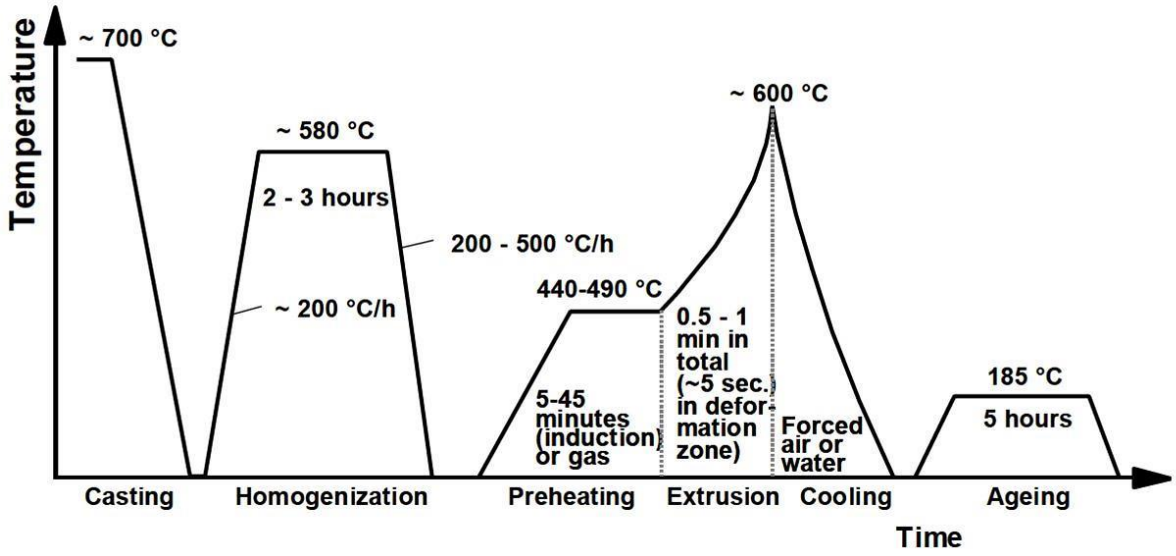

Figure 2.1: Typical thermo-mechanical processing history of AA6xxx aluminum alloys during extrusion process [23]

During the direct chill (DC) casting process, the molten metal is poured from the holding furnace into a hollow mold section where it is allowed to cool by conduction through the walls of the mold and then exposed to water cooling as the surface of the billet exits the mold [23]. Al-Mg-Si alloys containing Mg and Si as the major alloying elements can be considered as two phase alloys in which one phase is the Al matrix and the second phase comprises Fe-rich AlFeSi particles. The microstructure of the as-cast billet is usually characterized by the presence of micro-segregated regions and concentration gradients of Mg and Si. The insoluble Fe in Al-Mg-Si alloys combines with Si and Al to form metastable Al-Fe and β-AlFeSi intermetallic second phase particles in the as-cast alloy microstructure [26, 27].

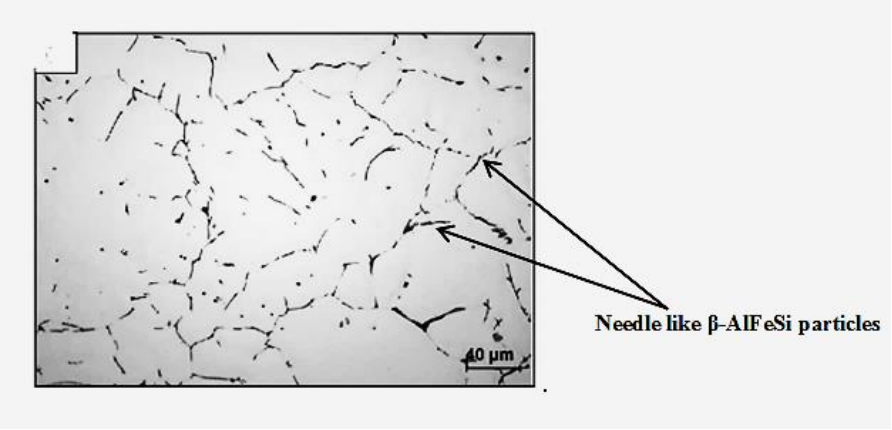

Figure 2.2: Microstructure of the as-cast AA6063 alloy [25]

Figure 2.2 shows second phase intermetallic β-AlFeSi particles present along grain boundaries in as-cast AA6063 aluminum alloy. These metastable compounds and the microsegregation formed during the solidification of cast AA6063 aluminum alloy have an adverse effect on the extrudability of the alloy due to low formability resulting from microsegregation and grain boundary segregation [25, 28]. The unstable monoclinic β-AlFeSi particles are present in a well-defined interdendritic network and as solute segregation in the intergranular spacing and grain boundaries. These β-AlFeSi intermetallic particles are non-uniformly distributed within the alloy

matrix. It is therefore required to convert the unstable monoclinic β-AlFeSi intermetallic particles to the more stable α-AlFeSi particles that have no detrimental effects on the extrudability of the alloy. On the whole, AA6xxx alloys are precipitation hardened alloys whose strength and formability properties can be improved through methods such as homogenization and aging processes [26].

Homogenization is a heat treatment procedure performed on as-cast aluminum alloy billets and is designed to reduce the microsegregation of Mg and Si as well as transform the majority of the β-AlFeSi into α-AlFeSi [29]. The process results in a homogenized matrix with a balanced distribution of the various Al-Fe-Si compounds [30]. Particular difficulty in obtaining suitable structures is encountered in alloys having higher Si content since this element increases the relative stability of the β-phase. The homogenization of Al-Mg-Si alloys has been divided into 3 steps that include heating, holding and cooling. Various microstructural changes have been reported to occur during these three stages [31]. The microstructural changes during the homogenization of Al-Mg-Si alloys are summarized in Figure 2.3.

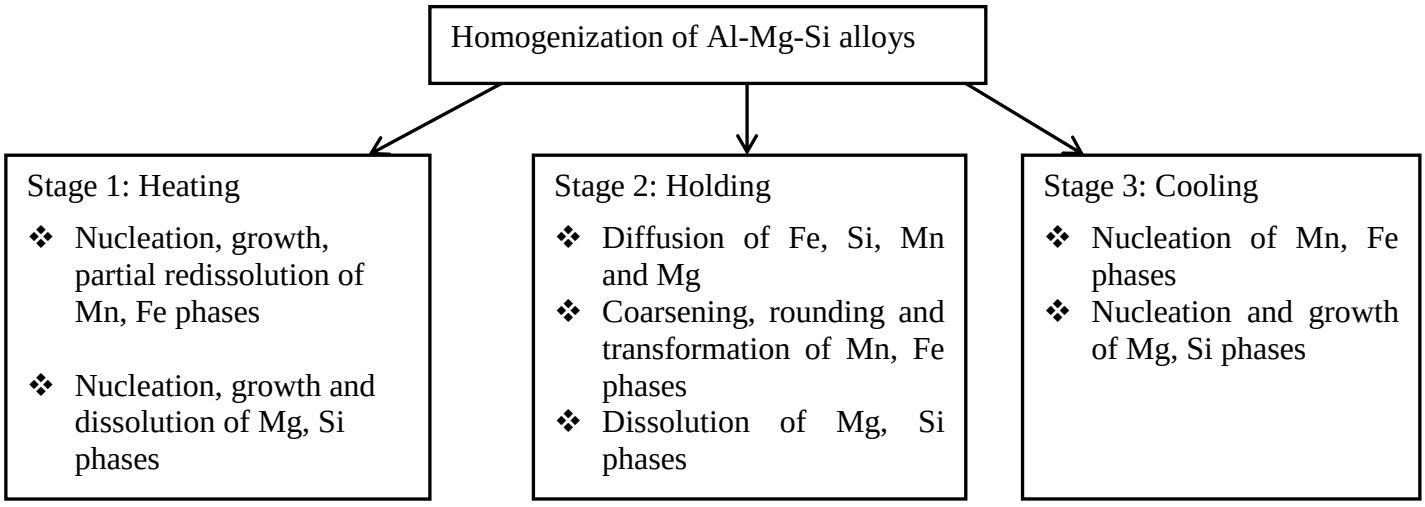

Figure 2.3: Microstructural changes during the homogenization of Al-Mg-Si alloys [31]

Figure 2.4: Optical microstructure of homogenized AA6063 aluminum alloy [30]

Figure 2.4 shows the microstructure of AA6063 aluminum alloy after homogenization at 600^{o}C for 6 hours upon which the Mg and Si phases that nucleate and grow during the cooling stage of homogenization become uniformly distributed throughout the alloy matrix.

2.1 Extrusion of AA6xxx alloys

Extrusion is a plastic deformation process in which a volume of metal (billet) is forced to flow by compression through a die with an opening of smaller cross-sectional area than that of the original billet [32]. The advantages of extrusion as a manufacturing process include: the ability to produce complex thin walled and hollow sections (with high geometric tolerances) that are otherwise difficult to produce by other manufacturing processes and the ability of the manufacturer to control the process through which materials with good surface finish are produced. Factors that affect the microstructure and mechanical properties of extruded profiles include: the extrusion (ram) speed, temperature, extrusion ratio as well as the alloy starting microstructure and composition.

The extrusion speed is the velocity of travel of the ram and this is a major factor that dictates the strain rate experienced by the material during the deformation process. The extrusion speed has been observed to have an influence on the final microstructure and mechanical properties of the extrudate [33, 34]. Zhao et al. [34] observed large and inhomogeneous grain

structures in AA6063 profiles extruded at velocities of 0.1m/s and 0.14m/s (Figures 2.5A and B respectively).

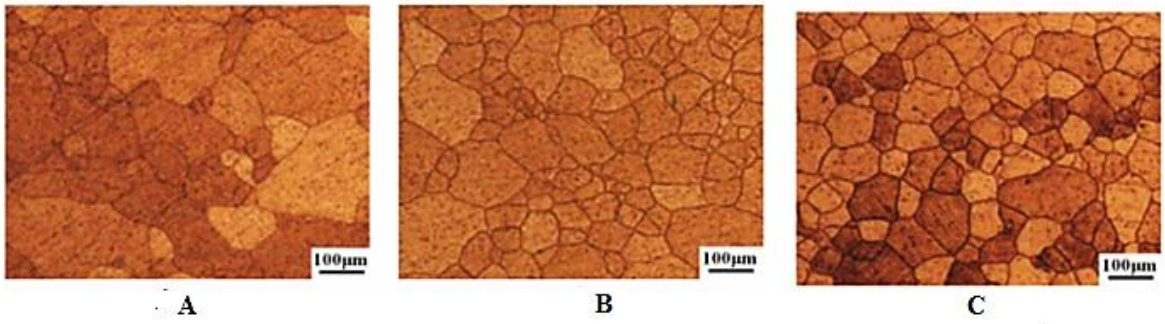

Figure 2.5: Final microstructure of 6063 aluminum extrudate at different extrusion velocities A): 0.1m/s B): 0.14m/s C): 0.18m/s [34]

As seen in Figure 2.5C, the sample extruded at 0.18 m/s was observed to exhibit a fine and uniform grain structure. An increase in the extrusion speed was reported to result in increased strain rate experienced by the material during the deformation process – a condition favorable for the formation of a finer grain structure. Aytac et al. [35] measured the effect of extrusion speed on the hardness of aged AA6063 alloy. The aged (T5) samples extruded at 3 mm/s and 6 mm/s were reported to have average hardness values of 74 HV and 83 HV respectively. Parson et al. [36] studied the influence of ram speed and billet temperature on the microstructure of extruded AA6005A aluminum alloy.

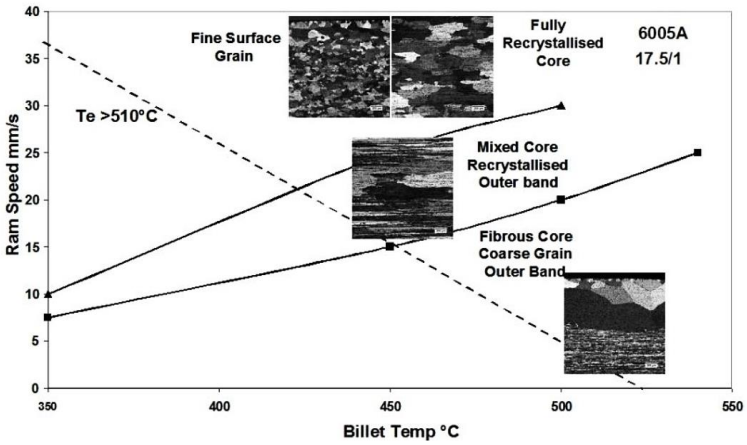

Figure 2.6: Influence of ram speed and billet temperature on the microstructure of extruded AA6005A alloy [36]

Figure 2.6 shows that a fine grain structure is promoted at billet temperatures of 420-480 ^{o}C and ram speeds ranging between 30 and 40mm/s. However, it was observed that high billet temperatures above 500 ^{o}C and low ram speed are suitable conditions for formation of an unrecrystallized microstructure. High ram speed (30-40 mm/s) and temperatures above 450 ^{o}C were reported to be favorable for formation of a fully recrystallized microstructure within the core of the extruded AA6005A alloy. Exit temperatures above 510 ^{o}C were observed to be sufficient enough for dissolution of Mg_2Si particles needed to ensure attainment of T6 strength requirements. Ishikawa et al. [37] studied the effect of extrusion speed on the microstructure of an Al-Mg-Si-Zn alloy. The central section of samples extruded at 1.5 mm/s were observed to exhibit a fibrous grain structure while samples extruded at 3 mm/s exhibited a recrystallized structure in the centre location. An increase in the extrusion speed was observed to promote occurrence of recrystallization due to an increase in deformation strain rate. Similarly, Sweet et al. [38] reported that an increase in the extrusion speed from 25 m/min to 30 m/min promotes the formation of finer recrystallized grains in the sub-surface regions and more complete recrystallization in the centre of extruded AA6061 alloy. The increase in extrusion speed was observed to result in higher deformation strain rate and thus higher stored energy – a major driving force for recrystallization.

The extrusion temperature has been observed to influence the mechanical properties of extruded Al-Mg-Si alloys. Ihara et al. [39] reported that the tensile strength of AA6005C aluminum alloy increases from 266 MPa to 278 MPa with an increase in the extrusion temperature from 480 to 520 ^{o}C. The increase was reported to be due to reduction in accumulation of strain energy in un-recrystallized zones with increasing extrusion temperature. The average recrystallized grain size of the extruded AA6005C alloy was found to increase from

165µm to 234µm when the extrusion temperature was reduced from 520 ^{o}C to 480 ^{o}C. Bryant [40] observed an increase in the yield strength and decrease in the toughness of extruded Al-Mg-Si alloy with increasing extrusion temperature. The alloy toughness was observed to drop from 800 J/m^3 to 160 J/m^3 while the yield strength increased from 270 MPa to 324 MPa with an increase in the extrusion temperature from 450 ^{o}C to 560 ^{o}C. It was reported that an increase in extrusion temperature favours increased equilibrium solubility of Mg_2Si.

The extrusion ratio E_R (defined as the ratio of the cross-sectional area of the upset billet to that of the extruded metal) has been identified as another factor affecting the extrusion process and properties of the extruded profile. During the extrusion of AA6082 alloy, Sweet et al. [38] reported that increased extrusion ratio above E_R =16 ensures attainment of critical stored energy required to obtain a fine recrystallized grain structure. An increase in the number of active nucleation sites was reported with increased E_R and hence higher stored energy. Karabay et al. [41] investigated the effect of extrusion ratio on the mechanical behavior of extruded AA6063 aluminum alloy. As seen in Figure 2.7, they observed that increased extrusion ratio results in an increase in hardness and decrease in elongation of extruded AA6063-T6 alloy.

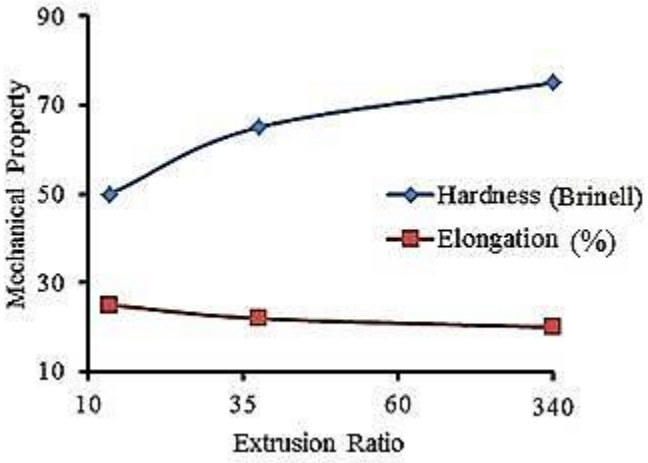

Figure 2.7: Effect of extrusion ratio on mechanical properties of AA6063 aluminum alloy [41]

An increase in the extrusion ratio was observed to favour formation of refined grain structure containing a large amount of fine new grains at initial grain boundaries. This refined grain structure due to increase in extrusion ratio was reported to be responsible for some increased strengthening in the AA6063 alloy. Demirci and Evlen [42] observed an increase in ultimate tensile strength (UTS) (from 150 to 188 MPa) and reduction in ductility (7.65 to 6.8 %) of an Al-Si alloy extruded at 350 ^{o}C when the extrusion ratio E_R is increased from 1.6 to 2. An increase in extrusion ratio was observed to favour a finer grain structure that promotes some strengthening.

The elements present in Al-Mg-Si alloys have been reported to influence the extrudability of these alloys [5, 19, 43]. Mg and Si when present in excess of that required to form Mg_2Si precipitates have been reported to influence the extrudability of Al-Mg-Si alloys [19]. Petrovic and Jensrud [43] reported an increase in the extrusion force from 3.4 MN to 3.6 MN required to extrude an Al-Mg-Si alloy when the Si content is increased from 3.7 to 5.51 wt. %. The retention of silicon in solution was observed to result in an increase in deformation resistance and therefore increased pressure required for extrusion. Langerweger [44] observed a drop in the extrudability of Al-Mg-Si alloy when the Si content is in excess of that required to form Mg_2Si particles. Reiso [19] studied the influence of Mg and Si on the maximum extrusion speed before tearing occurs on the surface of an Al-Mg-Si extruded profile. It was observed that the extrudability of the AA6xxx alloys is strongly affected by the alloy composition. Figure 2.8 shows the effect of Mg and Si on the maximum extrusion speed before tearing occurs on the surface of an extruded Al-Mg-Si alloy. Figure 2.8A shows that extrudability V (m/min) of the Al-Mg-Si alloy is reduced by 1-2% per 0.01 wt. % Si content. From Figure 2.8B, it is observed that Mg content above approximately 0.55 wt. % actually has a detrimental effect on the extrudability (sharp drop in maximum speed) of the AA6063 aluminum alloy [19].

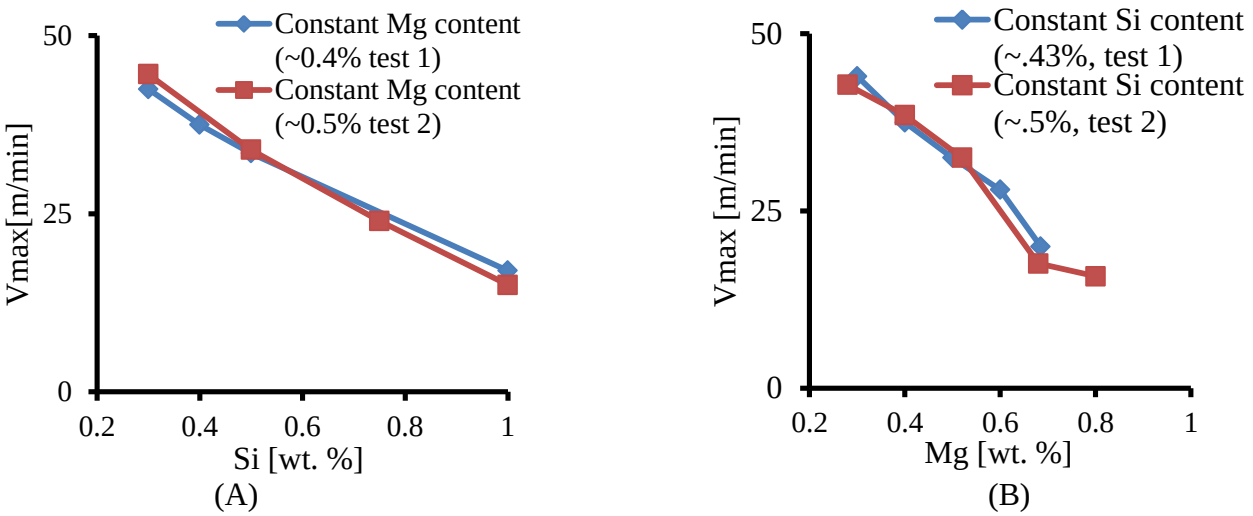

Figure 2.8: Influence of composition on extrudability of Al-Mg-Si alloy (A): Si content, (B) Mg content [19]

As seen in Figure 2.9, Zhu et al. [6] reported that Mg and Si dissolved in solid solution usually have a strong influence on alloy flow stress during extrusion. It was suggested that increased amounts of Mg and Si in solution increase the flow stress and deformation resistance during extrusion.

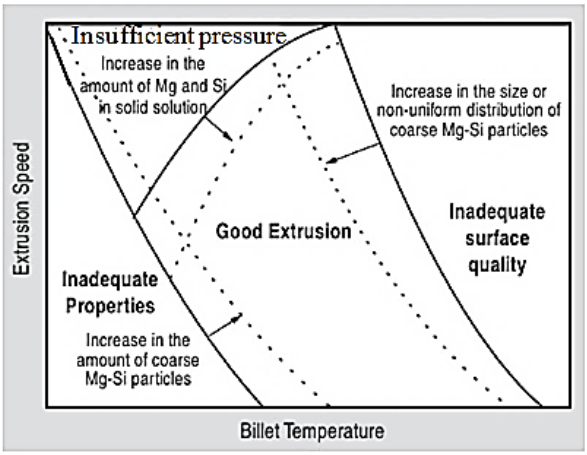

Figure 2.9: Effect of Mg-Si particles on extrusion limit diagram [6]

Evangelista et al. [45] reported an 8 % increase in the pressure required to extrude an Al-Mg-Si alloy for every 0.1 wt % increase in Mg_2Si in solid solution. Lang and Castle [46] determined the influence of Mn, Cu and Cr on the initial load required to extrude an Al-Mg-Si alloy.

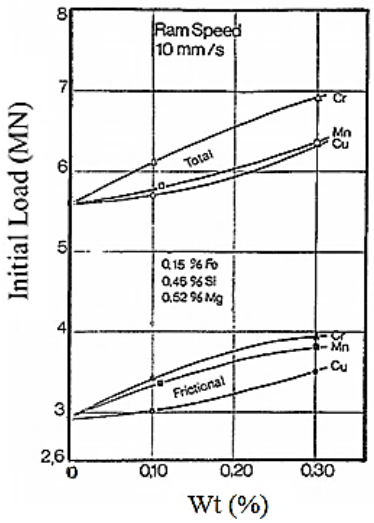

Figure 2.10: Influence of Cu, Mn and Cr on the initial and frictionless loads required to extrude an Al-Mg-Si alloy [46]

As seen in Figure 2.10, the extrusion load required to extrude the Al-Mg-Si alloy was observed to increase with an increase in the Cu, Mn and Cr content. Cr addition was reported to have the highest influence on the alloy's extrudability due to the interactions between Cr and Fe atoms to form Cr containing dispersoids. Zajac et al. [47] studied the influence of 0.08 wt. % Mn addition on the extrudability of AA6005 alloy. The Mn addition was observed to be responsible for the conversion of highly elongated β-AlFeSi rods to smaller α spheriodized intermetallics. The elimination of high density dislocation cells at the β rods was reported to result into reduction in strain hardening rate and a 20 % reduction in the pressure required to extrude the alloy. Transition elements such as Cr, Mn and Zr have been reported to suppress recrystallization in extruded aluminum alloys by pinning grain boundaries and promoting a fibrous grain structure [48]. Meng et al. [48] studied the effect of Zr on the as-extruded microstructure of Al-Mg-Si alloy. The extruded profiles with no Zr content were observed to exhibit a recrystallized grain structure while samples containing 0.15 wt % Zr were reported to exhibit a completely fibrous microstructure. Al_3Zr phases present in the extruded alloy containing Zr were reported to impede nucleation and growth of recrystallized grains by hindering formation and migration of grain

boundaries. Guemini et al. [49] reported a relatively high recrystallization temperature for hot rolled Al-Mg-Si alloys containing Zr, Mn and Mn + Cr dispersoids. The shift of recrystallization to higher annealing temperatures in the Al-Mg-Si alloys was linked to the presence of these dispersoids that inhibit recrystallization through their drag effect on grain boundaries and pinning of subgrain boundaries.

2.2 Microstructural changes during hot deformation of aluminum alloys

Microstructural changes have been reported to occur during the hot deformation of aluminum alloys. Some of these microstructural changes include: dynamic precipitation [50, 51], dynamic recovery [52] and dynamic recrystallization [48, 53-57].

Dynamic Precipitation

Dynamic precipitation (DP) has been reported to be similar to static precipitation hardening in aluminum alloys [50, 51]. The presence of large amount of very fine Q precipitate phases that impede dislocation motion was confirmed in AA6061 samples deformed at 400 ^{o}C to a strain of 1.2. The flow stress was reported to increase until a peak value is reached. However, particle coarsening was observed with continued straining resulting in reduction in the flow stress. Fan et al. [50] reported that dynamic precipitation is a temperature dependent phenomenon as precipitation of Q phases was confirmed in samples deformed at 400 ^{o}C but only the presence of rod like Si particles and intermetallics was confirmed in samples deformed at 500 ^{o}C. The Q-phase precipitates were reported to impede dislocation motion resulting in an increase in flow stress to a peak value. However, a drop in effect of precipitate hardening was observed with continued straining due to particle coarsening.

Dynamic Recovery

The high stacking fault energy (SFE) of aluminum alloys ensure that dislocation climb and cross slip readily occur during the hot deformation of these alloys [51]. The dynamic

recovery process has been reported to be the only form of dynamic restoration which occurs in aluminum alloys [53, 58]. The dynamic recovery process is a restorative mechanism that involves reduction in stored energy of the deformed grains by removal/rearrangement of dislocation defects. During the initial stages of deformation up to the yield point, dislocation interactions and multiplication are known to occur. Dislocations are arranged within subgrains aligned in planes of high shear stress. The stress-strain curve of a dynamically recovered alloy is usually characterized by an increase in flow stress up to a plateau followed by a constant steady flow stress [52]. At a specific strain, dynamic equilibrium is reached between the work hardening and dynamic recovery rates resulting into a constant dislocation density characterized by a steady state flow stress [52].

Dynamic recrystallization

Classical or discontinuous dynamic recrystallization (DDRX) involves the nucleation and growth of new grains which originate at old grain boundaries [52, 59, 60]. With increased material deformation, the driving force for increased growth of the recrystallized grains increases as their dislocation density increases. DDRX has been reported to occur in high purity aluminum and aluminum alloys containing large particles [52].

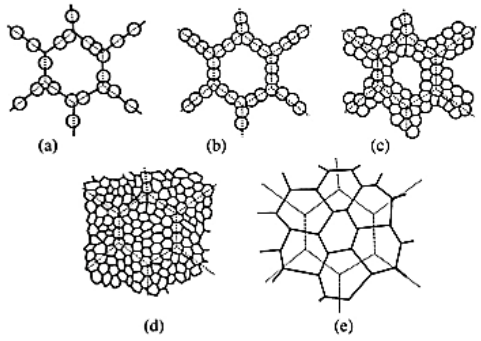

Figure 2.11: Microstructural development during DDRX (a) – (d): Large initial grains, (e) small initial grains [52]

However, DDRX has been observed to be more prominent in metals with low SFE where the dynamic recovery process is very slow [52, 61, 62]. The development of microstructure during DDRX is shown in Figure 2.11. This involves the nucleation of new grains and growth of dislocation depleted regions at the expense of dislocation filled regions. The stress-strain curves of dynamically recrystallized materials exhibit a broad peak which signifies the onset of dynamic recrystallization after attainment of a critical deformation ε_c [52]. Variations of classical DRX such as continuous dynamic recrystallization (CDRX) and geometric dynamic recrystallization (GDRX) have been reported to occur in aluminum alloys [52, 60, 63].

Continuous dynamic recrystallization involves the transformation of low angle boundaries into high angle boundaries during the deformation of a material [52, 60]. This transformation occurs due to progressive accumulation of dislocations within low angle boundaries resulting into an increase in their misorientation angle until critical misorientation angle $\theta_C = 15^o$ is reached [58]. Pedrix et al. [56] were the first to report the occurrence of CDRX in commercial purity (1050 grade) aluminum that was deformed in a torsion experiment. CDRX process has been reported to occur due to three mechanisms [60]. These mechanisms include: formation of subgrain boundaries with low misorientation angles (usually about 1^o), transformation of subgrain boundaries into grain boundaries and elimination of subgrain and grain boundaries.

Geometric dynamic recrystallization during hot deformation has been reported to involve flattening (during compression) or elongation (torsion or tension test) of original grains with progressive serration of grain boundaries during the formation of subgrains [52, 60]. The grain boundary area per unit volume continues to grow with increased straining such that there is an increase in the fraction of subgrain facets formed from the initial grain boundaries. Once the

original grain thickness reduces to about 2 subgrain size, grain boundaries contact each other causing grains to pinch off [64]. Figure 2.12 shows the progression of formation of GDRX with increasing strain.

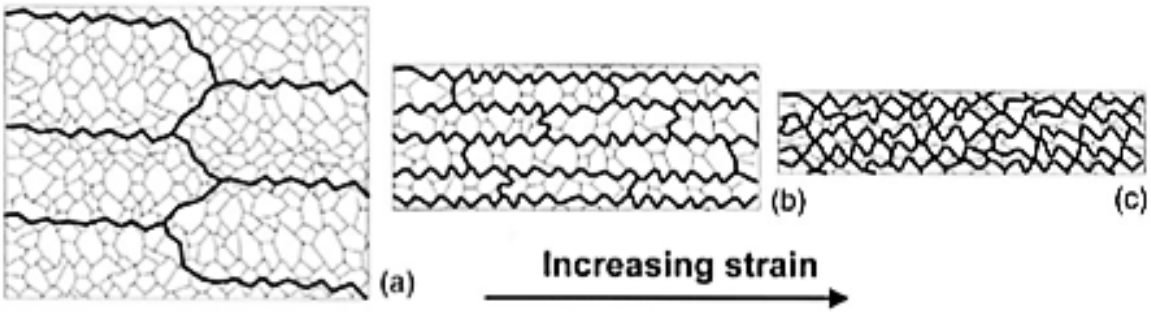

Figure 2.12: Geometric recrystallization (a): Serrated high angle grain boundaries (HAGB) formed during recovery shown in black, flattening of original grains occur, (b): Increase in HAGB with increased deformation and size of grain boundary serrations become comparable to grain thickness, (c): Interpenetration of scalloped boundaries resulting in formation of small equiaxed grains with size comparable to subgrain size [52]

During high temperature hot rolling of AA6082 at 450 ^{o}C and 550 ^{o}C, Poletti et al. [65] confirmed the occurrence of GDRX at small critical strain of 0.6 (450 ^{o}C) and 0.5 (550 ^{o}C). The microstructure of the hot rolled recrystallized material (inverse pole images shown in Figure 2.13) was characterized by the presence of large amount of HAGB, pinching off and grain refinement.

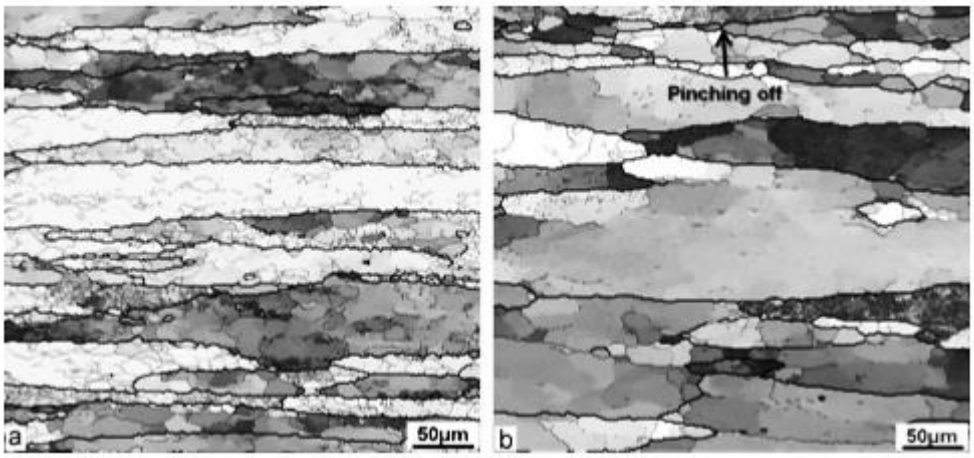

Figure 2.13: Inverse pole figure of hot rolled recrystallized samples (AA6082HR-Rex) deformed at 0.1s^{-1} (a) 450 ^{o}C and (b) 550^{o}C [65]

2.3 Constitutive modeling of hot deformation behaviour of aluminum alloys

Knowledge of the flow stress behavior of AA6xxx aluminum alloys during hot deformation process is important in order to effectively model and understand the behavior of these alloys during manufacturing processes such as extrusion and hot rolling. AA6xxx alloys experience a wide range of strains, strain rate and temperature during extrusion process. During the extrusion process, deformation temperature can vary from 400 ^{o}C to about 600 ^{o}C with strain rates reaching 30s^{-1} depending on the alloy type [66]. Several empirical constitutive relationships and physically based models have been reported in the literature for the prediction of the steady state flow stress behavior of metals over a set of strain rates and temperatures [66, 67].

Empirical models for hot deformation behavior of 6xxx series alloys

Constitutive equations used for predicting the hot deformation flow stress behavior of aluminum alloys include: the Power law, Sellars-Tegart model [33, 66-69] as well as the Saturation equation and power law (Sah-PL) model. The power law model is given as [33]:

$$A\sigma^{n_1} = \dot{\varepsilon} \qquad (2.1)$$

where σ is the flow stress, n_1 is the stress exponent; A is a material constant and $\dot{\varepsilon}$ is the strain rate. The power law equation which is used for creep situations holds true for $\alpha\sigma < 0.8$, where $\alpha = \frac{\beta}{n_1}$ and is a temperature-independent material constant called the stress multiplier. However at higher stress values, the power law predicts flow stress behavior with less accuracy. The exponential equation is applicable for high σ values and low temperature conditions such that $\alpha\sigma > 1.2$. The exponential equation is given as [66]:

$$Ae^{\beta\sigma} = \dot{\varepsilon} \qquad (2.2)$$

The Sellars-Tegart model is a rate equation which uses material parameters that are independent of temperature along with the Zener-Hollomon parameter (Z) in predicting the steady state

response behavior of materials at elevated temperatures. The Sellars-Tegart model actually reduces to the power law for low stress cases and into the exponential equation model for high stress, low temperature conditions. This equation can be used to correlate data over a wide range of stresses and strain rates even at temperatures where the simple power law expression fails [68]. This model is given as [33]:

$$\sigma = \frac{1}{\alpha}\sinh^{-1}\left(\frac{Z}{A}\right)^{\frac{1}{n}} \quad (2.3)$$

$$\text{where } Z = \dot{\varepsilon}e^{\frac{Q}{RT}} \quad (2.4)$$

$\dot{\varepsilon}$ refers to the effective strain rate, Q is the deformation activation energy (kJ/mol), R represents the universal gas constant (J/mol.K) and T denotes the absolute temperature (K). The temperature independent material parameters Q, R, n, α have been reported to be functions of strain and can vary with respect to a material's response to changing strain [68, 69]. The Sellars-Tegart model [33] uses an Arrhenius rate law in describing the relationship between the Zener-Hollomon parameter (Z), strain rate, flow stress and the temperature during the hot compression of AA6xxx aluminum alloys (Eqn. 2.4). The final form of the Sellars-Tegart model adapted from re-arranging equations (2.3) and (2.4) is given as [47, 68]:

$$\sigma = \frac{1}{\alpha}\ln\left[\left(\frac{Z}{A}\right)^{\frac{1}{n}} + \left(\left(\frac{Z}{A}\right)^{\frac{2}{n}} + 1\right)^{\frac{1}{2}}\right] \quad (2.5)$$

The saturation equation and power law model proposed by Sah [68] (Sah-PL) is a general exponential saturation equation in which the flow stress during hot deformation is expressed as a function of parameters such as strain, work hardening coefficient and the transient strain. The Sah-PL model is given as [70]:

$$\sigma = \sigma_o + (\sigma_{ss} - \sigma_o)\left[1 - \exp\left(\frac{-\varepsilon}{\varepsilon_R}\right)\right]^n \quad (2.6)$$

The parameter σ represents the flow stress during deformation; σ_{ss} is the steady-state flow stress and σ_o is the flow stress level at the start of plastic flow. The parameter n is the work hardening coefficient while ε_R refers to the transient strain. The stress at the onset of plastic flow σ_o and the steady-state flow σ_{ss} are modelled with the power law model as:

$$\sigma_j = \left(\frac{Z_j}{A_{1_j}}\right)^{\frac{1}{m_j}}, \; j = 0, ss \qquad (2.7)$$

The flow stress parameters σ_o and σ_{ss} are dependent on strain rate and temperature effects incorporated into the Zener-Holloman parameter Z_j in equation (2.7) and defined by equation (2.4). The parameter m_j which refers to the strain rate sensitivity and A_{1_j} are constants applicable to the Sah-PL model. The activation energy Q (in the Zener-Holloman parameter shown in equation 2.4), m_j and A_{1_j} are independent of temperature and strain rate. The Sah-PL model is only applicable for low stress conditions due to the fact that the power law does not yield accurate result above 18 MPa.

In order to account for microstructural occurrences during hot deformation compression of Al-Mg-Si alloys, the incorporation of microstructure effects such as precipitate size and distribution as well as solute content into the Sellers-Tegart model has more recently received attention. For example, Langkruis et al. [71] reported that water quenched samples with higher Mg and Si matrix solute content possess higher equivalent tensile stress during plane hot compression testing in comparison with over-aged AA6063 aluminum alloys that exhibit coarse β precipitates and lower solute content resulting in low hot flow stress. Anjabin et al. [72] reported that water quenched AA6063 aluminum alloy with higher solute content showed higher flow stress during hot compression testing in comparison to aged samples. Espedal et al. [73] showed that an increased amount of Mg_2Si precipitates results in a decrease in flow stress during

hot deformation of Al-Mg-Si alloys due to a decrease in solute hardening after heating up to the test temperature [74]. During plane strain hot compression of AA6063 aluminum alloy, Langkruis et al. [75] showed that changes in precipitate structure can influence the flow stress behavior of AA6063 aluminum alloys as coarse precipitates were observed to result into lower flow stress during the plane strain hot compression testing of AA6063 aluminum alloy.

Physically based model

The physically based constitutive equation developed by Kocks and Chen [76] for cubic metals relies on the effect of solute atoms on the stress needed for moving dislocations. This model is of the form:

$$\dot{\varepsilon} = A(\frac{\sigma}{\mu})^n \frac{\dot{\mu b^3}}{kT} \exp(\frac{-Q_D}{RT}) \qquad (2.8)$$

where μ is the shear modulus, k is the Boltzmann constant, R being the universal gas constant, Q_D is the activation energy for self-diffusion of diffusing species and b is the Burger's vector.

Effect of alloy composition on the hot deformation behavior of aluminum alloys

Several efforts have been invested in understanding the role of alloying elements such as Si, Mn, V, Fe and Cu on the hot deformation flow stress behavior of aluminum alloys. Liao et al. [77] reported an increase in the steady state flow stress and deformation activation energy with increase in the Si content of an Al-Mg-Si alloy from 0.6 to 12.3 wt. % due to increased presence of silicon particles that impede dislocation movements. Also, Wang et al. [78] reported that an increase in Si content from 2 to 15 wt. % is responsible for an increase in the hot deformation activation energy of Al-Si alloy from 152 kJ/mol to 180 kJ/mol. Increased Si solute atoms were observed to restrict dislocation movement. During the hot deformation compression of AA6063 alloy, Odoh et al. [79] reported that an increase in the Mg and Si solute content with increasing hold time results into an increase in the hot flow stress of AA6063 alloy by increasing the alloy's

deformation resistance. Nes et al. [80] reported that Mn and Si additions have significant effect on the hot deformation flow stress behavior of AA6060 and AA6082. These alloys were observed to have significantly higher hot deformation activation energy in comparison with binary alloys such as Al0.5Si and Al1Si. Complex solute atom interactions were observed between Mg-atoms on one hand and Mn-and Si-atoms on the other. These interactions were reported to be ultimately responsible for the increase in the hot deformation activation energy of the Al-Mg-Si alloys. Zhang and Baker [81] reported significantly higher hot deformation activation energy for naturally aged AA6082 aluminum alloy in comparison with annealed samples. This was attributed to the role of fine Mg_2Si precipitates that pin dislocations resulting into an increase in flow stress. The lower diffusivity of Mn in aluminum in comparison to aluminum self-diffusion has been reported to be responsible for the increase in activation energy for hot deformation (Q) in an Al-Fe-Si alloy [82]. The addition of 0.2 wt. % Mn was reported to result in retardation of the dynamic recovery process, an increase in flow stress and activation energy increase from 161 kJ/mol to 181 kJ/mol. Shakiba et al. [83] reported an increase in the flow stress and activation energy for hot deformation from 167 to 182 kJ/mol of Al-Fe-Si alloy when the Fe content is increased from 0.1 to 0.7 %. This was attributed to reduction in the mean misorientation angle and subgrain size indicating a slowing of the dynamic recovery process with increased Fe content. Shi and Chen [84] reported a significant increase in the peak flow stress and activation energy of AA7150 aluminum alloy when the V content is increased from 0.11 to 0.19 wt. %. The increased addition of V was observed to result in increased precipitation of large $Al_{21}V_2$ dispersoids that promote retardation of the dynamic recovery process and inhibition of dynamic recrystallization during the hot deformation process. During hot deformation compression of an AlFeSi alloy, Shakiba [82] reported a 19 % increase in the

alloy's flow stress with addition of 0.3 wt. % Cu. This increase was observed to be due to a reduction in the mean boundary misorientation angle and average subgrain size resulting into retardation of the dynamic recovery process with increase in the Cu content.

2.4 Age hardening response

Artificial aging is a technique that has been universally adopted for strengthening Al-Mg-Si alloys [26, 85-87]. The artificial aging process may be preceded by solution heat treatment which involves heating the alloy to a temperature between 460 ^{o}C and 530 ^{o}C in order to dissolve the alloying elements in solution [86]. This is followed by heating and holding the solution treated material at a temperature above room temperature. This results in the acceleration of precipitate formation. The needle like precipitates formed during the aging of AA6063 aluminum alloy have been identified as Mg_2Si particles responsible for an increase in the alloy's strength accompanied by a clear drop in ductility [87, 88]. During the aging process of AA6xxx alloys, solid state precipitation is usually induced at elevated temperatures based on the following sequence [15, 88]:

$$\text{Solid solution} \longrightarrow \text{GP zones} \longrightarrow Mg_2Si^{II} \longrightarrow Mg_2Si^{I} \longrightarrow Mg_2Si$$

The spherical Guinier–Preston (GP) zone formations which are extremely fine scaled solute enriched regions that offer obstruction to dislocation signify the onset of the formation of precipitates during the aging of AA6063 aluminum alloy [88]. These GP zones are Mg and Si enriched zones and their formation is followed by the precipitation of transition phases having a monoclinic structure (β^{II} structure) which grows into rod β^{I} cubic lattice structures that eventually transform to Mg_2Si precipitates responsible for the strengthening of the aged alloy.

The temperature during aging has been observed to affect tensile properties and fracture behavior of AA6063 alloy [88]. Munitz et al. [88] reported that aging temperature has a significant influence on the volume of Mg_2Si precipitate within the aged microstructure. They

noted that increased aging temperature correlates with larger but fewer Mg_2Si precipitates after peak aging time of 5 hours.

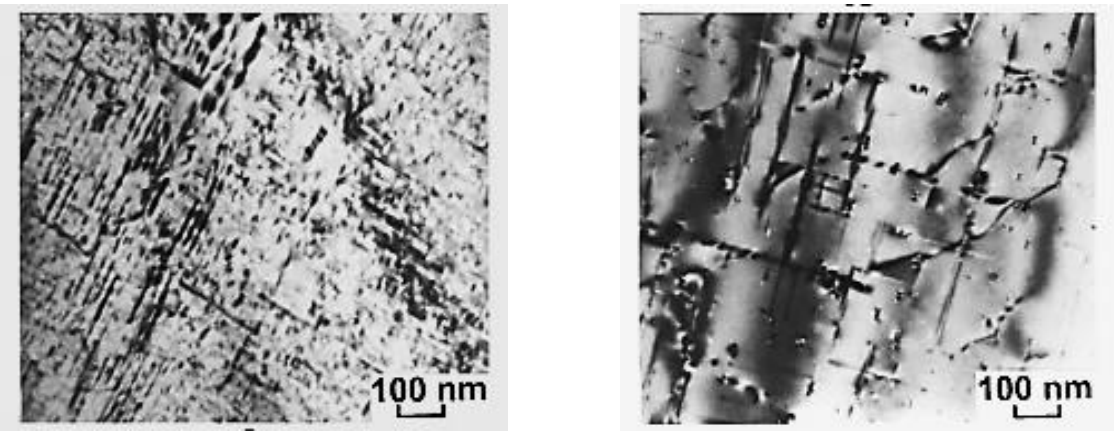

(A) (B)

Figure 2.14: Bright-field transmission electron images illustrating the internal microstructure of AA6063 aged for 5.5 hrs. A): 190 ^oC B): 240 ^oC [88]

In Figure 2.14A, the microstructure of the AA6063 alloy aged at 190 ^oC for 5.5 hours shows needle-like Mg_2Si precipitates in two perpendicular directions while the sample aged at 240 ^oC (shown in Figure 2.14B) exhibited a low density of mainly large Mg_2Si precipitates. Siddiqui et al. [20] studied the effect of aging temperature on the mechanical properties and fracture behavior of AA6063 alloy. The aluminum alloy samples were aged at 150 ^oC and 225 ^oC for 6 h. They reported an increase in tensile strength (from 80 MPa to 130 MPa) and a decrease in ductility (from 10 % to 6 %) as the aging temperature increased from 150 ^oC to 225 ^oC. The increase in strength with aging temperature was attributed to increase in density of GP zones that effectively signify the formation of the primary hardening Mg_2Si precipitates. An intergranular fracture surface with facets was observed in samples aged at lower temperatures ($\leq$200 ^oC) while samples aged at higher temperatures exhibited a cleavage fracture surface filled with striations.

Aging time has also been reported to affect the mechanical properties of aged Al-Mg-Si alloys. Jiang et al. [89] studied the influence of time on the mechanical and fracture behavior of

an Al-Mg-Si alloy aged at 160 ^{o}C. The ultimate tensile strength was observed to increase (from 164 MPa to 259 MPa) while the ductility was discovered to reduce (from 26 % to 15 %) with increase in the aging time from 1 h to 64 h. Samples aged for 1 h were reported to possess small volume fraction of dispersoids and minimal presence of GP zones. These samples were reported to exhibit a dimpled tensile fracture surface due to the absence of grain boundary precipitates. Samples aged for 64 h possess needle shaped GP zones along the <100> matrix direction and were observed to exhibit a mixed fracture mode containing dimples and intergranular rupture. The presence of high density grain boundary precipitates was confirmed in these samples. Das et al. [26] reported an increase in the strength and hardness property of an Al-Mg-Si alloy as the aging time is increased from 3 h to 7 h. The tensile strength and hardness of samples aged at 220 ^{o}C for 3 h were observed to be 130 MPa and 40 BHN respectively. For samples aged for 7 h, the tensile strength and hardness were reported to be 193 MPa and 48 BHN respectively. The increase in strength and hardness property with increased aging time was attributed to the increased diffusion of alloying elements whose partitioning encourages the formation of fine second phase Mg_2Si precipitates. Ozturk et al. [90] observed an increase in the ultimate tensile strength (from 199 MPa to 310 MPa) and hardness (65 HV to 105 HV) of AA6061-0 alloy when the aging time was increased from 20 min to 600 min. The increase in strength and hardness properties was attributed to the formation of a dense population of metastable β^{II} Mg_5Si_6 precipitates in the microstructure of the peak aged samples. Also the strain rate sensitivity parameter of the AA6061-0 alloy was observed to increase slightly with increased aging due to reduction in the amount of available free solute atoms.

Alloy composition has been reported to also affect the aging response behavior of Al-Mg-Si alloys [90-94]. Ceresara et al. [91] reported that Si in excess of that required to form

Mg_2Si influence the aging kinetics of Al-Mg-Si alloy. Excess Si was observed to reduce the solubility of Mg_2Si phases and increase the supersaturation of the alloy as well as enhance the density of GP zones. Ding et al. [92] studied the effect of Zn addition on the aging response behavior of an Al-Mg-Si alloy. The faster age hardening response behavior with increasing Zn content was attributed to the formation of the metastable η-$MgZn_2$ phases and faster precipitation of β-Mg_2Si strengthening phases. Cu content has been reported to influence the precipitation sequence of Al-Mg-Si-Cu alloys [94, 95]. Miao and laughlin [94] reported that the precipitation sequence in AA6022 alloy aged at 175 ^oC can be influenced by the addition of Cu. The precipitation sequence in samples containing 0.07 wt. % Cu was found to be GP zones→ needlike β^{II}→ rod like β^{I} + lathlike Q^{I} →β + Si while the precipitation sequence of samples containing 0.91 wt. % Cu is GP zones →needlike β^{II}→lathlike Q^{I}→Q + Si. The alloy containing 0.91 wt. % Cu was reported to show faster age hardening kinetics [94]. Camero et al. [96] studied the effect of vanadium addition on the precipitation kinetics of extruded Al-Mg-Si alloys. Figure 2.15 shows the transmission electron microscope (TEM) bright field images of aged AA6063 alloy (with and without vanadium) after aging at 175 ^oC for 8 h .

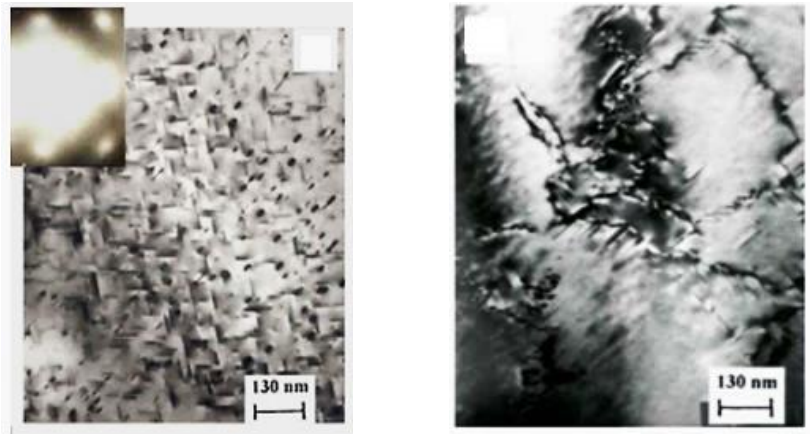

(A) (B)

Figure 2.15: TEM bright field images of extruded AA6063 alloy (A):Without V, (B): 0.1 wt. % V [96]

As seen in Figure 2.15A, AA6063 alloy with no V content was observed to contain β^{II} phases after aging at 175 ^{o}C for 8 h. However, the alloy containing 0.1 wt. % V content (Figure 2.15B) exhibited rod-shape β^{I} phases with average size of 100 nm length after aging at 175 ^{o}C for 8 h. This indicates that 0.1 wt. % V addition is responsible for acceleration of the precipitation of Mg_2Si strengthening phases in the extruded and aged AA6063 alloy. The presence of β^{I} phases in the alloy with no V content was confirmed only after aging for 128 h.

2.5 Effect of alloy composition

The mechanical and fracture properties as well as microstructure exhibited by extruded AA6xxx series aluminum alloys have been reported to be dependent on the elements present in the alloy's composition [97-103]. Wang et al. [97] reported that the tensile strength of extruded Al-Mg-Si alloy can be increased by increasing the Si content. The ultimate tensile strength was observed to increase from 120 MPa to 190 MPa with an increase in the Si content from 0.58 to 12.30 wt. %. The homogenized sample containing 0.58 wt. % Si was reported to contain short rod-like Fe rich phases while the sample containing 12.30 wt. % Si exhibited a microstructure filled with fibrous eutectic Si well spheriodized into fine particles. After extrusion, the alloy containing higher Si content was observed to exhibit a recrystallized microstructure owing to the equal distribution of Si particles which accumulate dislocations during the extrusion process. The alloy containing higher Si content was reported to exhibit higher ductility after extrusion due to the grain refining effect caused by recrystallization. Dorward and Bouvier [98] studied the effect of 0.5 wt. % Si in excess of that required to form Mg_2Si on the yield strength and toughness of AA6061 alloy solutionized at 540 ^{o}C.

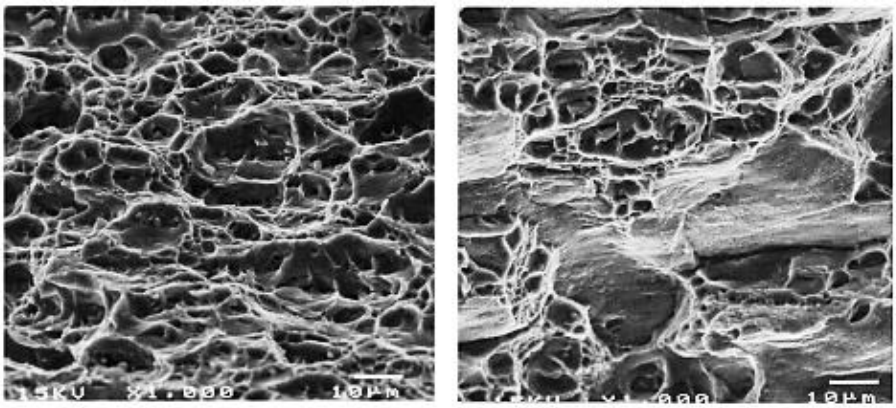

(A) (B)

Figure 2.16: Scanning electron fractographs of AA6061alloy (A): Rich balanced Mg-Si stoichiometry (B): 0.5 wt % excess Si [98]

Dorward and Bouvier [98] reported a 9 % increase in the alloy's yield strength and 28 % reduction in toughness when 0.5 wt. % excess Si is added. The increase in strength was attributed to increased solubility of Mg_2Si with increase in the excess Si level. The fracture surfaces of samples containing a rich balanced Mg-Si stoichiometry and 0.5 Wt. % excess Si are shown in Figure 2.16A and B respectively. The samples containing a balanced stoichiometry (Figure 2.16A) were observed to exhibit a ductile transgranular fracture morphology characterized by void formation at constituent particles while the samples containing 0.5 wt. % excess Si exhibited regions of intergranular fracture morphology characterized by a weakened grain boundary structure. The reduction in toughness was observed to be due to the promotion of intergranular precipitation by excess Si. Yildrim and Ozyurek [99] observed that an increase in Mg content (0.43 to 0.86 wt. %) results in an increase in the hardness and ultimate tensile strength (UTS) but aa reduction in ductility of heat treated Al-Mg-Si alloy. The UTS was reported to increase from 179 MPa to 210 MPa while the elongation reduced from 8 % to 3 % with increase in Mg content. The increase in hardness and strength with increase in Mg content was attributed to the increased presence of secondary Mg_2Si precipitates within the aluminum dendritic structure after heat treatment. The reduction in ductility with increased Mg content was

reported to be due to increased presence of Fe-rich π ($Al_8FeMg_3Si_6$) intermetallic compounds. However, Mg content was observed to have no influence on the fracture morphology as all the heat treated Al-Mg-Si alloy samples were observed to exhibit ductile fracture morphology. Dowling and Martin [100] reported that slip homogenization and a nearly uniform dislocation density due to the presence of Mn containing dispersoids are responsible for an increase in the toughness and tensile strength of an Al-Mg-Si alloy. During examination of fracture surfaces of Al-Mg-Si alloys, Busby et al. [101] reported that an increase in Mn-dispersoid content results into a reduction in occurrence of intergranular fracture and increase in transgranular ductile rupture. The dispersoids were observed to cause slip homogenization and prevent attainment of critical local strain required for intergranular crack nucleation. Jenski [102] observed slight and significant increase in the average yield strength and elongation respectively of rolled redraw AA6061-T6 alloy due to addition of 0.19 wt. % Cr. The addition of 0.19 wt. % Cr was reported to promote the transformation of β-$Al_9Fe_2Si_2$ to the more stable α-$Al_{12}Fe_3Si$ phase which is beneficial to the formability of the alloy. During tensile testing of peak aged Al-Zn-Mg-Cu alloys, Wagner and Shenoy [103] observed that alloys containing Zr dispersoids exhibit superior toughness in comparison with those containing Cr dispersoids. This was attributed to the finer and more coherent nature of Al_3Zr dispersoids in comparison to Cr rich E-phase dispersoids present in the alloy matrix. Wong et al. [104] studied the effect of Zr addition on the strength and hardness properties of a heat treated Al-Mg-Si alloy. 0.15 wt. % Zr addition was observed to be responsible for an increase in the hardness property from 75 VHN (in the base alloy) to 105 VHN as well as a 23 % increase in the alloy's tensile strength. The increase in strength and hardness properties was attributed to the presence of Al_3Zr precipitates that block dislocation motion through their grain boundary pinning effect. Ji et al. [105] studied the influence of Fe

content on the mechanical properties of Al-Mg-Si alloy. An 8 % increase in yield strength and 295 % decrease in ductility were observed due to 2.5 wt. % Fe addition. The increase in yield strength was reported to be due to strengthening provided by increased presence of Fe-rich α-Al_8Fe_2Si phases present at α-Al grain boundaries. The reduction in ductility was observed to be due to increased formation of large coarse needlelike β-AlFe precipitates in the alloy's microstructure. Shabestari and Moemeni [106] reported an increase in the strength and reduction in ductility of an Al-Mg-Si alloy when Cu is added up to 1.5 wt. %. The increase in strength with increasing Cu content was attributed to increased precipitation of Al_2Cu precipitates within interdendritic spaces. The Cu bearing phases were observed to slow dislocation mobility and therefore increase alloy strength property. However, Cu addition above 1.5 wt. % was reported to encourage nucleation of porosities that serve as stress concentration sites that ultimately cause reduction in the strength of the Al-Mg-Si alloy. Xu et al. [107] studied the effect of Sc addition on the mechanical properties and fracture morphology of Al-Mg-Si alloy. The tensile strength and ductility were observed to increase with addition of Sc. The increase in strength and ductility is attributed to the multi-refinement of the alloy microstructure due to presence of Sc, precipitation of nano-size Al_3Sc dispersoids as well as complete spheriodization of the eutectic Si. A quasi-cleavage fracture morphology characterized by extensive irregular cleavage planes and some tearing ridges was observed in the Al-Mg-Si with no Sc content. The fracture type was reported to change into a dimple ductile fracture morphology with increase in Sc content as samples containing 0.8 wt. % Sc were observed to exhibit a completely ductile fracture surface filled with uniformly distributed small dimples resulting into a significant increase in ductility.

2.6 Summary

A comprehensive review of research on the extrusion, heat treatment and subsequent mechanical properties of AA6xxx aluminum alloys shows that extensive work has been done in

order to understand the relationship between the thermomechanical history experienced and the microstructure as well as mechanical property evolution after extrusion and heat treatment. One area that has not received much attention is a systematic through process (from extrusion processing to aging) study of the effect of extrusion temperature, alloy composition and aging time on the mechanical property evolution and fracture morphology of Al-Mg-Si alloys. It is also important to determine the influence of alloying elements such as Cr and Mg-Si level on the hot deformation flow stress behavior of Al-Mg-Si alloys. Also, little effort has been previously invested into developing constitutive models for predicting the hot deformation flow stress behavior of Al-Mg-Si alloys while accounting for the Mg-Si solute content.

CHAPTER 3

Scope and Objectives

General Motors (GM), one of the leading manufacturers in the automobile industry is interested in the development of metals and alloys that have improved crash and impact resistance properties as well as an excellent strength to weight ratio. The development of such materials is central to GM's strategic plan to be the global leader in the production of fuel efficient and cost effective automobiles. The application of aluminum alloys as materials for the manufacture of front rail components in automobiles is an area that still requires more research effort. In order to satisfy such requirements as strength, ductility and extrudability; there exists the need to understand the effect of alloy composition and process parameters such as extrusion temperature as well as post extrusion aging condition on the final mechanical properties of extruded AA6xxx alloys. A collaborative research project team was initiated to address alloy development, design and optimization as well as manufacture of an extruded front rail profile for implementation in high volume mid-size cars. The overall objectives of the project include the design of an optimized geometry for front rails that satisfy energy requirements, development of alloy composition to achieve desired material properties, development of models to predict the extrusion load requirements in manufacturing the front rail components and design of an extrusion process to extrude the front rails with optimized geometry. The specific objectives for this research include:

- To understand the influence of alloy composition on the hot flow stress behavior of Al-Mg-Si alloys.
- Development and validation of a constitutive model for predicting the hot flow stress behavior of Al-Mg-Si alloy while accounting for the Mg-Si solute content level during pre-deformation heating.

- Understand the role of alloy composition and extrusion conditionvvvgfgvv on the through thickness microstructure of extruded Al-Mg-Si alloys.
- Investigate the effect of alloy composition, extrusion and aging condition on the extrudability, mechanical properties and fracture morphology of Al-Mg-Si alloys.

In order to achieve the identified objectives, a series of hot compression deformation experiments, extrusion trials, microstructural characterization and mathematical modeling were performed.

CHAPTER 4

Methodology

In this research, effort is made towards gaining better understanding of the extrusion processing and subsequent mechanical properties as well as hot deformation behavior of Al-Mg-Si alloys for front rail application in automobiles.

Hot compression deformation experiment, extrusion trials and mechanical property characterization were performed in order to achieve the set objectives. Also in order to account for Mg-Si solute content, a mathematical model is applied in development of accurate constitutive model for prediction of the hot deformation behavior of an Al-Mg-Si alloy.

4.1 Start Materials

The elemental composition of AA6xxx aluminum alloys is of primary interest in manufacturing process such as extrusion and post manufacture handling process such as aging. Elemental composition has been reported to influence the extrudability as well as post extrusion properties of AA6xxx alloys [108]. The chemical composition of the as-cast Al-Mg-Si alloys designed and supplied by GM is given in Table 4.1.

Table 4.1: Percent weight compositions of AA6xxx aluminum alloys

Alloy	Si	Fe	Cu	Mn	Mg	Ti	Cr	Al
1	0.5	0.20	0.15	0.1	0.50	-	0.2	
2	0.6	0.20	0.15	0.1	0.90	-	-	Balance
3	0.6	0.20	0.15	0.1	0.90	-	0.2	
4	0.4	0.16	<0.01	0.029	0.49	<0.01	-	

Alloys 1-3 were designed as variants of alloy 4 (considered to be the baseline alloy) in order to improve strength and fracture properties. The Al-Mg-Si alloys were industrially direct chill (DC) cast then homogenized at 560 ^{o}C (100 ^{o}C/h) for 4 hours followed by air cooling. The optical micrographs of the alloys in the as-cast form prior to homogenization are shown in Figure 4.1.

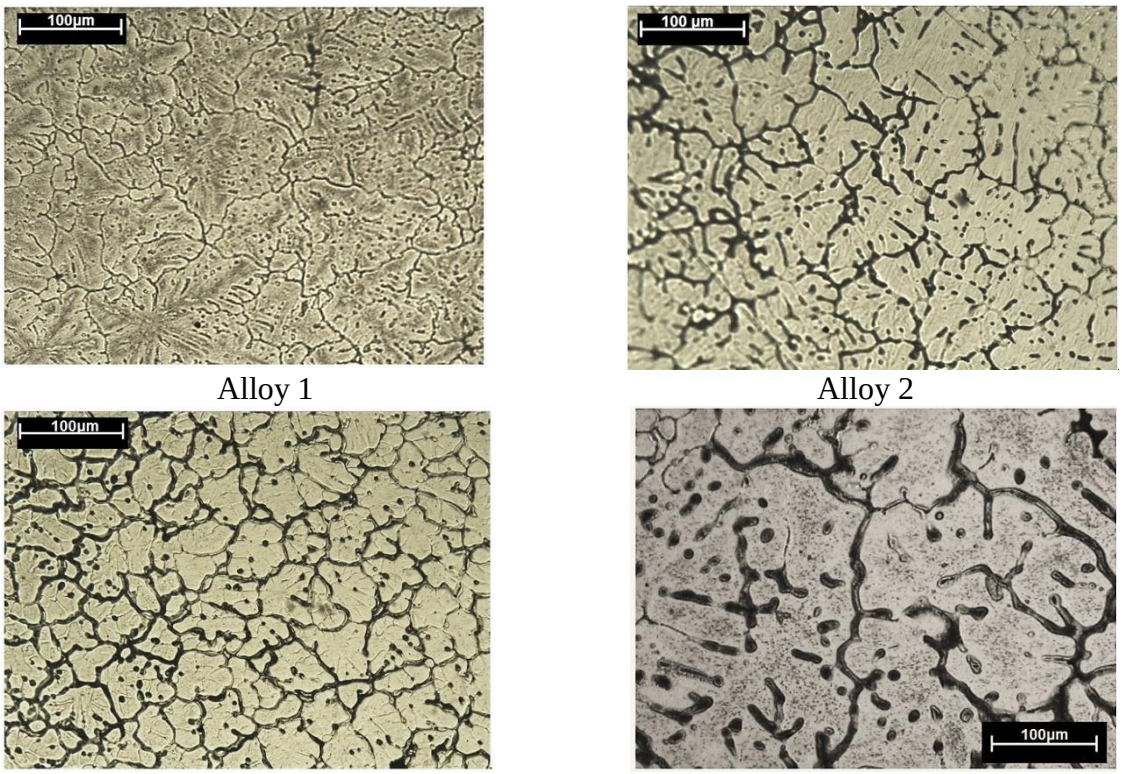

Figure 4.1: As-cast microstructures of the AA6xxx alloys

The as-cast microstructures of the AA6xxx alloys are characterized by the presence of micro-segregated regions and concentration gradients. The as-cast structures contain unstable monoclinic Chinese script like β-AlFeSi phases at the interdendritic regions. These unstable intermetallic second phase AlFeSi particles are formed by the combination of insoluble Fe with Si and Al.

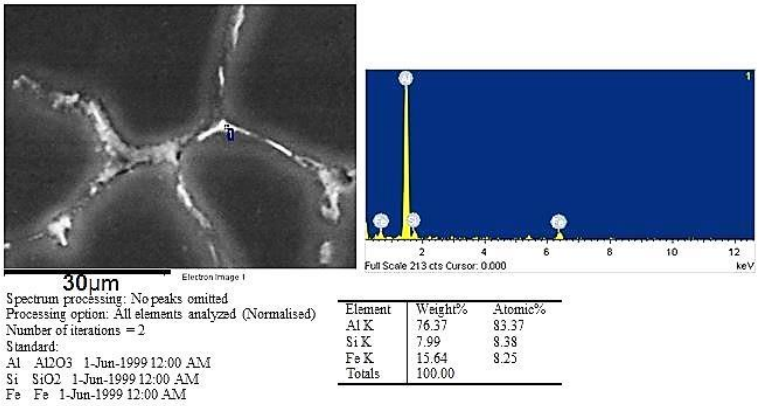

Figure 4.2: Scanning electron microscopy (SEM) image and energy-dispersive spectroscopy spectra (EDS) as-cast alloy 3

As shown in Figure 4.2, the presence of the Chinese-script like β-AlFeSi phases at grain boundaries was confirmed by SEM images and EDS. Homogenization heat treatment was performed in order to ensure formation of stable α-AlFeSi phases within alloy microstructure as well as reduction of concentration gradients and micro-segregation. Figure 4.3 shows the microstructure of the alloys after the homogenization process. The homogenization process was as prescribed by General Motors (GM), one of the stakeholder partners in the research project.

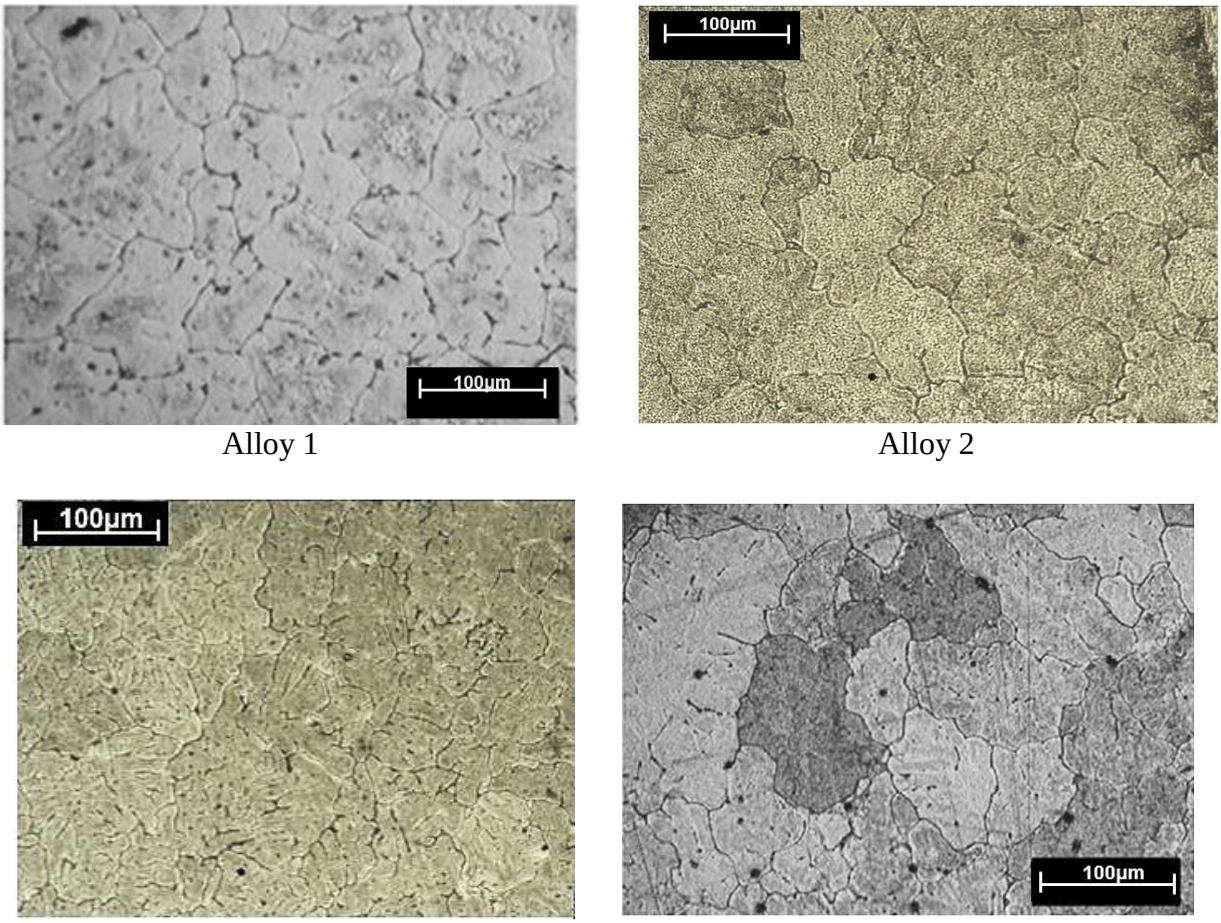

Alloy 1 Alloy 2

Alloy 3 Alloy 4

Figure 4.3: Homogenized microstructure of AA6xxx alloys

The alloys were observed to exhibit an equiaxed grain structure after the homogenization process. In all the aluminum alloys studied, the presence of rod like rhombic α-AlFeSi phases at interdendritic regions was confirmed by EDS (Figure 4.4).

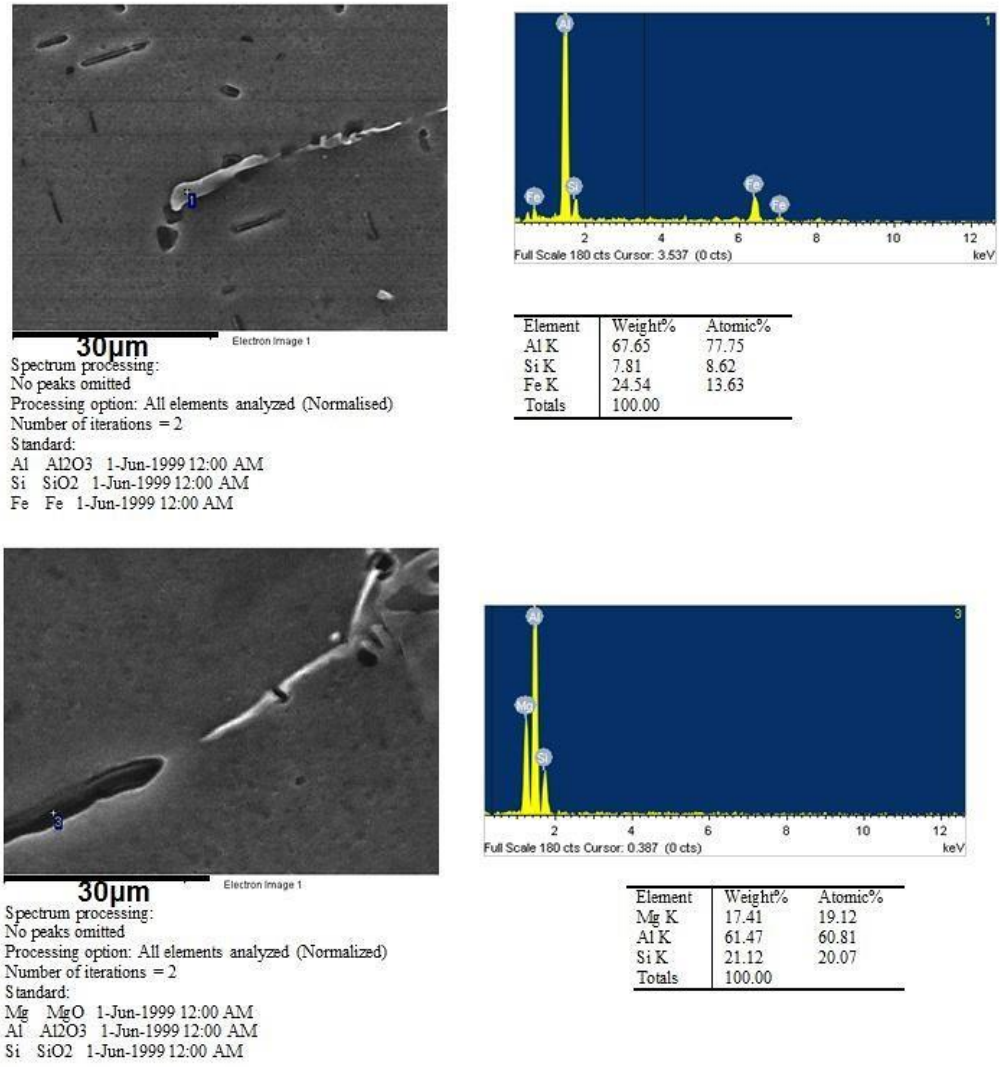

Figure 4.4: SEM image and EDS spectra confirming presence of α-AlFeSi and Mg_xSi_y particles in homogenized sample (Alloy 3)

4.2 Experiment

4.2.1 Hot compression tests

The hot deformation flow stress behavior of AA6xxx alloys was determined by performing deformation compression tests on homogenized alloy samples in a Gleeble 3500 thermomechanical simulator. The thermo-mechanical simulator is an integrated hydraulic servo-controlled apparatus with an in-situ heating system. Figure 4.5 shows the cylindrical compression sample held between grips in a Gleeble 3500 thermo-mechanical simulator.

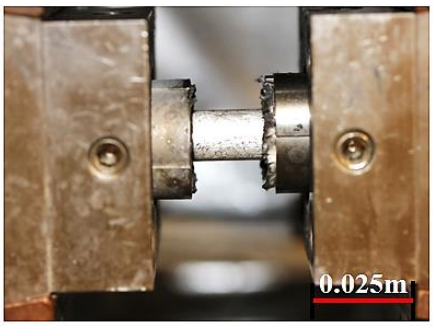

Figure 4.5: Cylindrical homogenized compression sample held within grips on the Gleeble 3500 thermomechanical simulator

The cylindrical compression samples with nominal dimensions ϕ10 mm × 15 mm were machined out of the same location on the homogenized billets in order to ensure that differences in present phases do not result in disparity in material flow stress behavior. The dimensions of the compression samples were chosen to conform to ASTM E209-00 standard. The hot compression deformation process (shown in Figure 4.6) involves heating the cylindrical compression sample (heating rate of 10 ^{o}C/s was applied in all tests performed in this work) to deformation temperature followed by holding at this temperature prior to the actual deformation process.

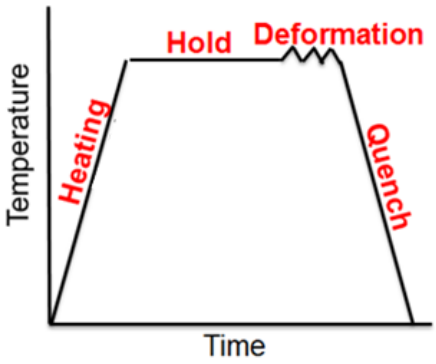

Figure 4.6: Schematic of the hot compression deformation process

The homogenized compression sample is held at test temperature prior to deformation in order to ensure heat balance and elimination of thermal gradients. Samples were deformed to true strain of 0.6 followed by water quenching in order to retain the post-deformation microstructure. Hot deformation compression tests were conducted on the four Al-Mg-Si alloys at four different

temperatures of 400, 450, 500 and 550 ^{o}C and four strain rates of 0.01, 0.1, 1 and 10 s^{-1}. During the hot compression deformation testing of these alloys, samples were held at test temperature for 1 min prior to the actual deformation. The deformation tests were repeated three times for each deformation condition in order to check for consistency in the flow stress data.

In order to determine the effect of pre-deformation hold time on hot flow stress behavior of AA6xxx alloys, alloy 4 samples were heated to 450 ^{o}C at 10 ^{o}C/s then held at this temperature for different times followed by deformation at 0.12 s^{-1} and 10 s^{-1}. The hold times applied are shown in Table 4.2.

Table 4.2: Deformation conditions to determine effect of hold time on flow stress behavior

Temperature (^{o}C)	**Strain rate (s^{-1})**	**Hold time (min)**
450	0.12	1, 5, 12.5, 16.5, 25
450	10	1.5, 12.5, 16.5, 25

4.2.2 Extrusion trials

In order to determine the influence of extrusion temperature on mechanical properties, microstructural evolution and fracture morphology of Al-Mg-Si alloys; laboratory scale extrusion of alloys 1-4 were performed in a 150 ton Wabash extruder at the University of Waterloo. The Wabash extrusion press equipment is shown in Figure 4.7.

Figure 4.7: Wabash laboratory scale extruder used for strip extrusion of AA6xxx alloys

Figure 4.8 shows a close up view of the extrusion ram, container and the cylindrical billet.

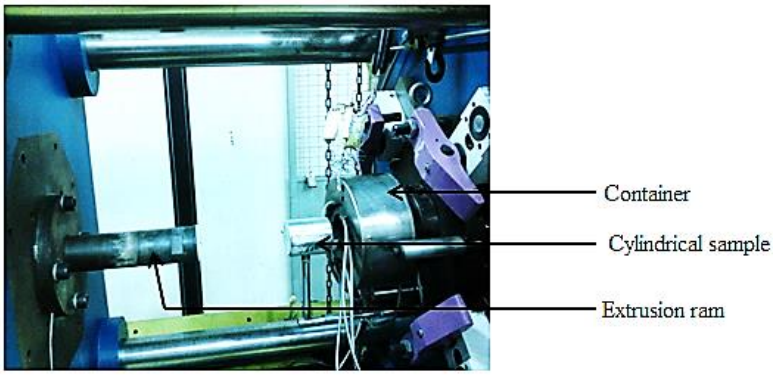

Figure 4.8: Close-up view of extruder showing the container, sample and ram

The laboratory scale extruder has a 75 mm diameter container designed to duplicate the internal extrusion pressures observed on larger production press equipment. The laboratory scale extruder is fully instrumented with thermocouples embedded in the container, die, ram and billet in order to measure temperature at various locations during the extrusion process. The hydraulic pressure and ram displacement during the extrusion process were recorded using a data acquisition system. Cylindrical extrusion samples with dimensions ϕ76 mm × 89 mm were machined from homogenized billets of the identified AA6xxx alloys along the casting direction. The cylindrical extrusion billets were extruded at 480, 500 and 520 ^{o}C into strip profiles measuring 1.9 mm in thickness and 53.3 mm in width. This implies that the extrusion trials were performed at an extrusion ratio E_R (defined as the ratio of the cross-sectional area of the upset billet to that of the extruded material) of ~ 44. The extruded profiles were air cooled to room temperature after the extrusion test. The extrudability of the alloys was determined as a function of the load required to extrude the sample and the ram speed during the extrusion process.

Alloys 1 – 4 were also industrially extruded into front rail profiles at 500 ^{o}C and E_R = 40 (starting billet diameter of 9 in) in a 2200 ton extrusion set up at Sapa Extrusions Canada. Alloy 4 industrial extrusions were tempered to T4 (solution heat treatment of the extruded profiles at

540^{o}C for 90 minutes followed by natural aging) and T6 designations (solution heat treatment and artificial aging at 171^{o}C for 10 hours) while alloys 1-3 were only aged to T6 condition.

4.2.3 Mechanical properties

After the extrusion trials, some of the laboratory extruded strip profiles were directly aged at 185 ^{o}C for 3, 5 and 8 hours with no solutionizing heat treatment while the remaining strip profiles were solutionized at 540 ^{o}C in a sand bath furnace for 40 minutes followed by water quenching. The solutionized strip profiles were thereafter heat treated at 185 ^{o}C for 3, 5 and 8 hours. The as-extruded and air cooled strip profiles were designated T4 temper while the extruded and aged samples with no solutionizing heat treatment were designated T5 temper. The T6 temper designation refers to samples extruded, solutionized and aged. In order to determine the influence of alloy composition, extrusion temperature and aging condition on the mechanical properties and fracture morphology of the AA6xxx alloys studied, hardness measurements and uniaxial tensile test were performed on tensile samples extracted from the T4, T5 and T6 extruded profiles.

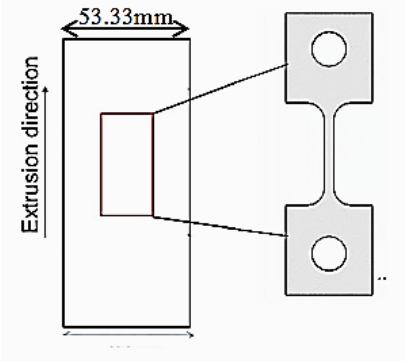

Figure 4.9: Laboratory extruded strip profile showing location of extracted tensile samples

The geometry of the extruded strip profile showing locations where tensile samples were extracted is shown in Figure 4.9. Figure 4.10 shows the dimensioning of the miniature dog bone style tensile sample extracted from the strip profiles along the extrusion direction. Quasi-static

tensile test was performed at strain rate of 0.1 s^{-1} on Instron 1331 servo hydraulic equipment. Sample elongation during the tensile test was measured using a ± 5 mm extensometer.

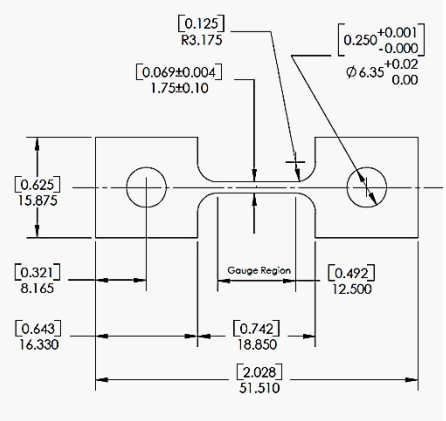

Figure 4.10: Schematic of mini dog bone tensile sample (dimension in inches in bracket) [109]

Stress-strain curves obtained during quasi-static tensile tests on miniature dog bone tensile samples have been reported to match those of ASTM E 8M-04 up to the ultimate tensile strength (UTS) [109]. The hardness property of the extruded profiles in the T4, T5 and T6 temper conditions was determined by micro hardness measurements using a 100g load on Wolpert Wilson micro Vickers 402MVD hardness equipment. The hardness test for each profile was performed at through thickness locations corresponding to gauge length centre of extracted miniature dog bone samples. The hardness and tensile tests were repeated three times for each condition in order to ensure consistency in the measured data. The average Vickers hardness value, UTS and elongation are reported in this study.

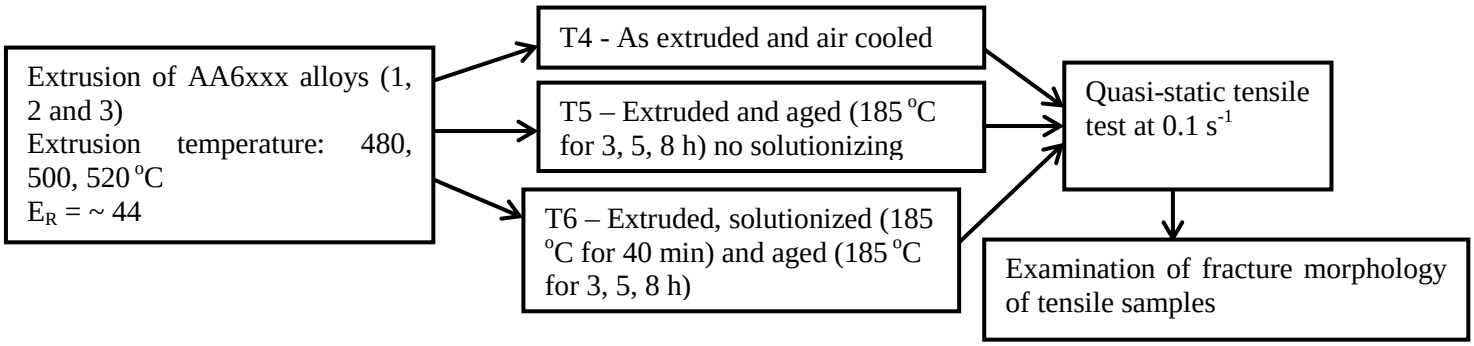

Figure 4.11: Mechanical property characterization of laboratory extruded AA6xxx alloys

Figure 4.11 shows a step by step path of efforts towards determining the role of extrusion and aging conditions as well as alloy composition on mechanical properties and fracture morphology of AA6xxx alloys. The mechanical properties of alloys 1-3 after industrial extrusion were also determined by performing quasi-static tensile test at 0.1 s^{-1} on T6 samples extracted along the extrusion direction (location as shown in Figure 4.12).

In order to determine the strain rate sensitivity and plastic anisotropy behavior of the industrially extruded alloy 4 in the T4 (solution heat treatment at 540 ^{o}C for 90 minutes followed by natural aging) and T6 (solution heat treatment and artificial aging at 180 ^{o}C for 3 hours) conditions, quasi-static tensile tests were performed at 0.001, 0.01 and 0.1 s^{-1} on samples extracted in the extrusion, 45^{o} and transverse direction. The geometry of alloy 4 front rail profile extruded at 500 ^{o}C is shown in Figure 4.12.

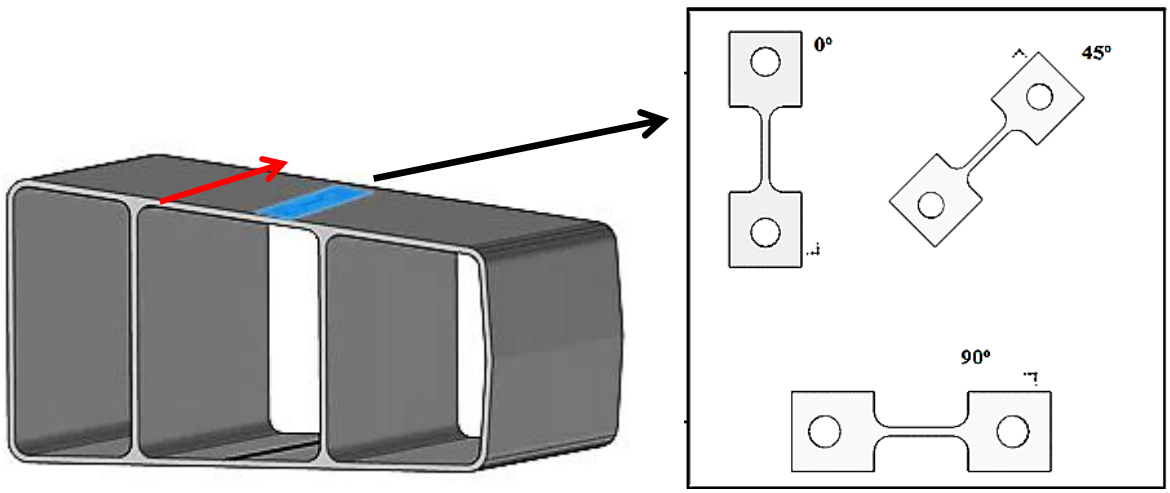

Figure 4:12: Industrial extrusion profile (red arrow is extrusion direction)

4.2.4 Microstructure characterization

After hot compression deformation testing in Gleeble thermo-mechanical simulator equipment, deformed samples were sectioned parallel to the compression direction and then prepared for microstructural observation. Grinding of deformed samples was performed by using silicon carbide (SiC) paper 240, 400, 600, 1200 in that order followed by polishing of sample

surface. During polishing process, 9 μm, 3 μm, 1 μm and 0.25 μm polishing solutions were used on MD-Chem and MD-Mol polishing pads to remove surface defects and scratches. The grain structure of deformed alloys was thereafter revealed by anodizing sample surface with 3 % HBF_4 Barker's reagent for 1.5 minutes at 30 V. The grain structure was then examined under polarized light in an optical microscope.

The influence of alloy composition and extrusion ratio on the microstructure was determined by optical examination of the through thickness section of the laboratory extruded profiles (E_R = 44) and sections cut from profiles of the AA6xxx alloys extruded on a 2200 ton industrial extrusion press at extrusion ratio E_R = 40.

In order to determine the average radius r_o of Mg_2Si particles present in alloy 4, high magnification scanning electron microscope (SEM) examination and energy dispersive spectroscopy spectra (EDS) of alloy 4 in the homogenized condition were performed.

The fracture morphology of alloys 1, 2 and 3 after tensile testing in the T5 and T6 conditions were examined by SEM.

4.3 Mathematical modeling

4.3.1 Mg_2Si particle dissolution model

In order to account for Mg-Si solute content in the constitutive model to be developed for predicting the hot flow stress behavior of alloy 4, a dissolution model was developed by incorporating hold time into Vermolen's finite volume particle dissolution model [110-112]. A computer code developed using the MATLAB environment was utilized to simulate the dissolution of Mg_2Si particles in the alloy matrix during the heat up and hold period prior to deformation. The details of the Mg_2Si particle dissolution model are presented in Appendix A. In order to determine the Mg-Si solute content for specific deformation temperature and hold time, the size distribution of Mg_2Si particles was determined from SEM images of alloy 4. Figure 4.13

shows the size distribution of Mg_2Si particles measured from SEM images of homogenized alloy 4. Using this data, an average particle radius r_o = 0.5 μm was determined.

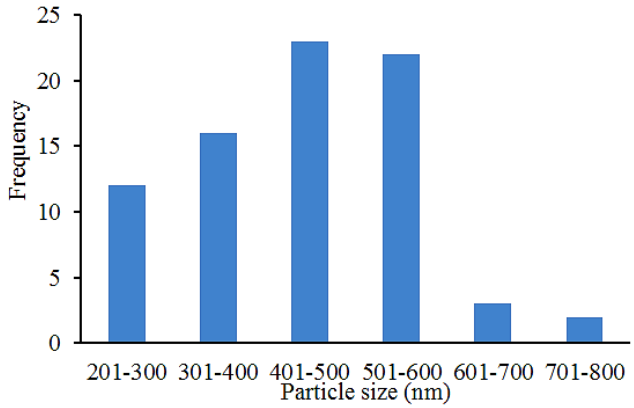

Figure 4.13: Measured Mg_2Si particle size distribution in alloy 4

Figure 4.14 confirms the presence of AlFeSi intermetallics and Mg_2Si particles in homogenized alloy 4.

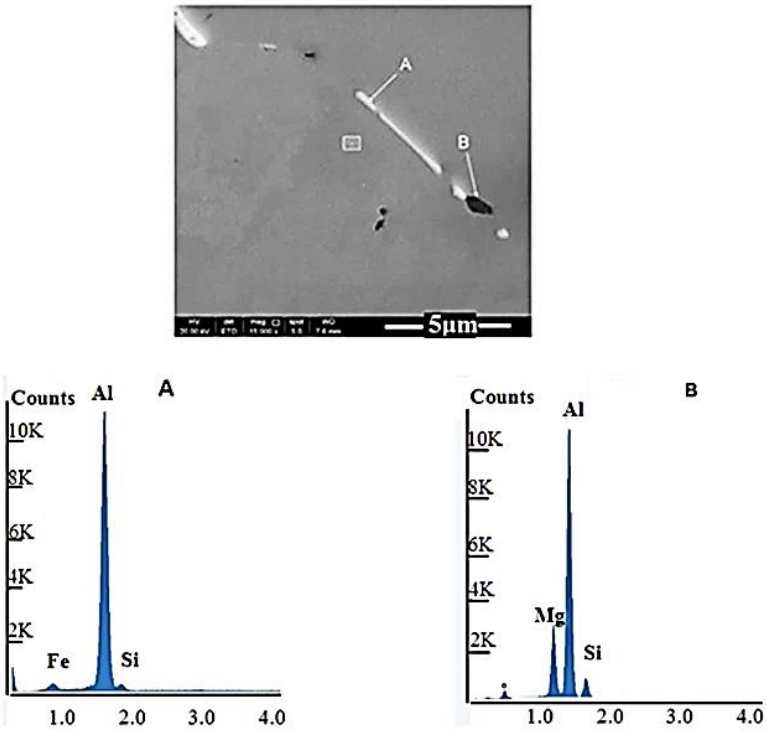

Figure 4.14: SEM image of homogenized alloy 4 showing presence of AlFeSi intermetallic and Mg_2Si particle confirmed by energy dispersive spectroscopy spectra (EDS) for (A): α –AlFeSi (B): Mg_2Si

4.3.2. Extrusion modeling

In order to predict the thermo-mechanical history during extrusion process, the commercial Finite Element package, DEFORM-2D was used to model the laboratory scale extrusion of alloy 4 into a cylindrical rod. Deform 2D is based on the flow formulation approach using an updated Lagrangian procedure. Alloy 4 billet was extruded at 485 ^{o}C into a rod measuring 25mm diameter which represents an extrusion ratio of 9. The thermal history experienced by the alloy during the extrusion process was measured by thermocouples embedded in the container, die, and ram. The details of the extrusion modeling are presented in Appendix B.

CHAPTER 5
Results and Discussion

The results of the research are presented and discussed in this chapter. The effect of alloy content and Mg-Si solute content on the hot deformation flow stress behavior of Al-Mg-Si alloys is reported. The roles of alloy composition and extrusion condition on the extrudability and microstructure of extruded Al-Mg-Si alloys are also presented. Finally, the influence of alloy composition, extrusion condition and aging time on the mechanical properties, microstructure and fracture morphology of Al-Mg-Si alloys are discussed.

5.1 Hot compression behavior

Measured Flow stress curves

The temperature – time data and strain – time plot during the hot deformation of alloy 1 at 400 ^{o}C and strain rate of 10 s^{-1} are shown in Figure 5.1.

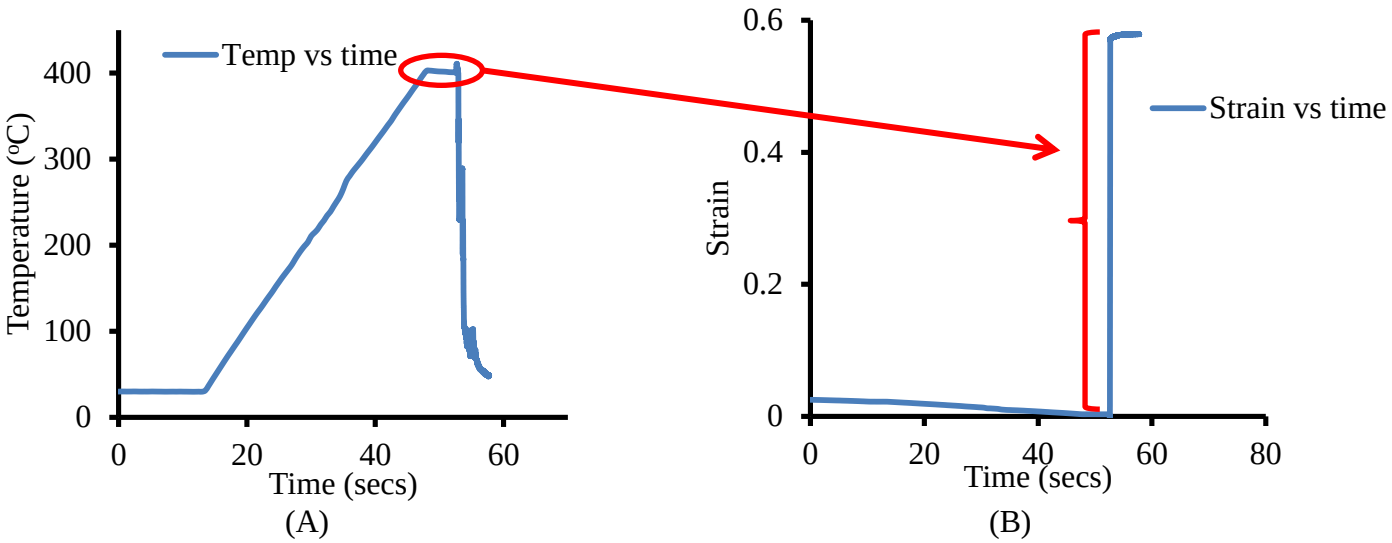

Figure 5.1: (A): Temperature vs time, (B): Strain vs time plots during hot deformation of alloy 1

Figure 5.1A shows that the sample is heated to test temperature of 400 ^{o}C at a rate of 10 ^{o}C/s prior to actual deformation. The actual deformation of the sample at 400 ^{o}C shown in Figure 5.1A (shown in red circle) corresponds to the range of changing strain in Figure 5.1B. As seen in Figure 5.1B, the actual deformation occurs very rapidly due to the high deformation strain rate

(nominal strain rate of 10 s^{-1}). The actual strain rate during the deformation of the sample in the Gleeble thermomechanical simulator was determined as:

$$\dot{\varepsilon} = \frac{d\varepsilon}{dt} \qquad (5.1)$$

Figure 5.2 shows the strain rate vs. strain plot during the deformation process. The average actual strain rate $\dot{\varepsilon}_{\text{avg actual}}$ was subsequently calculated as the average of strain rate between strain of 0.1 and 0.6.

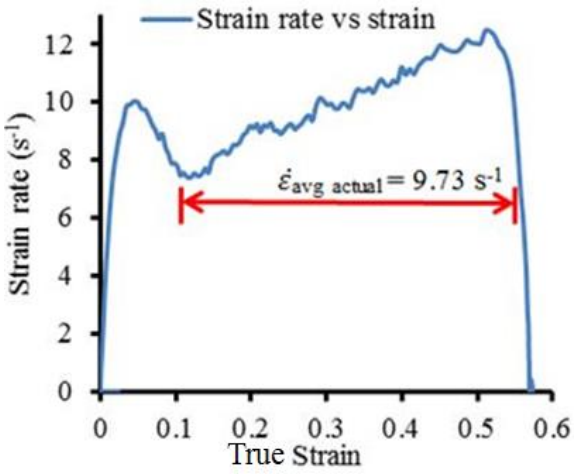

Figure 5.2: Strain rate vs strain plot for alloy 1 deformed at 400 ^{o}C and 10 s^{-1}

Typical true stress-strain curves obtained during the hot deformation compression of alloy 1 at different deformation conditions are presented in Figure 5.3.

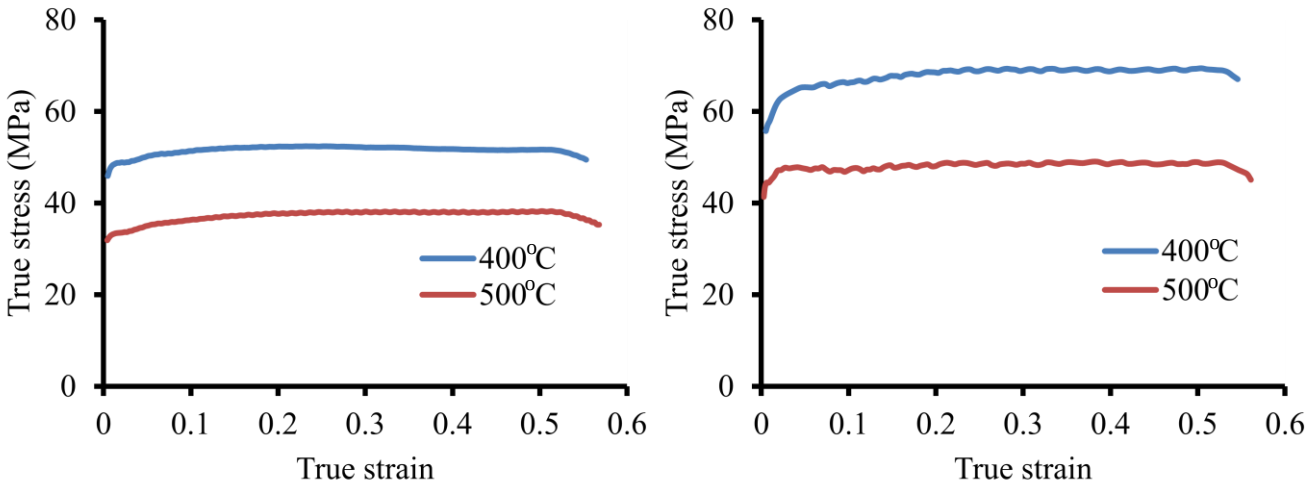

Figure 5.3: Flow stress curves for alloy 1 at (A): 1 s^{-1} (B): 10 s^{-1}

The average experimental steady state flow stress for each deformation condition was determined from the experimental flow curves as the average of stress values from a true strain of 0.1 to 0.6. As shown in Figure 5.3, alloy 1 exhibits a steady flow stress behavior as the stress was observed to be relatively constant with strain. This indicates that dynamic equilibrium is reached quickly between work hardening and dynamic recovery mechanisms during the hot deformation of this alloy. The flow stress curves of alloy 1 shown in Figure 5.3 indicate that the flow stress is very sensitive to both the deformation temperature and strain rate. As the temperature increases, the flow stress decreases for a given strain rate while flow stress increase with strain rate increase for a given deformation temperature.

5.1.1. Effect of alloy content

In this section, the influence of alloy composition on the flow stress behavior, strain rate sensitivity parameter and activation energy of Al-Mg-Si alloys have been determined by performing hot deformation compression test on alloys 1, 2 and 3. The detailed experimental procedure is described in section 4.2.1. The stress-strain curves for alloys 1-3 after deformation at specific temperatures and strain rates are shown in Figure 5.4. The average experimental steady state flow stress for each deformation condition was determined from the experimental flow curves as the average of stress values from a true strain of 0.1 to 0.6.

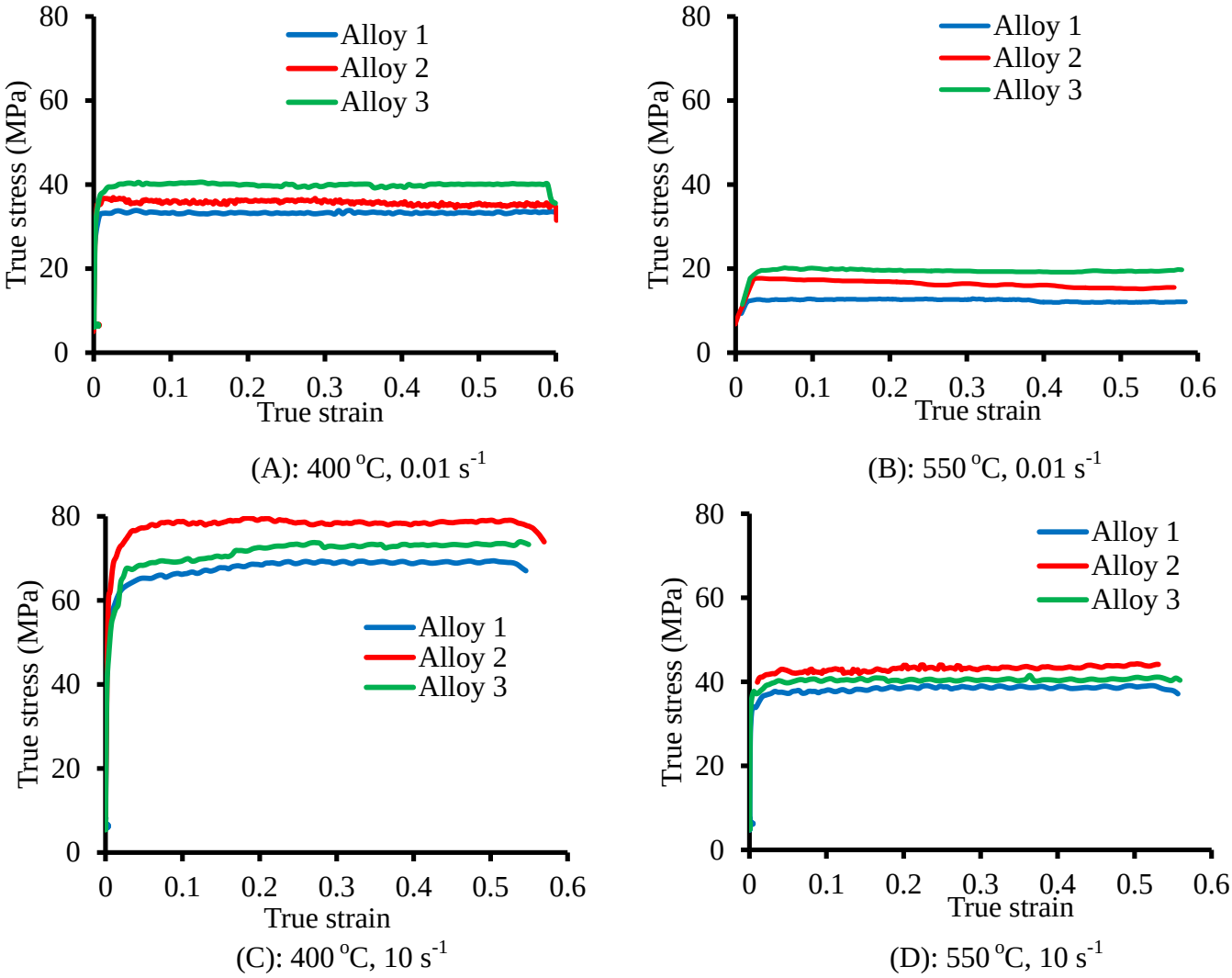

Figure 5.4: Typical stress-strain curve during hot compression deformation

The steady flow stress during the deformation process was observed to change only slightly with increasing strain. The slight increase in flow stress with strain observed in the flow stress curve of alloy 3 deformed at 400 °C, 10 s^{-1} is only due to very small changes in actual test strain rate during the deformation process. In each alloy, the average flow stress was observed to increase with increasing deformation strain rate and decreasing temperature. The average steady state flow stress for the three Al-Mg-Si alloys compressed under different deformation temperatures and strain rates are provided in Figure 5.5. An increase in the Mg-Si content was observed to

result in increased average flow stress for all deformation conditions as alloy 3 was observed to possess higher flow stress than alloy 1.

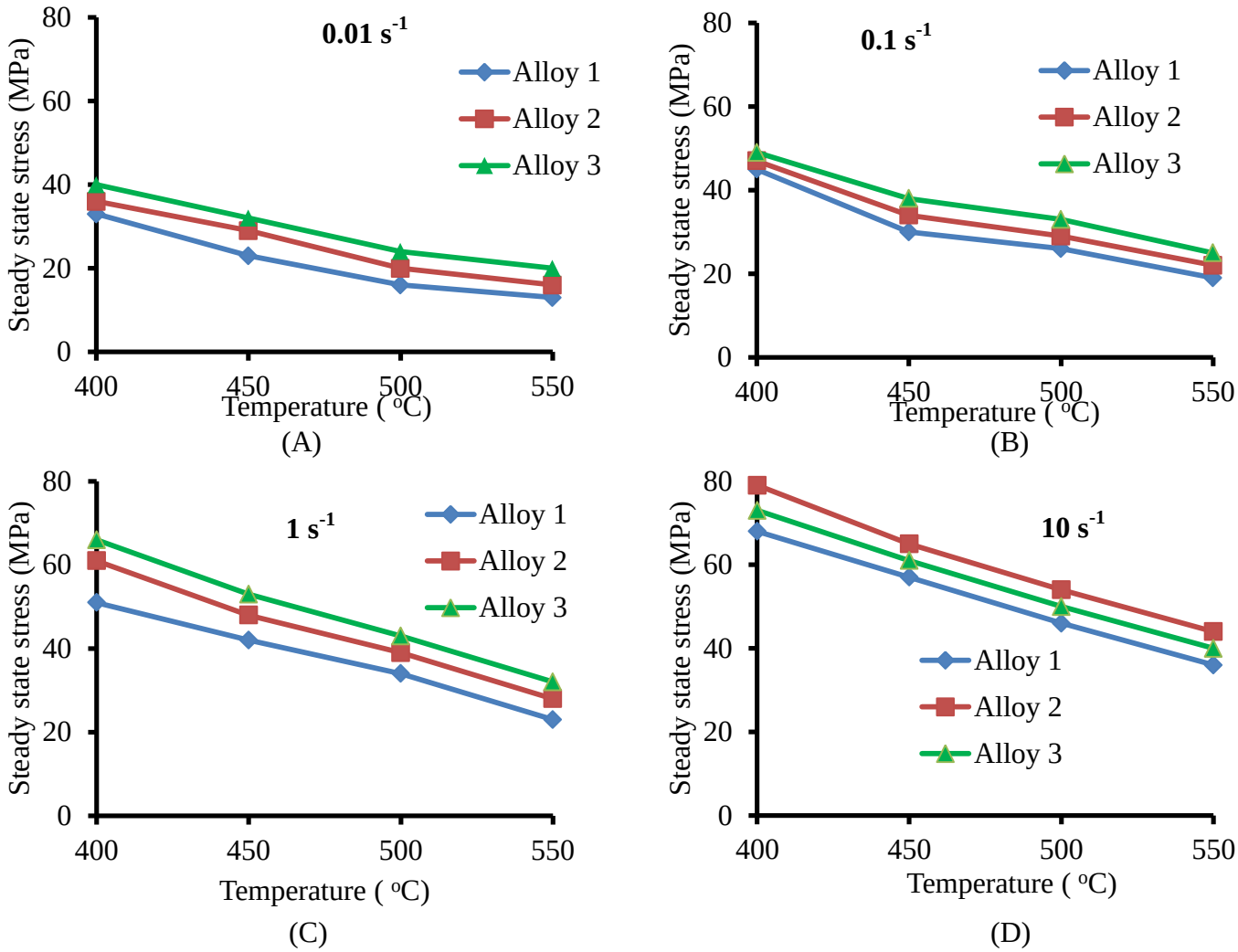

Figure 5.5: Average steady state stress vs temperature data

By comparing the average flow stress values of alloys 2 and 3 (equal Mg-Si content) deformed at low strain rates (0.01-1 s^{-1}), alloy 3 with 0.2 wt % Cr was observed to possess higher average flow stress. However, it is worth noting that for alloys 2 and 3 deformed at 10 s^{-1}; the presence of 0.2 wt % Cr did not necessarily translate into increased average flow stress as both alloys have comparable average flow stress values.

Constitutive model for hot flow stress behaviour

In order to effectively model the thermally activated hot flow stress deformation behavior of the Al-Mg-Si alloys, the hyperbolic sine law was used to quantify how the flow stress changes as a function of deformation temperature T (K) and strain rate $\dot{\varepsilon}$ (s^{-1}). The hyperbolic sine law is given as [73, 113]:

$$\sigma_{ss} = \frac{1}{\alpha_{ss}} \ln \left[\left(\frac{Z_{ss}}{A_{ss}}\right)^{\frac{1}{n_{ss}}} + \left(\left(\frac{Z_{ss}}{A_{ss}}\right)^{\frac{2}{n_{ss}}} + 1\right)^{\frac{1}{2}} \right]$$
$$\text{where } Z_{ss} = \dot{\varepsilon} \exp\left(\frac{Q_{ss}}{RT}\right) \qquad (5.2)$$

σ_{ss} is the steady state flow stress (MPa) and the parameter Q_{ss} (kJ/mol) refers to the deformation activation energy under steady state condition [114]. The hot deformation flow stress behavior of various engineering alloys has been determined using the hyperbolic sine law (Equation (5.2)) wherein the fit parameters A_{ss}, n_{ss}, Q_{ss} and α_{ss} were determined from experimental flow stress curves [113,114]. T refers to the deformation temperature (K) and R is the universal gas constant (R = 8.314 J/ (K mol)). n_{ss} is the mean slope of ln$\dot{\varepsilon}$ vs ln [sinh (ασ)] curve and the parameter α_{ss} can be calculated as:

$$\alpha_{ss} = \frac{\beta}{n_1} \qquad (5.3)$$

where β is obtained as the mean slope of the ln $\dot{\varepsilon}$ vs σ graph and n_1 represents the mean slope of ln$\dot{\varepsilon}$ vs ln σ graph [113]. The parameter Q_{ss} can be obtained by [73, 79, 113]:

$$Q = R\, n_{ss} \frac{\partial \ln[\sinh(\alpha\sigma)]}{\partial\left(\frac{1000}{T}\right)} \qquad (5.4)$$

where the partial derivative part of Eqn. (5.4) refers to the mean slope of ln [sinh (ασ)] vs $\frac{1000}{T}$ curves obtained at known constant strain rate. Using Eqns. (5.3) and (5.4), the material parameters α, n and activation energy for hot working (Q) for the Al-Mg-Si alloys studied in this research were determined.

$$\dot{\varepsilon} \exp(\frac{Q}{RT}) = A_{ss} [sinh(\alpha_{ss}\sigma)]^{n_{ss}} \quad (5.5)$$

The parameter A_{ss} may be obtained by substituting other known material constants into Eqn. (5.5) [115]. The relationship plots for determining the material parameters α, n and β for alloy 1 are shown in Figure 5.6.

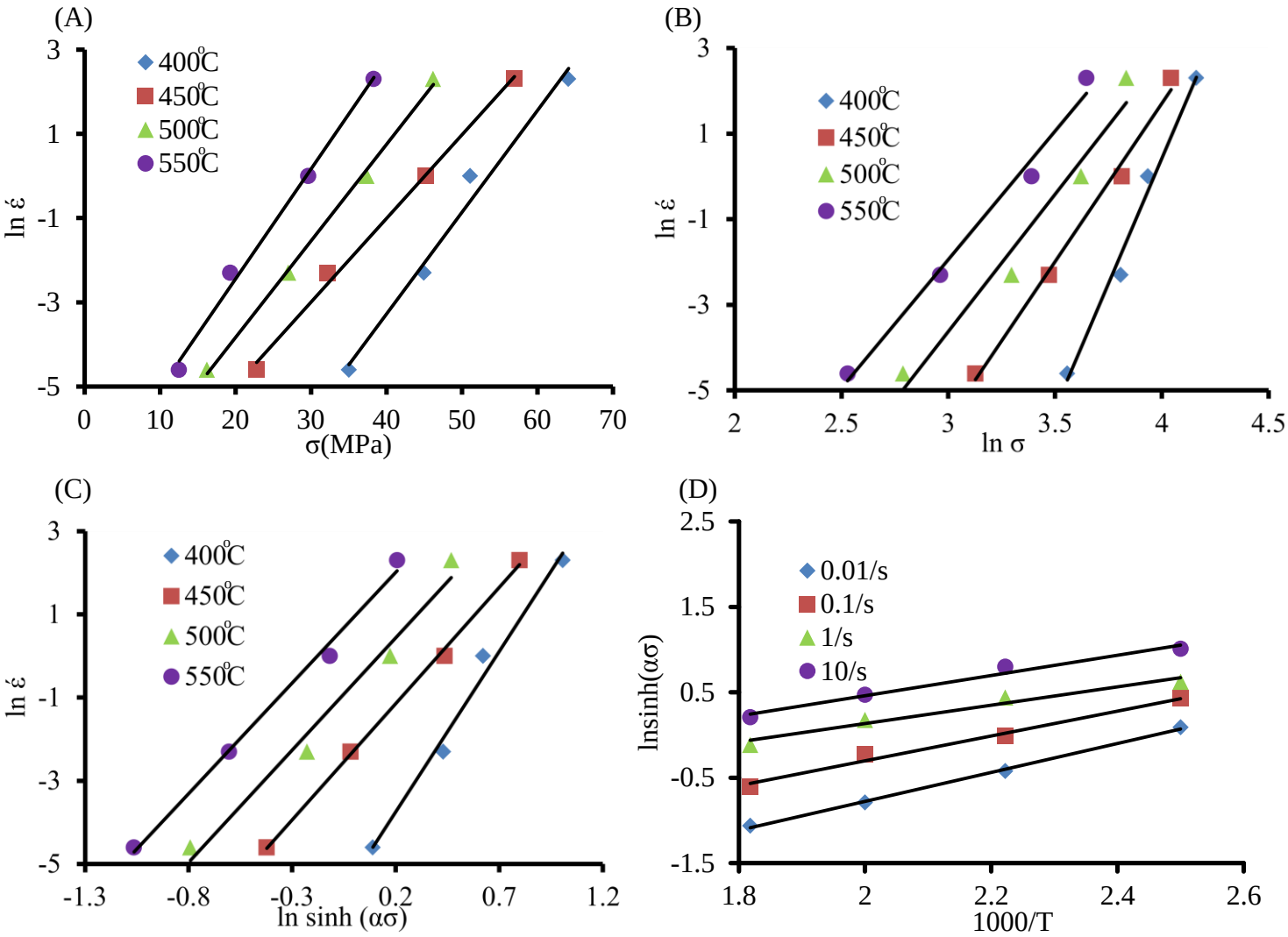

Figure 5.6: Relationship plots for alloy 1: (A) ln $\dot{\varepsilon}$ vs σ, (B) ln $\dot{\varepsilon}$ vs ln σ, (C) ln $\dot{\varepsilon}$ vs ln sinh (ασ), (D) ln sinh (ασ) vs $\frac{1000}{T}$

Upon taking the natural logarithm of both sides of the hyperbolic sine equation (Eqn. (5.2)) the parameter ln A is therefore obtained as the intercept of the ln Z vs ln [sinh (ασ)] plot. Using the power law equation proposed by Sellars and Tegart [116], the strain rate sensitivity parameter m

for each alloy was determined as the average slope of the ln σ vs ln $\dot{\varepsilon}$ plot. The relationship plots for determining the material parameter 'A' and strain rate sensitivity parameter 'm' for alloy 1 are shown in Figure 5.7 (A) and (B) respectively.

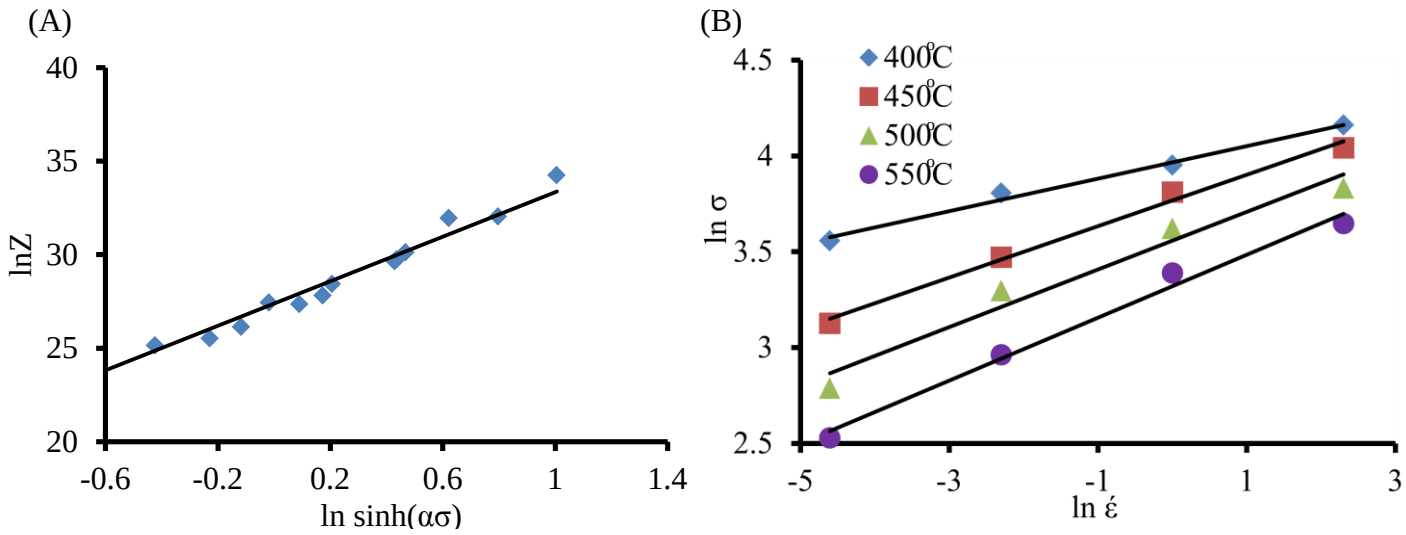

Figure 5.7: (A): ln Z vs ln (sinh (ασ)) plot with ln A as intercept, (B): ln σ vs ln $\dot{\varepsilon}$ plot for alloy 1

The material constants, activation energy and strain rate sensitivity parameter for the three alloys are shown in Table 5.1.

Table 5.1: Material parameters: activation energy values and strain rate sensitivity parameter

Alloy	Q (kJ/mol)	n	α $(MPa)^{-1}$	A (s^{-1})	m
1	178	6.70	0.027	7.78×10^{11}	0.133
2	171	4.96	0.027	9.72×10^{10}	0.126
3	197	6.70	0.025	6.35×10^{12}	0.111
4	125	4.08	0.041	4.21×10^{7}	0.179

The constitutive equations for predicting the hot flow stress behaviour of alloys 1, 2 and 3 based on the average of stress values from a true strain of 0.1 to 0.6 are therefore given respectively as:

$$\sigma = \frac{1}{0.027}\ln\left[\left(\frac{Z}{7.78\times10^{11}}\right)^{\frac{1}{6.7}} + \left(\left(\frac{Z}{7.78\times10^{11}}\right)^{\frac{2}{6.70}} + 1\right)^{\frac{1}{2}}\right] \quad (5.6)$$

$$\sigma = \frac{1}{0.027}\ln\left[\left(\frac{Z}{9.72\times10^{10}}\right)^{\frac{1}{4.96}} + \left(\left(\frac{Z}{9.72\times10^{10}}\right)^{\frac{2}{4.96}} + 1\right)^{\frac{1}{2}}\right] \quad (5.7)$$

$$\sigma = \frac{1}{0.025}\ln\left[\left(\frac{Z}{6.35\times10^{12}}\right)^{\frac{1}{6.7}} + \left(\left(\frac{Z}{6.35\times10^{12}}\right)^{\frac{2}{6.70}} + 1\right)^{\frac{1}{2}}\right] \quad (5.8)$$

In order to determine the accuracy of the developed models in predicting the hot flow stress behavior of the aluminum alloys over a wide range of conditions, the experimental average

steady flow stress data (shown in Figure 5.5) were compared with predicted values obtained using equations (5.6) – (5.8) for alloys 1, 2 and 3 respectively.

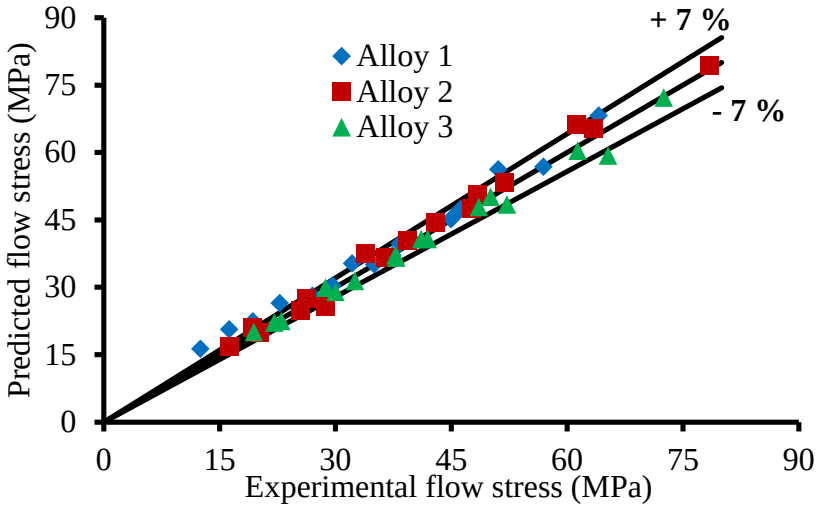

Figure 5.8: Comparison between predicted and experimental flow stress data at different deformation conditions

As shown in Figure 5.8, there exists good correlation between experimental and predicted data for the aluminum alloys tested in the current work. In order to quantitatively measure the predictive accuracy of the developed constitutive equation for determining the flow stress behavior of the aluminum alloys during hot deformation, the average absolute relative error (AARE) was calculated as a function of σ_p (predicted) and σ_{exp} (experimental) flow stress values [117]:

$$\text{AARE} = \frac{1}{N}\sum_{i=1}^{i=N}\left|\frac{\sigma_{exp}^{i}-\sigma_{p}^{i}}{\sigma_{exp}^{i}}\right| \times 100\% \qquad (5.9)$$

The AARE values for alloys 1, 2 and 3 were found to be 7.2 %, 5.4 % and 3.6 % respectively. This indicates that the hyperbolic equations (5.6) – (5.8) can effectively predict the hot flow stress behaviour of alloys 1, 2 and 3 respectively.

Effect of alloy composition on flow stress, activation energy and strain rate sensitivity

As seen in Table 5.1, alloy 3 with 0.2 wt % Cr has a higher activation energy (Q) value in comparison with alloy 2 possessing equal Mg and Si content but no Cr. Also, 0.2 wt % Cr addition was discovered to result in an increase in the average steady flow stress for deformations at low strain rates (0.01-1 s^{-1}, compare alloys 2 and 3). Aluminum alloys are known to gain strengthening via mechanisms such as cold working or work hardening, precipitation hardening, solid solution strengthening and grain refinement. The role of transition elements as grain refiners has been widely reported in literature [118-120]. It is believed that the higher and lower flow stress of alloy 3 in comparison to alloy 2 at low strain rates (0.01 -1 s^{-1}) and high strain rate (10 s^{-1}) respectively is not attributable to the grain refining role of Cr as grain refinement is expected to result into further strengthening and not a drop in flow stress. Also, this flow stress behavior in alloy 3 cannot be attributed to precipitation hardening (deformation conditions not similar to aging treatment and complete dissolution of Mg_2Si occurs just above 500 ^oC, see Figure 5.36) and work hardening effect (no evidence of this mechanism in the flow stress curves shown in Figure 5.4 as equilibrium is quickly reached between softening and work hardening mechanisms).

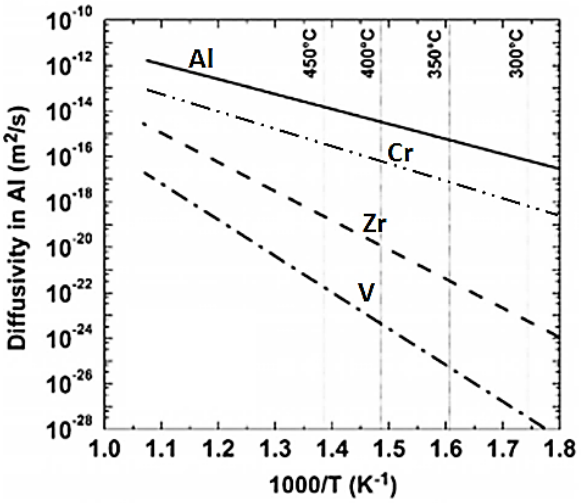

Figure 5.9: Diffusivity of transition elements in aluminum as a function of temperature [121]

Solid solution strengthening involves strengthening of Al alloys resulting from the dislocation blocking role of foreign atoms of elements in the crystal lattice of aluminum. In Cr containing alloys, Cr solute diffusion contributes to the hot deformation kinetics process and may be responsible for the increase in flow stress and activation energy. Figure 5.9 shows the diffusivity of Cr and other transition elements in aluminum as a function of temperature. For specific temperature, Cr has a lower diffusivity in aluminum in comparison to aluminum self-diffusion. During the deformation process, the presence of solute atoms that diffuse less rapidly in aluminum in comparison with aluminum self-diffusion rate have been found to result into strengthening due to such solute atoms serving as barriers to dislocation movement [122,123]. Cr solute atoms segregate at subgrain boundaries resulting into reduction in the energy possessed by dislocations [124]. The pinning of dislocations at subgrain boundaries implies that an increase in applied stress will be required to free dislocations. The continued blocking of dislocations by Cr solute atoms result in the multiplication of static dislocations since dislocations already blocked by Cr solute atoms now serve as barriers to the mobility of other dislocations [125]. During hot deformation compression, the recovery process is hindered by higher solute atom vacancy binding energy which reduces vacancies available for dislocation climb and hence a decrease in dislocation mobility [126]. This result into an increase in the activation energy required for hot deformation. In their studies on creep behaviour of aluminum alloys, Rummel et al. [124] observed that the lower diffusivity of Cr in aluminum in comparison to aluminum self-diffusion is usually associated with higher activation energy in aluminum alloys with Cr content. The diffusivities of magnesium and silicon in aluminum were determined as a function of temperature by using an Arrhenius relationship proposed by Langkruis et al. [111] and given as:

$$D_i = D_i^0 \exp\left(-\frac{Q_i^d}{RT}\right) \qquad (5.10)$$

where D_i is the diffusivity of an element in aluminum matrix, R is the universal gas constant, Q_i^d is the activation energy for diffusion of element *i* in aluminum. T represents temperature (K) and D_i^0 is the diffusion parameter for element *i*. Fujikawa [127] experimentally determined parameters D_i^0 and Q_i^d for various elements. The diffusivity values for Mg, Si and Cr in aluminum at different temperatures were calculated using equation (5.10) and are shown in Table 5.2.

Table 5.2: Mg, Si and Cr diffusivities (D) (m^2/sec) in aluminum as a function of temperature

Temperature (^oC)	D_{Mg}	D_{Si}	D_{Cr}
400	1.16×10^{-14}	5.67×10^{-15}	3.11×10^{-16}
500	2.05×10^{-13}	1.31×10^{-13}	1.38×10^{-15}
550	6.63×10^{-13}	4.73×10^{-13}	2.69×10^{-15}

Sherby and Ruano [123] reported that the diffusion coefficient or diffusivity of solute atoms in aluminum matrix is inversely proportional to the deformation resistance of dilute solid solution aluminum alloys. Table 5.2 shows that Cr has the least diffusivity in aluminum of the three elements available as solute atoms in the alloys studied and therefore the presence of its solute atoms in the Al matrix is expected to be accompanied by the highest deformation resistance. This may therefore explain the trend observed in the activation energy values for the alloys studied in this work as Mg atoms dissolve faster in Al matrix than Si and Cr solute atoms. This implies that at specific deformation temperature, there exist fewer Mg solute atoms in Al matrix serving as dislocation blocking barriers in comparison to Si and Cr solute atoms. As seen in Table 5.1, 0.2 wt % Cr addition has a higher influence on activation energy than Mg-Si increase. The activation energy Q was observed to increase with increase in the Mg-Si content (178 kJ/mol in alloy 1 to 197 kJ/mol in alloy 3). However, alloy 2 (Q = 171 kJ/mol) with higher Mg-Si content and no Cr addition has a lower activation energy in comparison with alloy 1 where 0.2 wt % Cr is present. Alloy 3 with high Mg-Si content and 0.2 wt % Cr possesses the highest activation energy and

flow stress values (during low strain rate deformation) while alloy 2 with high Mg-Si content and no Cr content possess the highest average flow stress value during high strain rate deformation.

The strain rate sensitivity parameter was observed to reduce with increase in the Mg-Si content as well as with addition of 0.2 wt. % Cr. Alloy 3 with 0.6 wt % Si, 0.9 wt % Mg and 0.2 wt % Cr has the least strain rate sensitivity parameter of the three alloys studied in this work. This is consistent with available literature in which elemental additions have been observed to result in reduction of the strain rate sensitivity of aluminum alloys [128]. Ozturk et al. [129] also reported an increase in the strain rate sensitivity parameter for AA6061 due to reduction in the amount of free solute atoms. During deformation process, dislocations are arrested at obstacles such as clusters of mobile solute atoms [128,117]. The pipe diffusion of these solute atoms encourages the creation of a dislocation atmosphere. However, an increase in deformation strain rate results into less dislocation arrest time which leads to dislocation freedom and therefore less stress required to accommodate applied strain [128]. The higher diffusivities of Mg and Si (compared to Cr) in aluminum implies that Mg and Si diffusion are less sensitive to reduction in dislocation arrest time associated with strain rate increase. This indicates that during low strain rate deformation (0.01-1 s^{-1}), there exists more time for Cr solute atoms to arrest dislocations and this may be responsible for the higher flow stress of alloy 3 (with Cr) in comparison with alloy 2 (no Cr). However, at higher deformation strain rate (10 s^{-1}); Cr dislocation arrest effect becomes minimal resulting into comparable average flow stress values for alloys 2 and 3.

Summary

Hot compression deformation tests of select Al-Mg-Si alloys were performed on a Gleeble 3500 thermomechanical simulator at various temperatures (400-550 ^{o}C) and strain rates (0.01-10 s^{-1}). The following conclusions can be made:

(I) For all tested alloys, the average steady flow stress increases with increasing strain rate and decreasing deformation temperature. For all deformation conditions, alloy 1 (0.5Mg, 0.5Si, 0.2Cr) displayed the lowest average steady flow stress value. Alloy 3 (0.9Mg, 0.6Si, 0.2Cr) exhibited the highest flow stress at strain rates up to 1 s^{-1} while alloys 2 and 3 displayed comparable average flow stress values at $10s^{-1}$.

(II) Hot deformation activation energy was observed to increase from 178kJ/mol in alloy 1 to 197 kJ/mol in alloy 3 with higher Mg-Si content. Also, addition of 0.2 wt % Cr was discovered to increase the activation energy for hot deformation in alloy 3 in comparison with alloy 2 with no Cr content.

(III) An increase in the Mg-Si content and addition of 0.2 wt % Cr were observed to result in decreasing strain rate sensitivity parameter. The reduction in dislocation arrest time due to increase in deformation strain rate may be responsible for reduced Cr solute atom strengthening in alloy 3.

5.1.2 Effect of Mg-Si solute content

The influence of hold time on Mg-Si solute content level during pre-deformation heating of a homogenized Al-Mg-Si alloy (alloy 4) has been determined and the Mg-Si solute content (X) integrated into a constitutive equation for predicting the hot flow stress behavior of Al-Mg-Si alloys. The developed constitutive equation was validated against experimental measurements and also compared to existing data available in the literature on hot flow stress behavior of Al-Mg-Si alloys. The detailed experimental procedure is described in section 4.2.1. The developed mathematical model applied in determination of the Mg-Si solute content as a function of hold time (s) and deformation temperature (^{o}C) is discussed in section 4.3.1 and appendix A. The

material parameters α, n and activation energy for hot working (Q) for the Al-Mg-Si (alloy 4) alloy studied in this research were determined as described in section 5.1.1.

Flow stress curves

The hot compression stress-strain curves for samples held for 60 seconds at test temperature prior to deformation are shown in Figure 5.10.

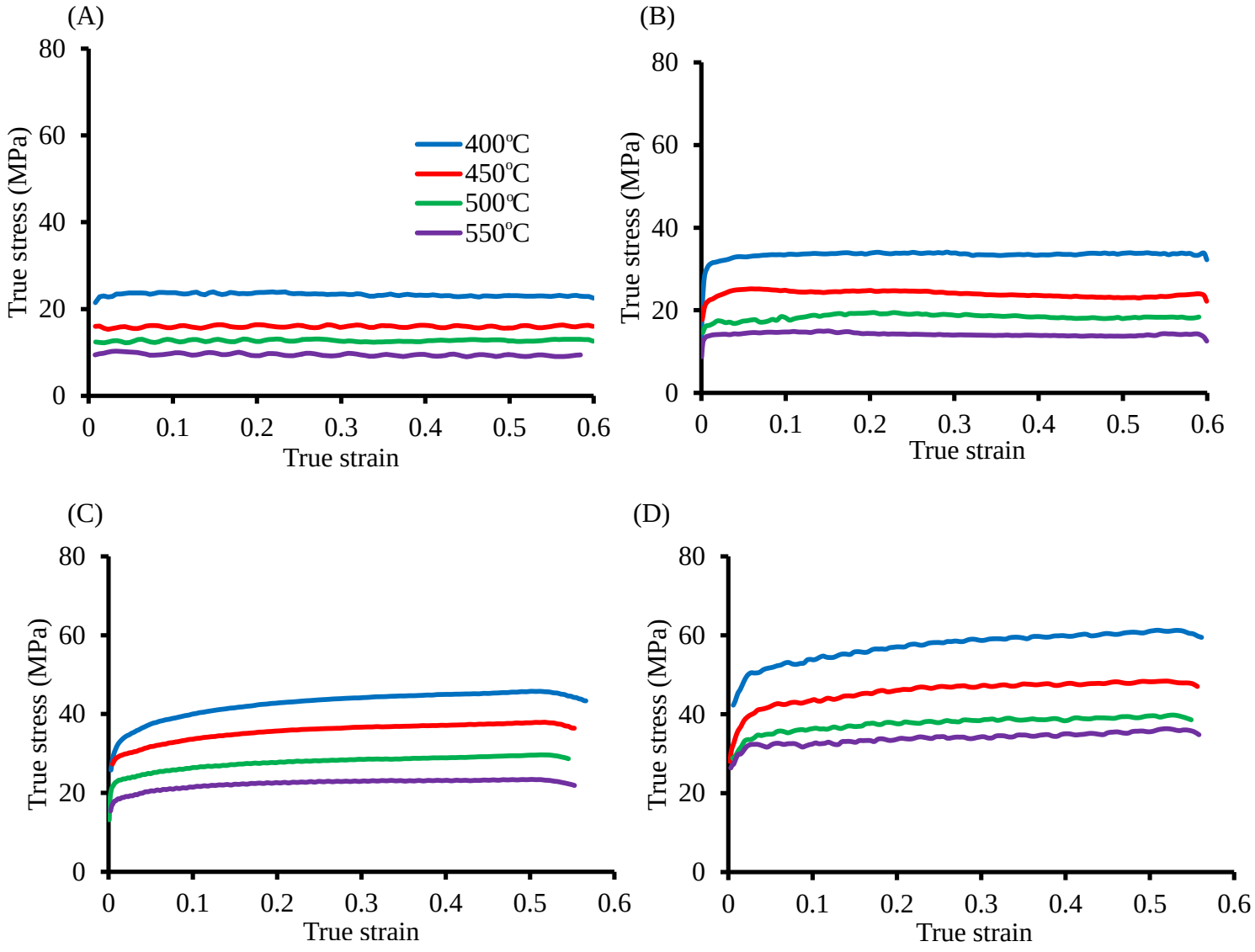

Figure 5.10: Stress-strain curves of alloy 4 during hot compression deformation (A): 0.01 s^{-1} (B): 0.1 s^{-1} (C): 1 s^{-1} (D): 10 s^{-1}

At a constant deformation temperature, the average flow stress was observed to increase with increasing strain rate. However, the flow stress decreases with increasing temperature at a

constant strain rate. The average experimental steady state flow stress for different conditions was determined from experimental flow stress curves as the average stress from true strain of 0.1 to 0.6.

Constitutive model for hot deformation

The Mg and Si solute content for specific deformation temperature and hold time were determined from the particle dissolution model described in Appendix A. In the literature, the parameter A_{ss} is obtained by substituting other known material constants into Eqn. (5.2) [115]. However for current research, the parameter A_{ss} was determined as a function of the amount of Mg and Si in solid solution [74]:

$$A_{ss} = \exp(k_1)\exp(-k_2 X) \quad (5.11)$$

The parameter A_{ss} has been determined to depend explicitly on the weighted Mg and Si solute content (represented as X) in the aluminum alloy matrix, defined as [71, 74]:

$$X = 2[\mathrm{Mg}] + [\mathrm{Si}] \quad (5.12)$$

[Mg] and [Si] are respectively Mg and Si solute content in alloy matrix and were determined as a function of the temperature and hold time in current research using the one dimensional particle dissolution model. The parameters k_1 and k_2 are model parameters obtained by plotting $n_{ss}\ln(\sinh(\alpha_{ss}\sigma_{ss})) - \ln(Z_{ss})$ against X [75]. The applied hyperbolic sine equation which is dependent on the Mg-Si solute content (X) is obtained by inserting Eqn. (5.11) into Eqn. (5.2). This modified hyperbolic sine equation is given as [79]:

$$\sigma_{ss} = \frac{1}{\alpha_{ss}} \ln\left[\left(\frac{Z_{ss}}{\exp(k_1)\exp(-k_2 X)}\right)^{\frac{1}{n_{ss}}} + \left(\left(\frac{Z_{ss}}{exp(k_1)\,exp(-k_2 X)}\right)^{\frac{2}{n_{ss}}} + 1\right)^{\frac{1}{2}}\right] \quad (5.13)$$

For an average Mg_2Si initial particle size, $r_o = 0.5$ μm in the alloy, the weighted solute content X was determined using Eqn. (5.12). At constant temperature and hold time, the solute content X

increases with decreasing average initial particle size r_o due to faster dissolution of Mg_2Si particles with smaller initial particle radius. However, at temperatures ≥ 500 ^oC, the particle dissolution process occurs very rapidly such that the particle size has negligible effect on amount of Mg that dissolves with time (Figure A3 in appendix A).

Using data from the flow stress curves shown in Figure 5.10 and the developed particle dissolution model; the material parameter A_{ss} was determined by Eqn. (5.11). The material parameters α, n and activation energy for hot working (Q) for alloy 4 were determined as described in section 5.2. The model parameters determined experimentally in this research are shown in Table 5.3.

Table 5.3: Determined parameters utilized in this research

Q_{ss} (kJ/mol)	α_{ss} (MPa^{-1})	n_{ss}	k_1	k_2 (wt. $\%^{-1}$)
125	0.041	4.08	19.1-21.02	2.24

Table 5.4 shows model parameters for the constitutive relation used in predicting the hot flow stress behavior of alloy 4 in this work as compared to the available literature data for AA6063 alloy. The determined constitutive parameters α_{ss}, Q_{ss} and n_{ss} were utilized in modeling the thermo-mechanical history of alloy 4 extruded at 485 ^oC. The extrusion modelling result is shown in Appendix B.

Table 5.4: Comparison of fitting parameters for alloy 4 with available literature data for AA6063

Fitting parameter	Current work	Literature
Q_{ss} (kJ/mol)	125	115-180 [72-75]
n_{ss}	4.08	3.05-6.5 [73-74]
α_{ss} (MPa^{-1})	0.041	0.01-0.09 [73-75, 117]
A_{ss} (s^{-1})	1.97×10^7- 1.3×10^9	$2 \times 10^7 – 8 \times 10^{10}$ [74-75]

As seen in Table 5.4, the constitutive parameters applied for predicting the hot deformation flow stress behavior of alloy 4 fits well within available literature data for AA6063 alloy.

Validation of particle dissolution model

In order to validate the particle dissolution model, the electrical resistivity of alloy 4 samples held at 450 ^{o}C for different times followed by water quenching was measured. The relationship between elemental (Si, Mg, Fe and Cu) weight percent in solid solution and the electrical resistivity of Al-Mg-Si alloys has been studied and given by Matthiessen's rule as [130]:

$$\frac{1}{k} = 0.0267 + 0.032Fe_{ss}\ \% + 0.0068Si_{ss}\ \% + 0.0052Mg_{ss}\% + 0.0033Cu_{ss}\% \quad (5.14)$$

where $\frac{1}{k}$ is the resistivity of the alloy; Fe_{ss}, Si_{ss}, Mg_{ss} and Cu_{ss} are the weight percent of the respective elements in solid solution. Alloy 4 has a low Cu content (< 0.01 %) and therefore Cu in solid solution has minimal contribution to the electrical resistivity of the alloy. Mg and Si particle dissolution are therefore significant contributors to the measured electrical resistance of the alloy as Fe forms second phase intermetallics and has negligible solubility (~0.04 %) in aluminum alloys [130].

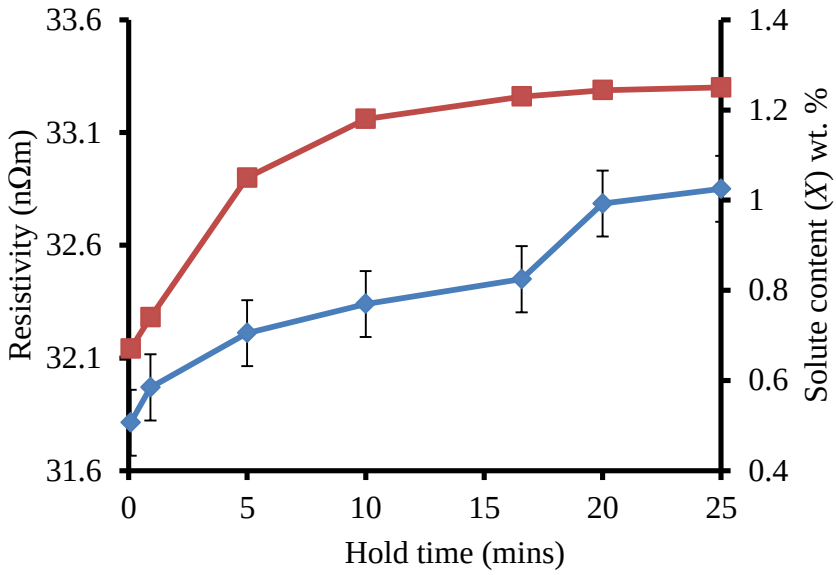

Figure 5.11: Measured resistivity and model predicted solute content for alloy 4 samples

Figure 5.11 shows the measured resistivity as well as the model predicted solute content for alloy 4 samples held at 450 ^{o}C for different times. The resistivity of alloy 4 was observed to increase with increasing hold time. Olaffson et al. [131] showed that alloying elements in solid solution have the highest contribution to alloy electrical resistivity by causing electron mobility disturbance.

Comparison of experimental and predicted steady state flow stress

In order to determine the accuracy of the developed model in predicting the hot flow stress behavior of alloy 4 over a wide range of conditions, the solute content (X) was determined for specific hold time and test temperature based on the particle dissolution model discussed earlier assuming an average particle size r_o = 0.5 μm. The average steady flow stress for different deformation conditions was then determined by Eqn. (5.13) and using data shown in Table 5.3.

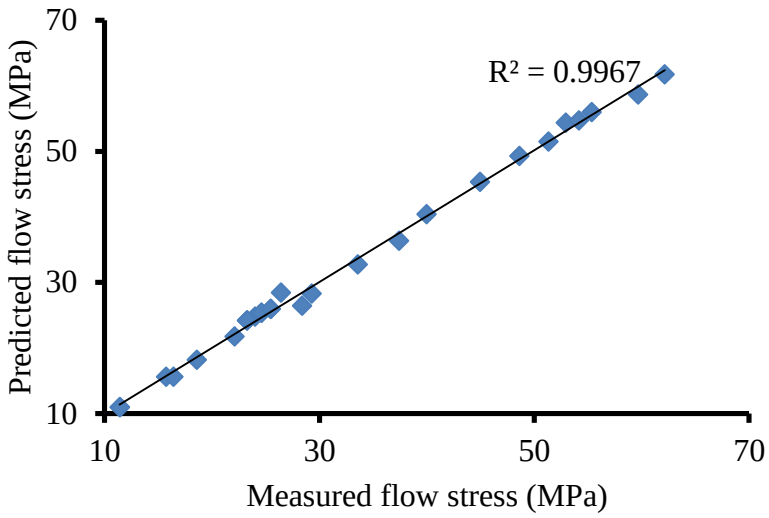

Figure 5.12: Comparison between predicted and experimental flow stress data in different deformation conditions for alloy 4

As seen in Figure 5.12, there exists good correlation between experimental and predicted data for the Al-Mg-Si alloy tested in the current work. In order to verify the predictive ability of the new model to predict the flow stress behavior of Al-Mg-Si alloys over wide range of deformation

conditions, the average hot steady flow stress of various Al-Mg-Si alloys with similar elemental weight composition were predicted. The average predicted flow stress values were compared to the experimental flow stress data available in literature for these alloys. The solute content for different deformation conditions was determined based on an average particle size r_o = 0.5 μm. In their studies on effect of heating rate on Mg_2Si dissolution during hot deformation compression of AA6063 alloy, Langkruis et al. [111] showed extensively that prediction of Mg solute content as a function of heating rate varies only for particles with average particle size less than 0.5 μm.

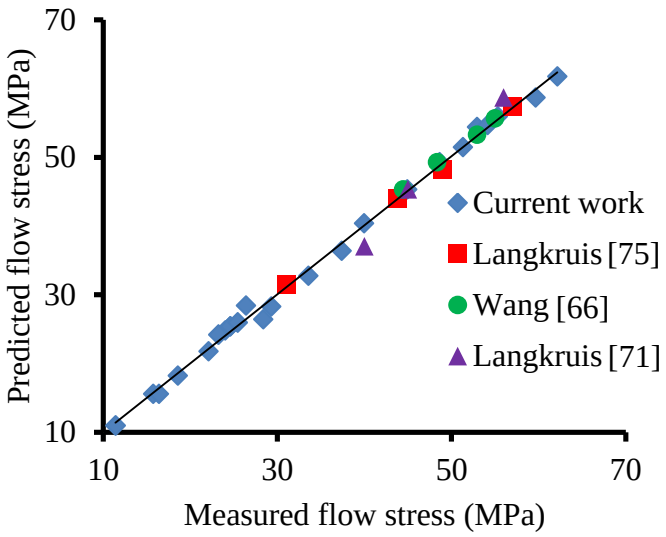

Figure 5.13: Comparison between predicted and measured flow stress under various conditions

Figure 5.13 shows the model predictions as compared to the measured steady state flow stress for this work as well as experimental data from the literature. As shown, predictions determined using current model match the experimental measurements available in literature.

Effect of hold time on flow stress behavior

The effect of hold time on the flow stress behavior of alloy 4 was determined by performing hot compression deformation tests at 450 ^oC and 10 s^{-1} after hold times of 1, 5, 12.5, 16.6 and 25 min. The hot compression tests were performed thrice in order to ensure

repeatability and ascertain differences in measured flow stress for the given deformation conditions. Figure 5.14 shows that the average experimental steady flow stress during the deformation increases with increasing hold time.

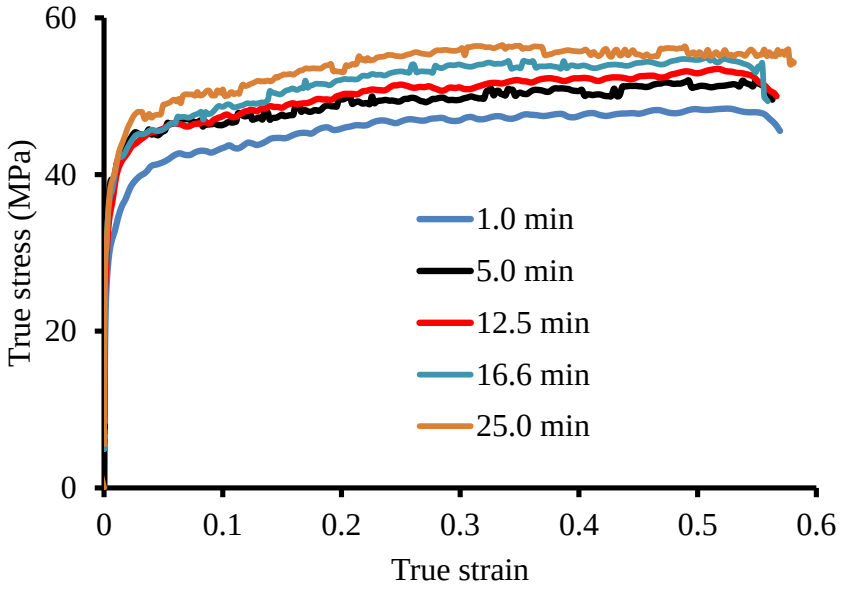

Figure 5.14: Measured stress-strain curve (450 ^{o}C, 10 s^{-1} after different hold times)

The effect of hold time can be verified by comparing the stress-strain curves obtained for hold times of 1 and 25 min i.e. a 14.5 % increase in flow stress due to an increase in hold time. The increase in average flow stress due to increase in hold time at deformation test temperature is attributed to an increase in the Mg-Si solute content with increasing hold time. During extrusion of AA6063 alloy, Zhu et al. [6] reported that an increase in the amount of Mg-Si dissolved in solid solution usually has a strong influence on the alloy's resistance to deformation. The average steady state flow stress for deformation at 450 ^{o}C and 10 s^{-1} after different hold times was predicted using Eqn. (5.13), parameters in Table 5.3 and the solute content X determined via the particle dissolution model shown in Appendix A.

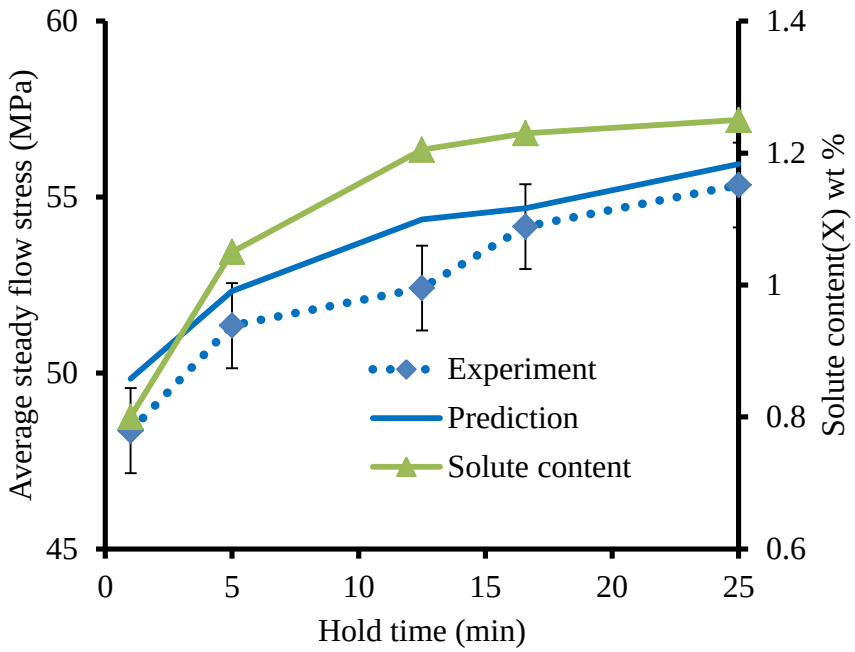

Figure 5.15: Effect of hold time on solute content and average steady state flow stress (450 ^{o}C, 10 s^{-1})

The Mg-Si solute content after heating up to 450 ^{o}C was determined as X = 0.8, 1.05, 1.205, 1.23 and 1.25 for hold time t = 1, 5, 12.5, 16.6 and 25 min respectively. The average experimental steady state stress values obtained from Figure 5.14 were compared with predicted flow stress values. As seen in Figure 5.15, the predicted flow stress values compare well with the average experimental values. The developed constitutive model can predict the average flow stress as a function of the solute content – a parameter that varies with hold time at test temperature. Figure 5.15 shows that the average measured flow stress of the deformed alloy 4 was observed to increase with increasing hold time and Mg_2Si solute content (X) prior to deformation. In order to further prove the importance of accounting for solute content as a function of hold time in development of constitutive equation for predicting the hot deformation flow stress behavior of Al-Mg-Si alloys; the parameter A_{ss} was determined simply as a fit parameter (Eqn. (5.5)) and also as a function of the solute content (varies with hold time, Eqn. 5.11). The predicted flow

stress for different deformation conditions was thereafter determined by using Eqns. (5.2) and (5.13) respectively.

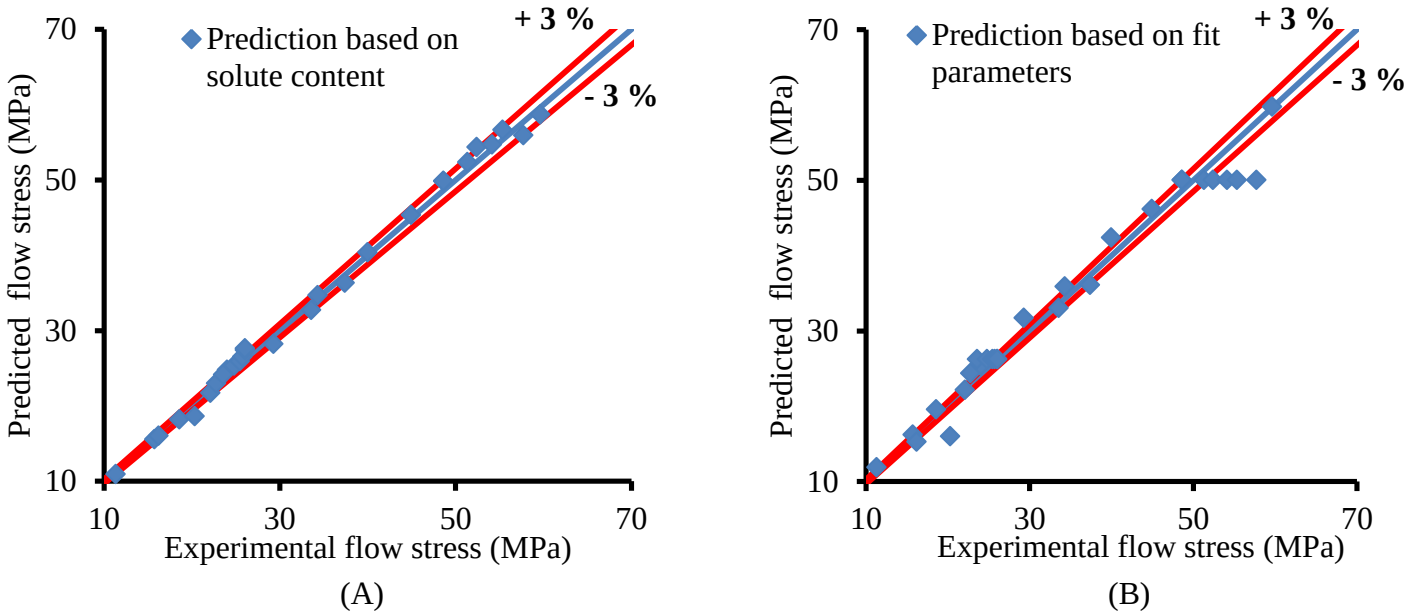

Figure 5.16: Comparison of measured and predicted flow stress for alloy 4 (A): A_{ss} obtained by Eqn. (5.11), (B): A_{ss} obtained by Eqn. (5.5)

Figure 5.16A shows predicted flow stress values obtained by accounting for the solute content in the constitutive equation (Eqn. (5.13)) vs experimental flow stress values while the predicted flow stress values in Figure 5.16B were determined based on fit parameters obtained from the experimental flow stress curve. As seen in Figure 5.16, the developed constitutive model which accounts for solute content (X) as a function of hold time is better matched to test data and is therefore a more reliable tool for prediction of the flow stress behavior of Al-Mg-Si alloys. In order to quantitatively measure the predictive accuracy of the developed constitutive equation for determining the flow stress behavior of Al-Mg-Si alloys during hot deformation, the average absolute relative error (AARE) was calculated using Eqn. (5.9). For the developed constitutive model which involves accounting for solute content as a function of hold time, AARE = 3.4 %. However, for flow stress prediction performed without accounting for solute content (i.e. only fit parameters), AARE = 9.6 %.

A solute dependent constitutive equation has been developed for the modeling of the hot flow stress behavior of an Al-Mg-Si alloy. Using a one-dimensional particle dissolution model, the influence of Mg and Si solute content during pre-heating on the deformation resistance of the alloy has been determined.

5.2 Extrudability

In this section, the influence of alloy composition and extrusion temperature on the extrudability of alloys 1 - 4 is discussed. Cylindrical extrusion samples of alloys 1 - 4 with dimensions ϕ76 mm × 89 mm were extruded into strip profiles measuring 1.9 mm in thickness and 53.3 mm in width. The detailed extrusion trial procedure including the starting billet size and extrusion profile shape are discussed in section 4.2.2.

In order to detect temperature changes during the extrusion process, thermocouples were installed in the die, container, billet and ram sections. Figure 5.17 shows the temperature history experienced by these sections during the extrusion of alloy 3 at 500 ^{o}C.

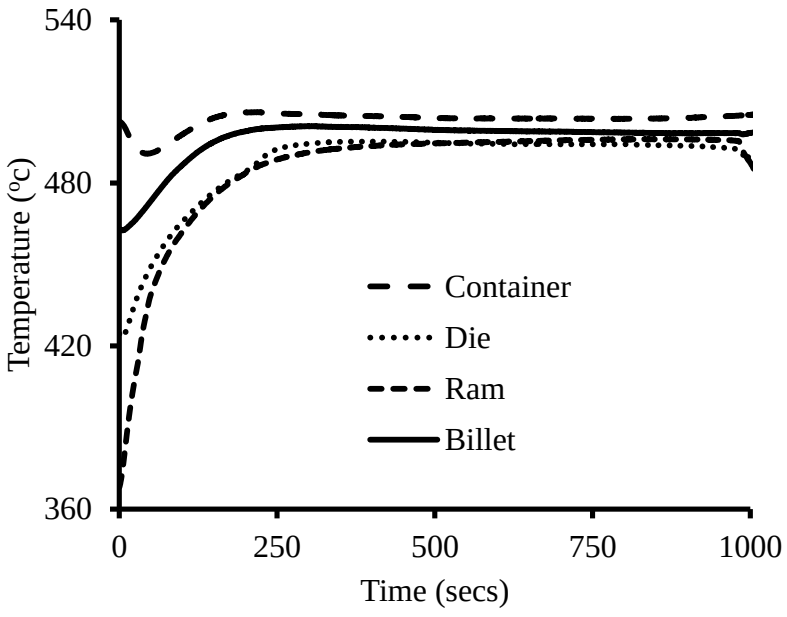

Figure 5.17: Temperature vs time plot for alloy 3 during extrusion at 500 ^{o}C

As seen in Figure 5.17, the die, container, billet and ram sections were observed to reach steady state temperature after about 4 minutes. These sections were observed to maintain steady state temperature during the extrusion process i.e. $\Delta T = 0$ during the extrusion process.

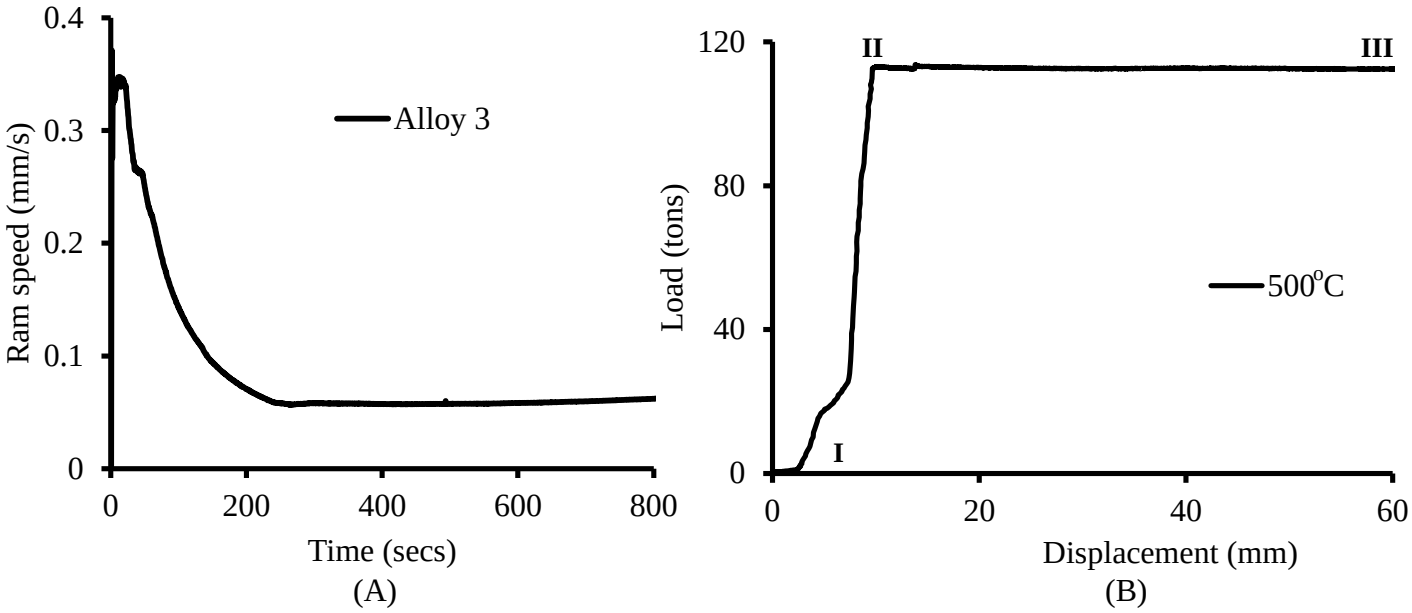

Figure 5.18: (A): Velocity vs Time graph; (B) Load vs Displacement graph for alloy 3

The velocity–time plot obtained during the extrusion of alloy 3 at 500 ^{o}C is shown in Figure 5.18(A). During the initial stages of the extrusion process, the ram speed increases to a maximum followed by a drop to steady state as the ram starts pushing the billet through the die orifice. The initial increase in ram speed corresponds to the time during which there is no contact between the ram and the billet i.e. no obstacle in the path of travel of the ram hence the increase in its speed as it travels towards the billet. The actual ram speed during the extrusion of the billet therefore corresponds to the steady state speed obtained once contact is made between the ram and the billet. The load-displacement plot obtained during the extrusion of alloy 3 at 500 ^{o}C is shown in Figure 5.18(B). The container is filled with the billet to be extruded prior to the stage labelled I in Figure 5.18B. During stage I-II, the die becomes filled with the material to be extruded and

this result into a pressure build up. The required load is reached at stage II with the actual extrusion i.e. the profile exiting the die orifice occurring during the steady state section II-III.

Effect of alloy composition on extrudability

The extrudability of alloys 1, 2 and 3 were determined as a function of the required extrusion breakthrough load and ram speed during the extrusion process. The load vs displacement graphs obtained during the extrusion of alloys 1, 2 and 3 at 500 ^{o}C are shown in Figure 5.19.

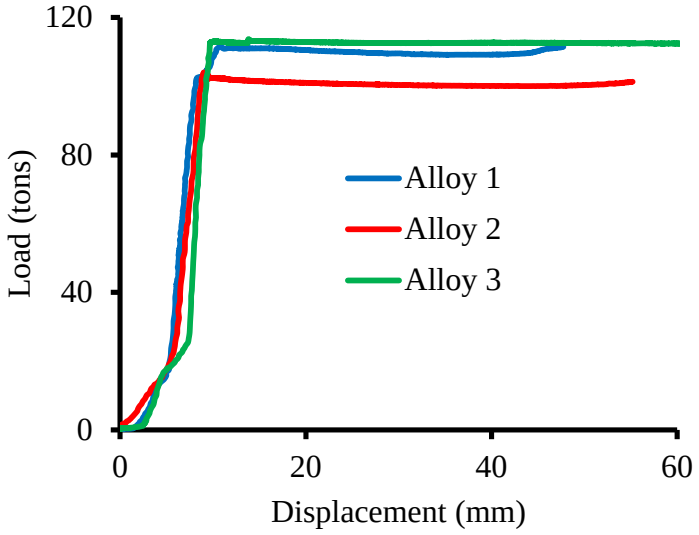

Figure 5.19: Load vs displacement graph for alloys 1 and 2 extruded at 500 ^{o}C

As seen in Figure 5.19, the extrusion load was observed to reach steady state after an initial increase with displacement. The extrusion trials were conducted three times in order to ensure repeatability and consistency in acquired data. The breakthrough load required for successful extrusion of alloys 1 - 4 are shown in Figure 5.20 and were extracted as the steady state load (i.e. stage II-III in Figure 5.18B) from the load- displacement data. Alloy 2 (0.6 wt. % Si, 0.9 wt. % Mg and no Cr content) was observed to require the least extrusion load of alloys 1, 2 and 3. Addition of 0.2 wt. % Cr results in a drop in extrudability of the Al-Mg-Si alloys as the load required to extrude alloy 2 was observed to be lower than that for alloy 3.

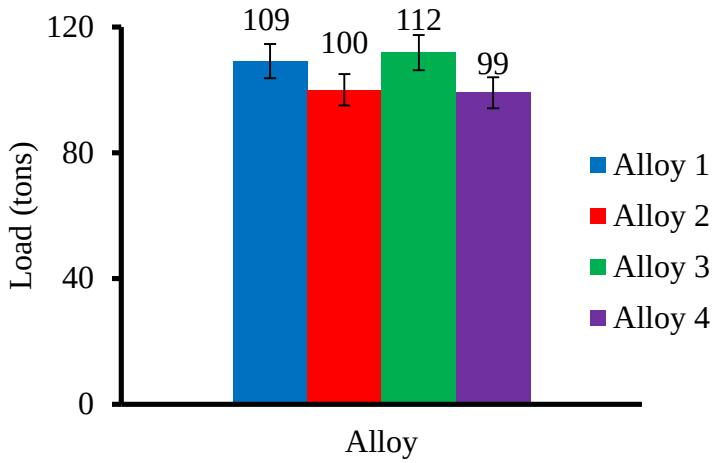

Figure 5.20: Required extrusion load for alloys 1-4 extruded at 500 ^{o}C

By comparing the load required to extrude alloy 3 (112 ton) and alloy 1 (109 ton), extrudability was observed to reduce with an increase in Mg and Si content.

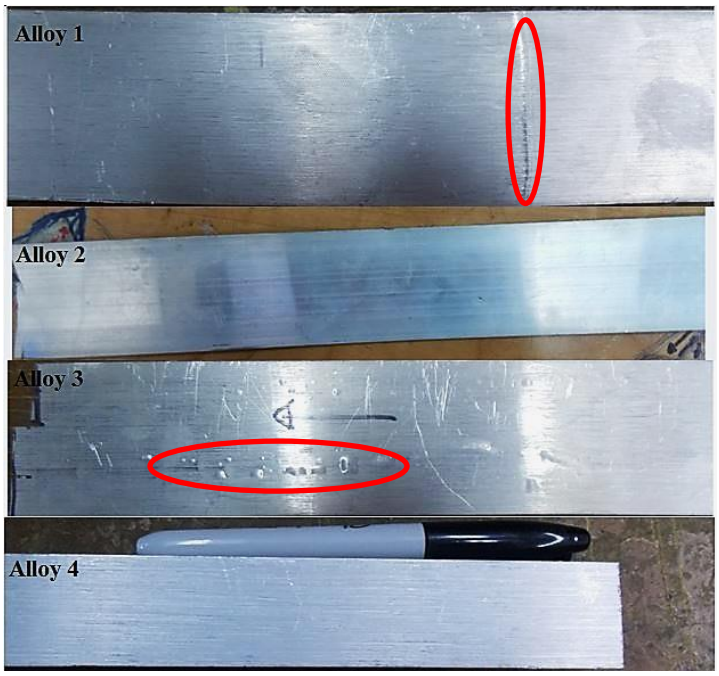

Figure 5.21: Surface quality of alloys 1 – 4 after laboratory scale extrusion at 500 ^{o}C

As seen in Figure 5.21, the extruded profile of alloys 2 and 4 were observed to have better surface finish as the extruded surface of alloys 1 and 3 were observed to have rough patches and small surface tears (shown in red). The ram speed during the extrusion process was also measured as an indication of the extrusion rate i.e. the exit velocity of the extruded profile.

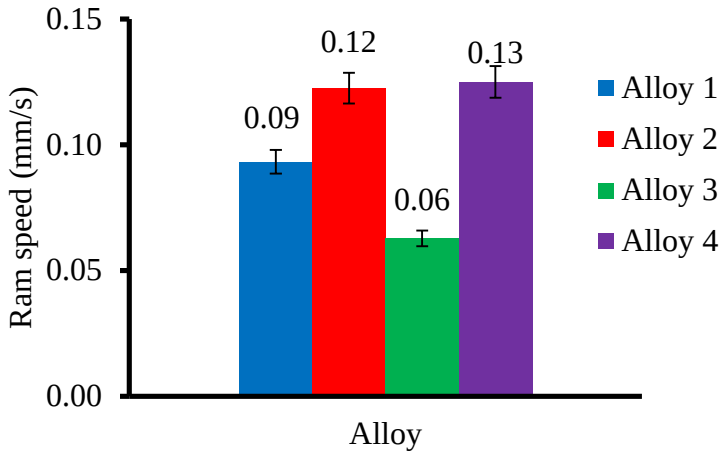

Figure 5.22: Ram speed for alloys 1 - 4 extruded at 500 ^{o}C

The ram speed obtained as the steady state speed (as shown in Figure 5.18A) during the extrusion of alloys 1-4 is shown in Figure 5.22. The ram speed was lowest during extrusion of alloy 3 and highest for alloy 4. This indicates that an increase in the Mg-Si content and 0.2 wt. % Cr addition result in reduction of the exit velocity of the extrusion.

Effect of extrusion temperature on extrudability

The effect of extrusion temperature on ram speed for alloys 1 - 3 is shown in Figure 5.23

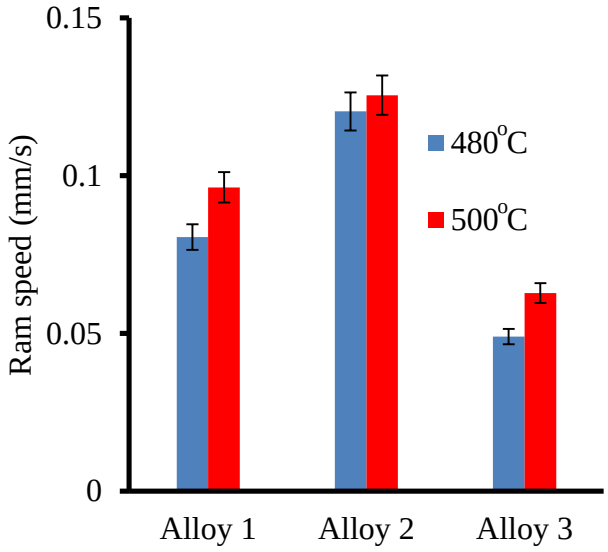

Figure 5.23: Effect of extrusion temperature on ram speed

As seen in Figure 5.23, the ram speed was observed to increase with an increase in extrusion temperature for alloys 1, 2 and 3. Figure 5.23 shows that the extrudability (i.e. ease of extrusion) of these alloys increase with an increase in the extrusion temperature. As the extrusion temperature increases, the billet becomes softer and therefore relatively easier to deform.

5.3 Surface to surface microstructure

The influence of alloy composition and extrusion ratio on the microstructures of the laboratory and industrial extrusion alloys are discussed in this section. The laboratory scale extrusion was performed at an extrusion ratio E_R = 44 into a simple strip geometry which translates into a true strain of 3.8 whereas the industry scale extrusion was performed using a porthole die geometry to make a complicated shape at an E_R = 40 (translates into a true strain of ~ 3.7). For the laboratory extruded profiles, samples for microstructural examination were extracted at 508 mm from the end and 8 mm from the mid-length of the extruded profile. The sample for optical examination was extracted 9 mm from the centre of the outer web and 505 mm from the end of the industrial extrusion front rail profile.

5.3.1: Laboratory extruded profile (E_R = 44)

The low magnification (×50) microstructure of the anodized surface to surface microstructure of the laboratory extruded alloy 1 is shown in Figure 5.24. Also, high magnification (×200) examination of locations in the centre and surface regions was performed in order to adequately characterize the microstructure at these locations. The extrusion direction is parallel to the surface of the page.

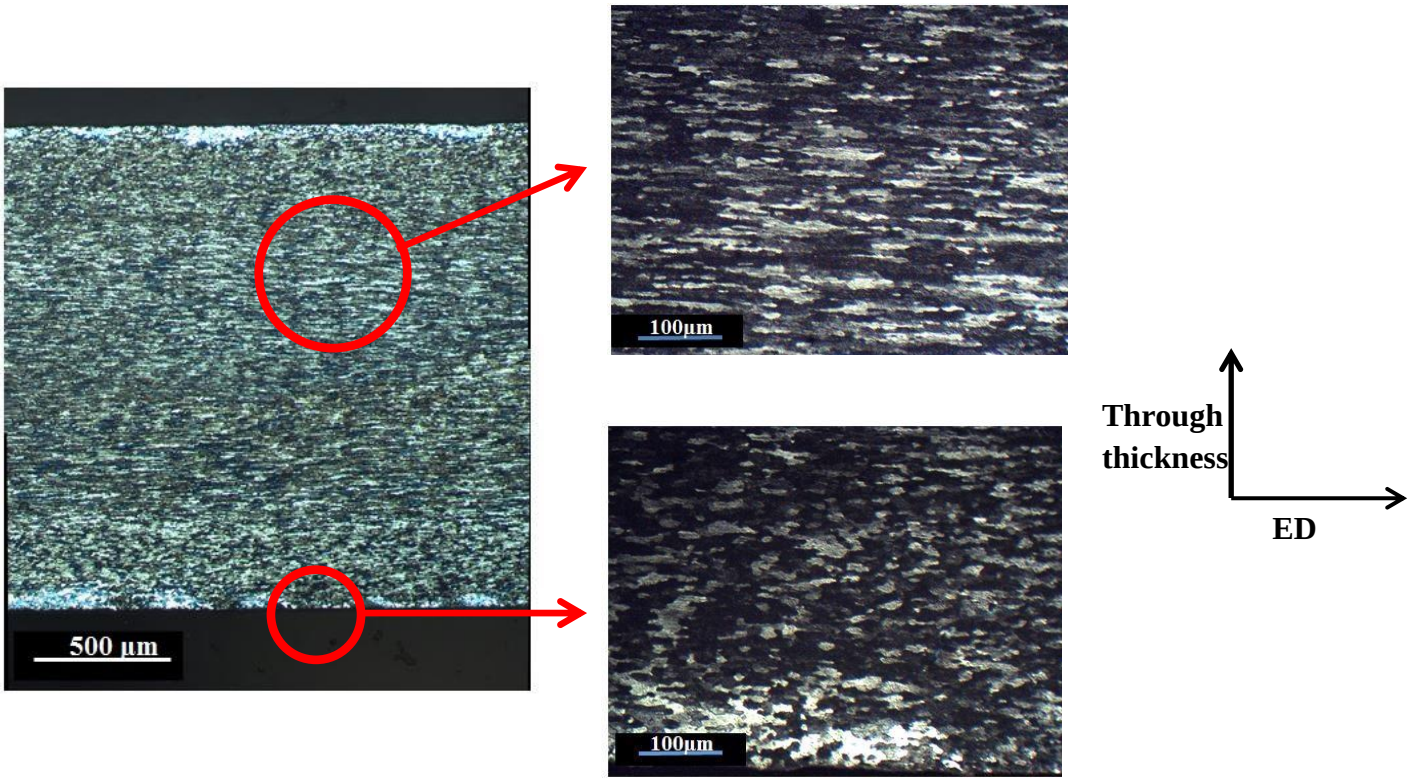

Figure 5.24: Surface to surface microstructure of alloy 1 (Extrusion temperature = 500 ^{o}C)

As shown in Figure 5.24, the low magnification microstructure of the laboratory extruded alloy 1 was observed to exhibit a fine recrystallized grain structure in the surface region as well as in the layers just below the surface. The surface layer was observed to be filled with recrystallized grains as peripheral coarse grains (PCG) were not observed in the surface layer of this alloy after extrusion. As seen in the high magnification examination of the alloy's centre region, the core of the alloy was observed to contain recrystallized grains after the laboratory scale extrusion. The low and high magnification microstructures of the laboratory extruded alloy 2 are shown in Figure 5.25.

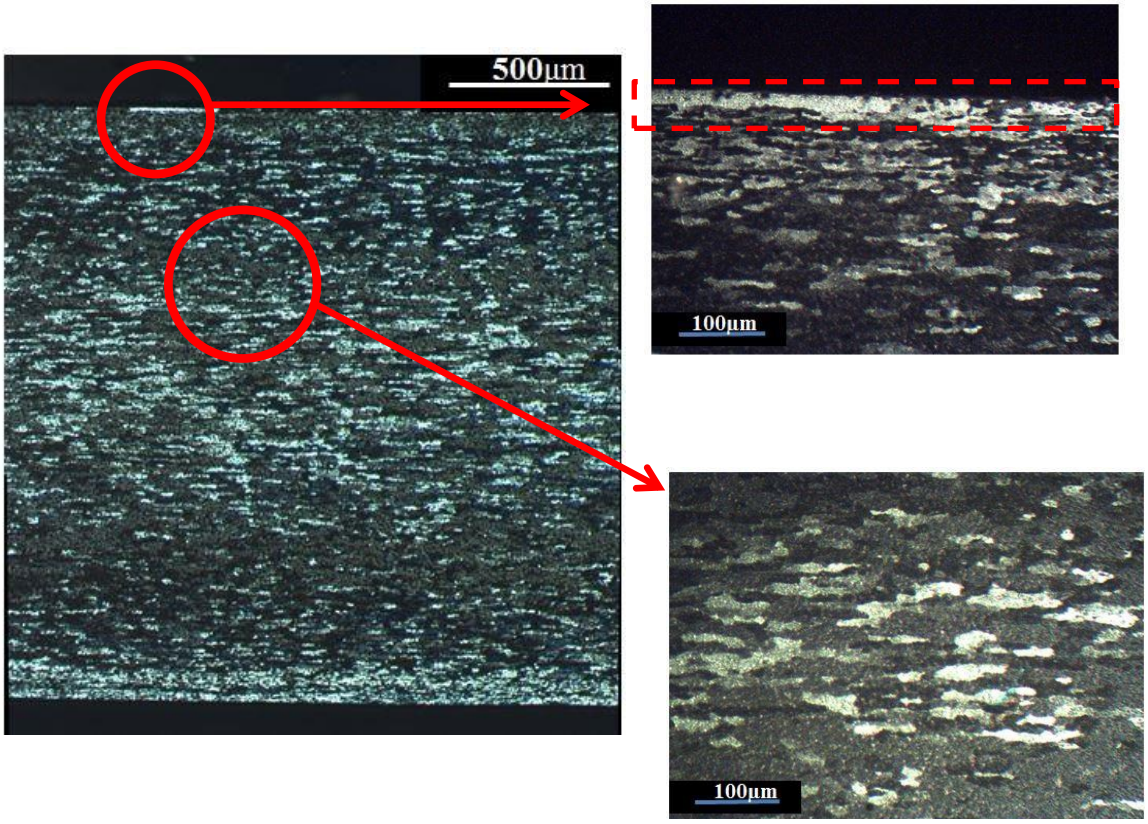

Figure 5.25: Surface to surface microstructure of alloy 2 (500 ^{o}C)

The surface layer of alloy 2 was observed to contain more coarse grains in comparison to the grains observed in the surface layer of alloy 1. In the high magnification image of the extruded profile, a coarse grain layer (shown in broken red line) with depth of approximately 20 µm was observed in the surface region of the laboratory extruded alloy 2. High magnification examination of the centre region reveals a recrystallised grain structure in the core of the alloy after extrusion. The microstructure of alloy 3 after extrusion at an extrusion ratio E_R = 44 is shown in Figure 5.26.

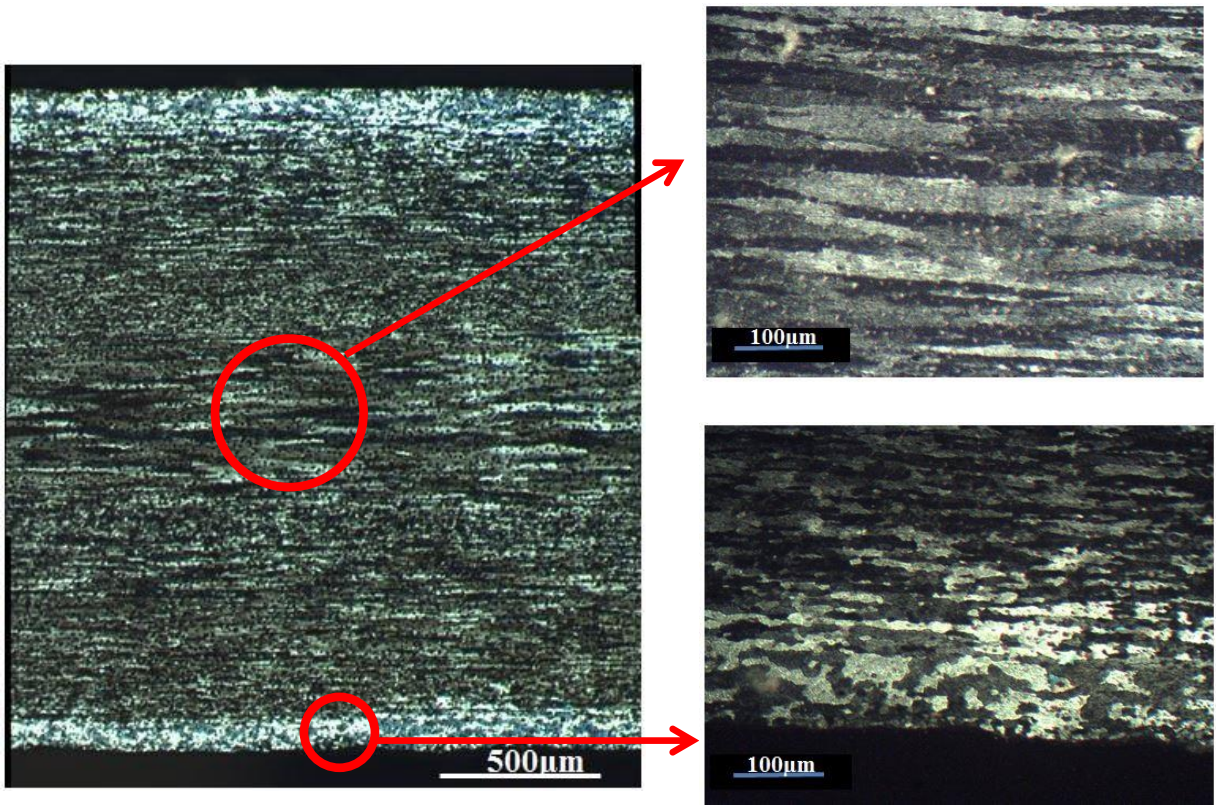

Figure 5.26: Surface to surface microstructure of alloy 3 (500 ^{o}C)

The microstructure of alloy 3 extruded in the laboratory scale extrusion equipment (Figure 5.26) reveals small recrystallized grains in the surface layer. The recrystallized grain structure in the surface region was observed to be similar to that present in the surface region of alloy 1 after extrusion at E_R = 44. High magnification examination of the region below the recrystallized surface layer reveals a fibrous grain structure followed by the presence of large deformed grains in the centre region. Figure 5.26 shows that coarse recrystallized grains were not observed in the centre and surface regions of this alloy after extrusion. The surface to surface microstructure of alloy 4 after laboratory extrusion is shown in Figure 5.27.

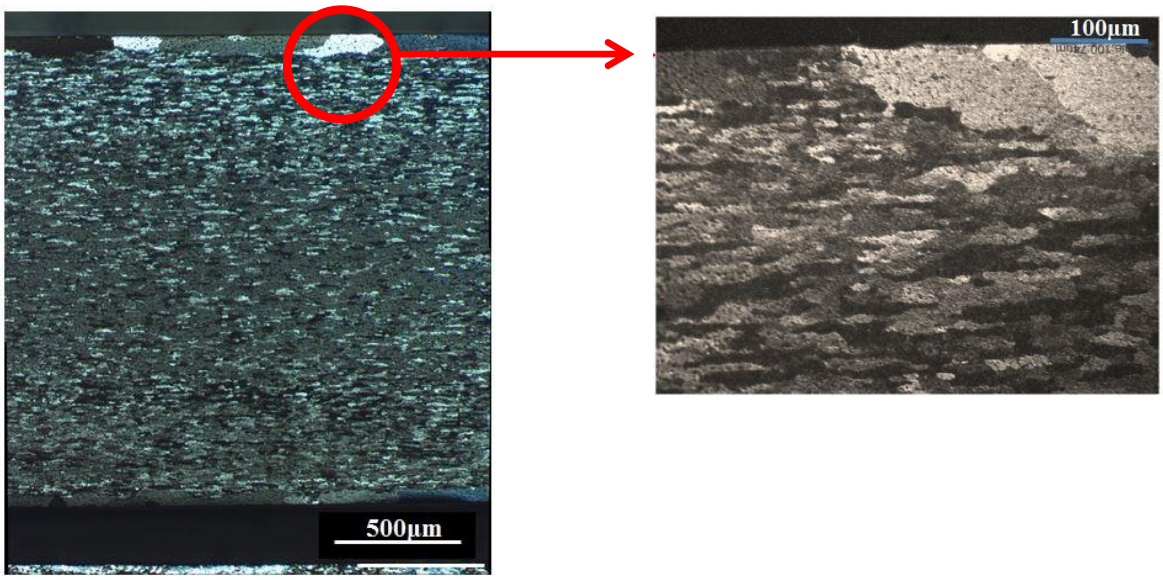

Figure 5.27: Surface to surface microstructure of alloy 4 (500 ^{o}C)

The microstructure of alloy 4 after the laboratory scale extrusion process reveals peripheral coarse grains (PCG) in the surface region and recrystallized grains in the layer below the surface. The coarse grains in the surface region were observed to have an average grain thickness of 70 µm. As seen in Figures 5.24 - 5.27, only fine recrystallized grains were observed in the surface layers of alloys 1 and 3 while alloy 2 extruded on the laboratory scale extruder exhibited a more coarse recrystallized grain strucutre in the surface region. As shown in Table 4.1, there exists only a very small amount of Mn in alloy 4 (0.029 wt. %). Transition elements such as Mn and Cr are known to form dispersoids that pin grain boundaries and retard or prevent occurrence of recrystallization in AA6xxx alloys by Zener pinning of low and high angle grain boundary motion [38, 52, 133]. The higher volume of dispersoids in alloys 1 and 3 (0.1 wt % Mn, 0.2 wt % Cr) in comparison with alloy 2 (0.1 wt % Mn) ensures increased grain boundary pinning and retardation of the recrystallization process in alloys 1 and 3 in comparison with alloy 2. The absence of Mn and Cr containing dispersoids in alloy 4 therefore ensures increased mobility for

boundary migration and grain growth. This is believed to be responsible for the presence of peripheral coarse grains in the surface layer of alloy 4 after extrusion.

A summary of the centre to surface microstructures of the laboratory extruded alloys are shown in Table 5.5.

Table 5.5: Centre to surface microstructure characterization of laboratory extruded alloys

	Alloy			
	1	**2**	**3**	**4**
Surface	Recrystallized grains	Coarse recrystallized grains present	Small recrystallized grains	Peripheral coarse grains present
Centre	Recrystallized grains	Recrystallized grains	Large deformed grains and fibrous grains	Recrystallized grains

The surface of the alloys were observed to exhibit either a recrystallized grain structure (alloys 1 and 3) filled with small fine grains, a somewhat thick layer of coarse grains (alloys 2) or peripheral coarse grains (alloy 4). At the start of the extrusion process, the material to be extruded experiences an increase in temperature as it passes through the die due to friction effect between the die and the surface of the material to be extruded. The surface therefore experiences higher temperature and strain rate deformation in comparison with the centre. The increased deformation at the surface ensures an increase in the stored energy – the required driving force for recrystallization. This therefore explains why the surface layer of the four alloys exhibit a more recrystallized structure than the core after the extrusion process.

5.3.2: Industrial extrusions ($E_R = 40$)

The surface to surface microstructure of alloy 1 after extrusion at 500 ^oC and E_R =40 is shown in Figure 5.28.

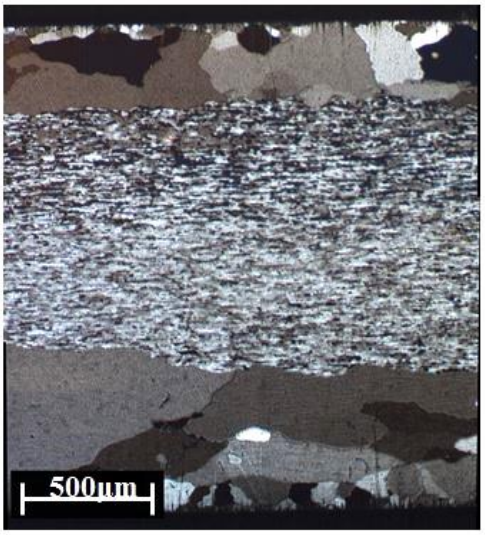

Figure 5.28: Surface to surface microstructure of alloy 1 (500 ^{o}C)

As seen in Figure 5.28, Coarse grains as well as small recrystallized grains were observed in the surface layer of alloy 1 extruded at E_R = 40. The average thickness of the coarse grains present in the surface layer was approximately 400 µm. The layers below the surface of the industrial extrusion alloy were observed to be filled with fibrous grains.

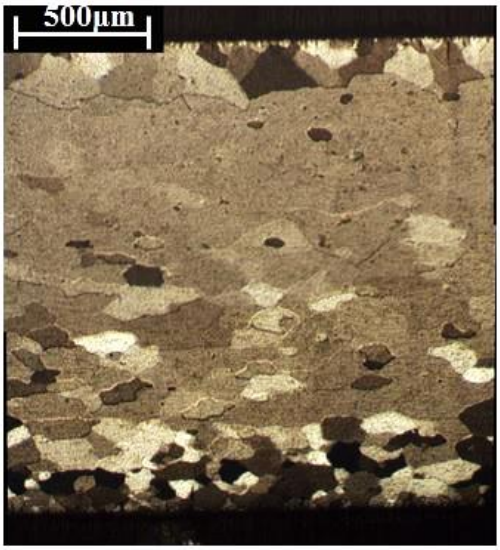

Figure 5.29: Surface to surface microstructure of alloy 2 (500 ^{o}C)

The surface to surface microstructure of alloy 2 extruded in the industrial extrusion machine is shown in Figure 5.29. One surface layer was observed to contain fine recrystallized grains while

the other surfac exhibits coarse grains with average diameter of 200 µm. The section below the coarse grain region was observed to exhibit an unrecrecystallized structure.

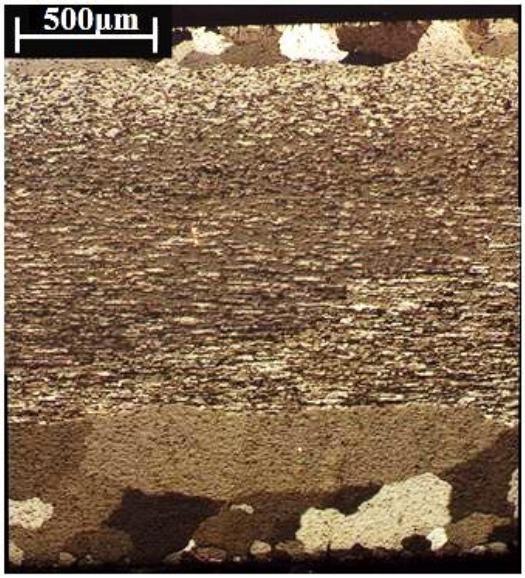

Figure 5.30: Surface to surface microstructure of alloy 3 (500 ^{o}C)

The surface to surface microstructure of alloy 3 after the industrial extrusion process (shown in Figure 5.30) reveals coarse grains and few fine granular grains in the surface layer. The average coarse grain diameter was aproximately 185 µm. The centre of the extrudate was observed to exhibit a fibrous grain structure.

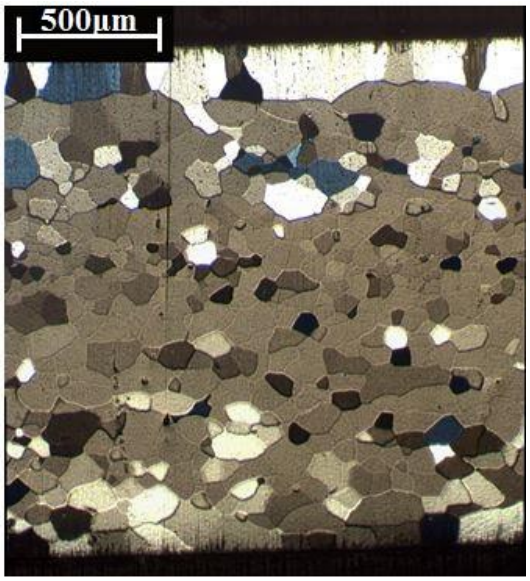

Figure 5.31: Surface to surface microstructure of alloy 4 (500 ^{o}C)

Figure 5.31 shows the surface to surface microstructure of alloy 4 after the industrial scale extrusion process. Alloy 4 exhibits a fully recrystallized grain structure in the centre region with smaller grains present in the core and large grains in the layers just below the surface. The microstructure of the alloy reveals the presence of coarse grains with average grain thickness of 200 μm in one of the alloy's surface layer. Small recrystallized grains were observed to be present in the centre region of the alloy while larger recrystallized grains were confirmed in the layer just below the coarse grain layer.

The surface to surface microstructures of the alloys studied (see Figs. 5.24 - 5.31) reveals the presence of large recrystallized grains in the surface layer of the industrial extruded profiles - presence of peripheral coarse grains (PCG). During the industrial extrusion process, the alloys were extruded at a faster rate than in the laboratory scale extrusion process. This implies that the profiles were subjected to higher strain rate deformation during the industrial extrusion process. The large strain rate deformation resulting from increased extrusion speed during the industrial extrusion process causes the grains within the alloy microstructure to have sufficient stored energy required to trigger recrystallization.

5.4 Post extrusion properties

5.4.1 Laboratory extruded materials

Hardness

The measured hardness of alloys 1, 2 and 3 as a function of extrusion temperature in the T4 (as-extruded), T5 (aged at 185 ^{o}C for 5 hours without solutionizing) and T6 (solutionized at 540 ^{o}C for 40 mins. followed by aging at 185 ^{o}C for 5 hours) tempers is shown in Figure 5.32. The hardness value presented is an average of three repetitions for each condition. Also, the hardness samples were selected in close proximity of each other in order to ensure similar grain structure.

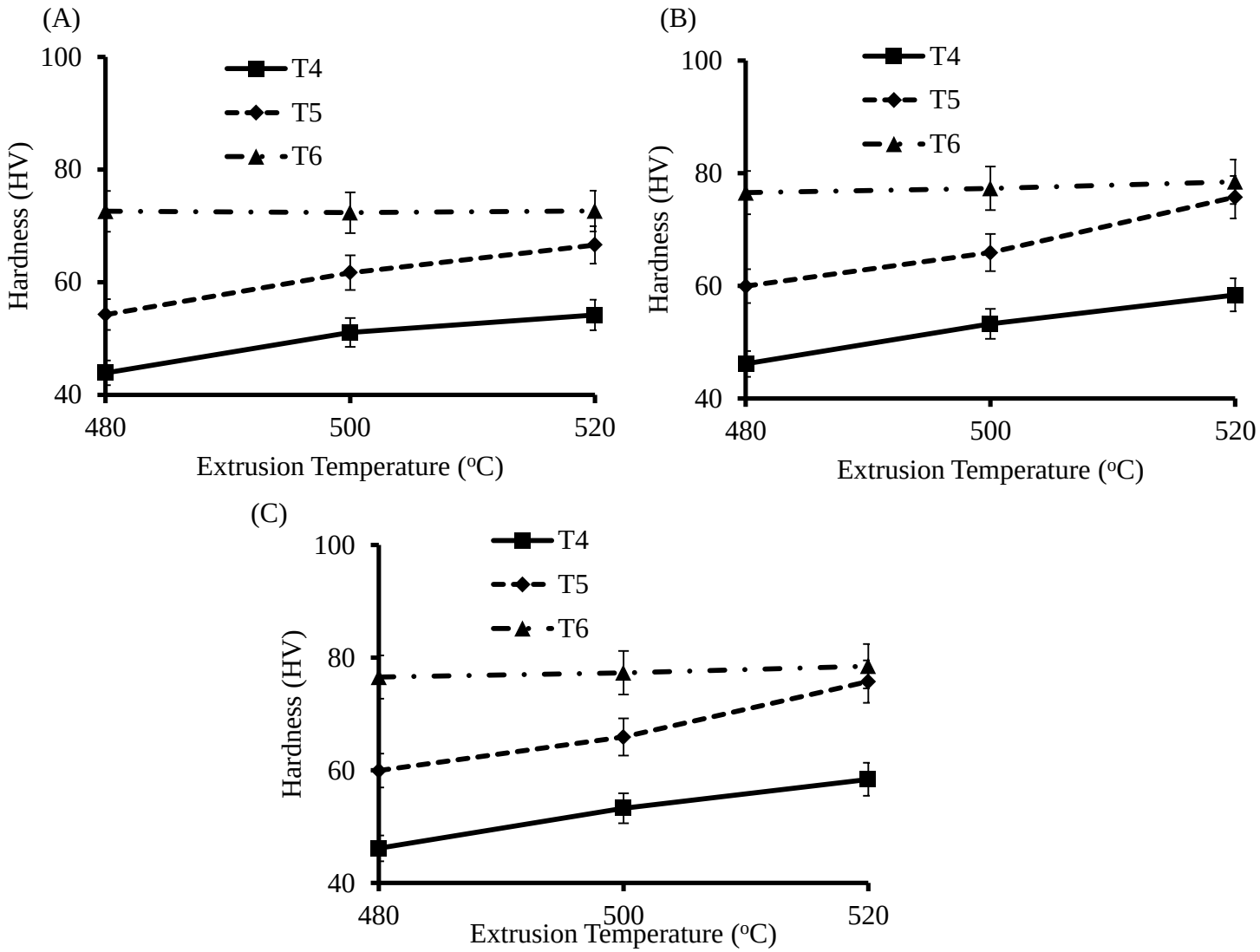

Figure 5.32: Average Vickers hardness measurement for different extrusion temperatures (A): Alloy 1, (B): Alloy 2, (C): Alloy 3

In all three alloys studied, the average measured Vickers hardness value of the T4 and T5 samples were observed to increase with extrusion temperature. In the T4 condition, an increase in the hardness with increasing extrusion temperature is believed to be due to an increase in the Mg and Si dissolved in solid solution which results in an increase in the alloy's deformation resistance. The extruded profiles of alloys 1, 2 and 3 were observed to possess higher measured hardness value in the T5 condition than in the T4 as-extruded form. This increase is believed to be due to the precipitation of Mg_2Si phases during aging to the T5 condition. Mg_2Si phases are

primary strengthening phases in Al-Mg-Si alloys and have been reported to serve as obstacles to dislocation movement [88]. As expected, in the T6 condition, the measured hardness values for each of the alloys were observed to be independent of extrusion temperature. This trend is expected as solutionizing at 540 ^{o}C for 40 min prior to aging ensures complete dissolution of the Mg-Si into the alloy matrix. Therefore, upon subsequent aging at 185 ^{o}C for 5 h; optimum precipitation of Mg_2Si phases which are the primary strengthening phases in Al-Mg-Si alloys is achieved irrespective of prior extrusion temperature. In the T4, T5 and T6 conditions, alloys 1(0.5 Mg, 0.5 Si, 0.2 Cr) and 3 (0.9 Mg, 0.6 Si, 0.2 Cr) were observed to possess the lowest and highest hardness values respectively for all extrusion temperatures. This implies that the hardness property increases with increase in the Mg-Si content while 0.2 wt % Cr addition contributes only marginally to the hardness property considering the small difference in hardness property of alloys 2 and 3 in the T4, T5 and T6 conditions.

Effect of extrusion temperature, alloy composition and aging time on tensile properties

The engineering stress-strain curves obtained during the tensile testing of alloy 1 extruded at 480, 500 and 520 ^{o}C are shown in Figure 5.33.

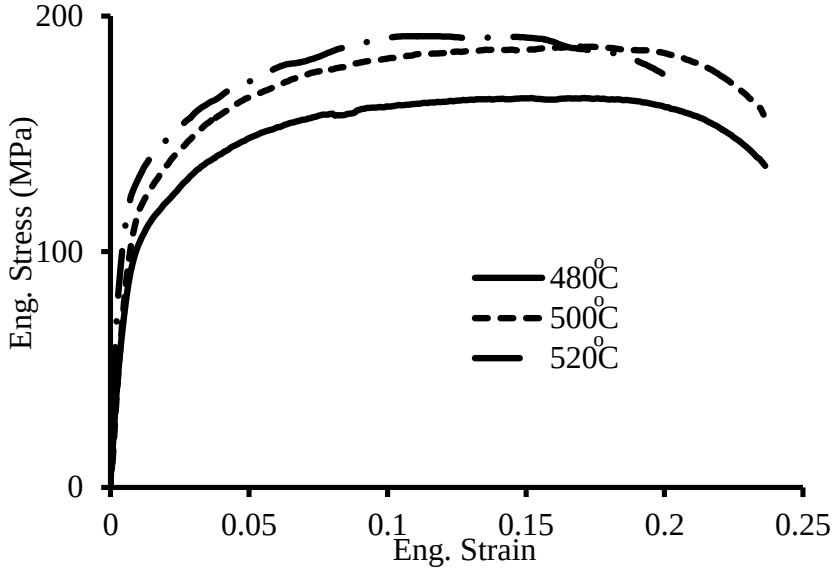

Figure 5.33: Stress-strain curve for alloy 1 extruded at different temperatures (T4)

As seen in Figure 5.33, the extrusion temperature was observed to influence the tensile properties of alloy 1 in the T4 condition. The stress-strain curves of alloys 1, 2 and 3 extruded at 500 ^{o}C are shown in Figure 5.34.

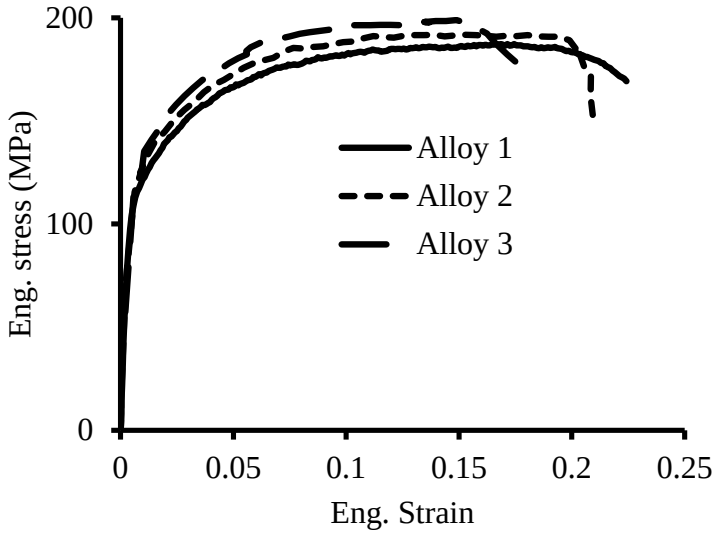

Figure 5.34: Stress-strain curves for alloys 1, 2 and 3 after extrusion at 500 ^{o}C (T4)

The tensile properties of alloy 1 in the T4 condition after extrusion at different temperatures are shown in Figure 5.35. The yield and ultimate tensile strengths were observed to increase with temperature.

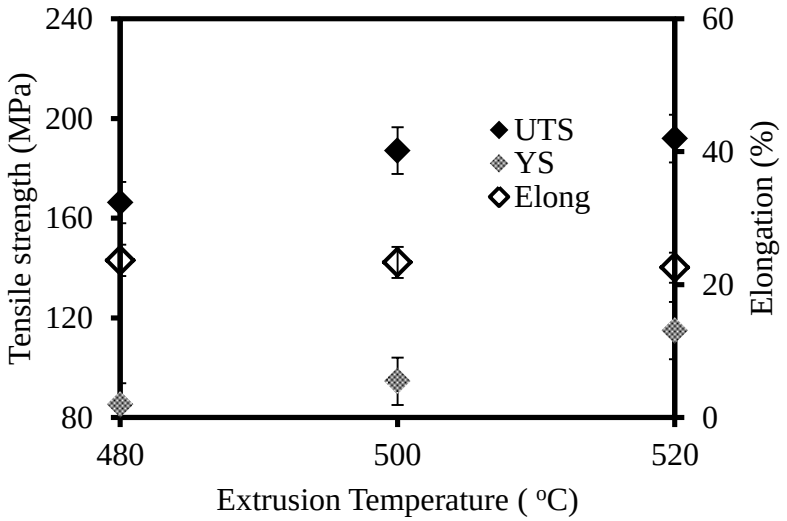

Figure 5.35: Tensile properties of alloy 1 (T4) as a function of extrusion temperature

The UTS of alloy 1 increased from 166 MPa to 192 MPa with increase in the extrusion temperature from 480 ^{o}C to 520 ^{o}C while the ductility was observed to decrease with increase in extrusion temperature. The increase in tensile strength of alloy 1 with an increase in the extrusion temperature is believed to be due to an increase in the Mg-Si dissolved in solution which is responsible for an increase in the alloy's deformation resistance [6, 79]. The solid fraction diagram of alloy 1 showing the dissolution of present phases as a function of temperature is shown in Figure 5.36.

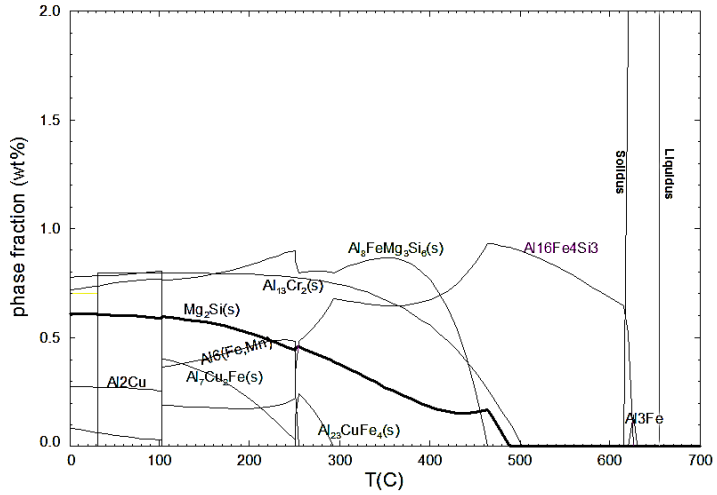

Figure 5.36: Solid fraction diagram of alloy 1 showing the dissolution of present phases [134]

As seen in Figure 5.36, complete dissolution of Mg_2Si phases is expected at about 495 ^{o}C. This therefore explains the increase in the UTS of alloy 1 (from 166 to 192 MPa – a 16 % increase in strength) when the extrusion temperature is increased from 480 ^{o}C to 520 ^{o}C. However with complete dissolution of Mg-Si phases just below 500 ^{o}C, only a slight increase in strength is expected for alloy 1 samples extruded above 500 ^{o}C. As seen in Figure 5.35, the average UTS of alloy 1 samples extruded at 520 ^{o}C was 192 MPa – a 2 % increase in strength over samples extruded at 500 ^{o}C. The tensile properties of alloys 2 and 3 in the T4 condition as a function of extrusion temperature are shown in Figures 5.37(A) and (B) respectively.

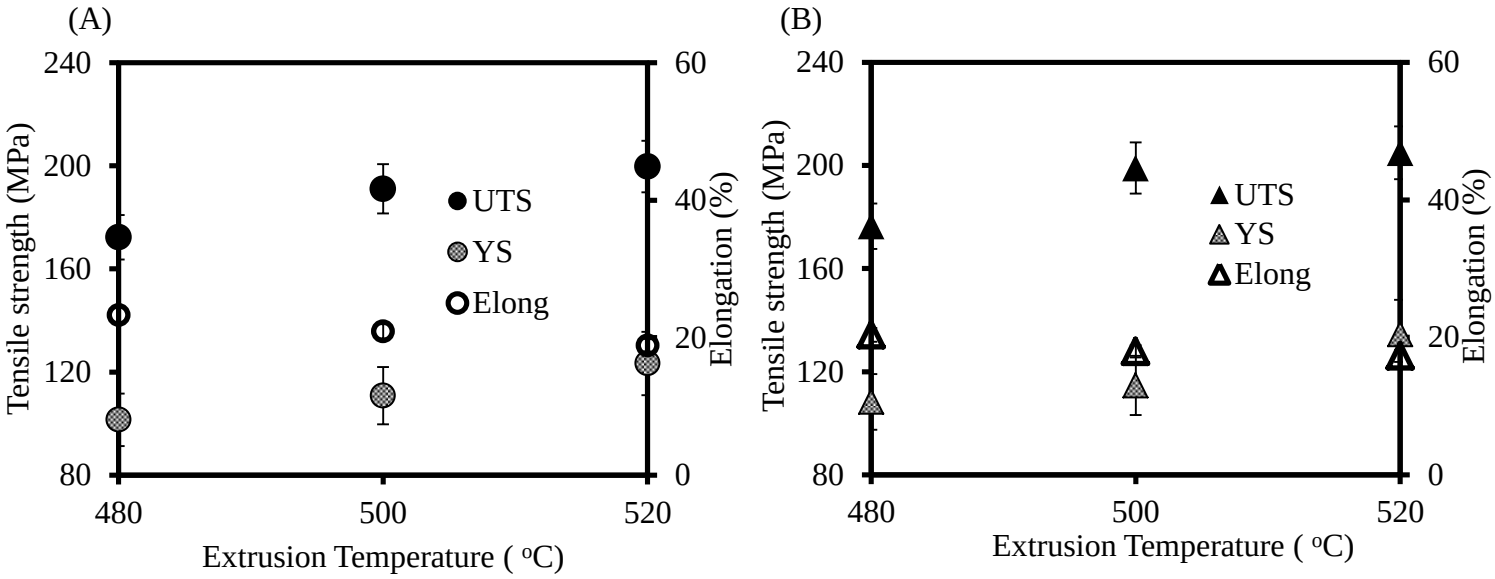

Figure 5.37: Tensile properties as a function of extrusion temperature (T4) (A): alloy 2, (B): alloy 3

The UTS of alloys 2 (from 172 MPa to 200 MPa) and 3 (from 176 MPa to 205 MPa) were observed to increase with an increase in the extrusion temperature from 480 °C to 520 °C. The solid fraction diagrams of alloys 2 and 3 as a function of temperature are shown in Figure 5.38 and 5.39 respectively.

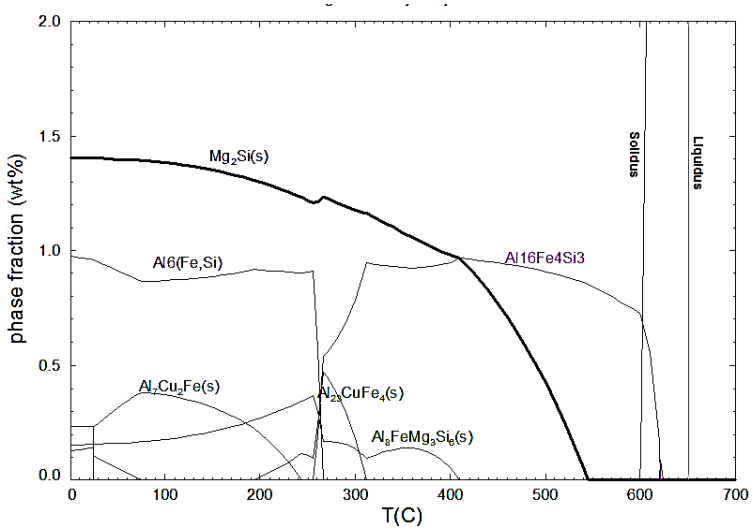

Figure 5.38: Solid fraction diagram of alloy 2 showing dissolution of present phases [134]

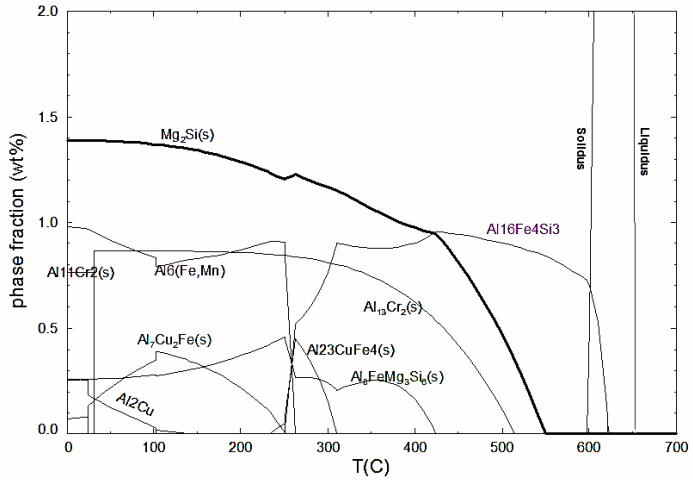

Figure 5.39: Solid fraction diagram of alloy 3 showing dissolution of present phases [134]

The solid fraction diagrams of alloys 2 and 3 shown in Figure 5.38 and 5.39 respectively indicate that complete dissolution of Mg_2Si phases occur at ~ 550 ^oC. This is believed to explain the increase in tensile strength of both alloys with increasing extrusion temperature. A 5 % and 3 % increase in UTS were observed for alloys 2 and 3 respectively when the extrusion temperature is increased from 500 ^oC to 520 ^oC even though complete dissolution of Mg_2Si phases is expected at approximately 550 ^oC. Also as seen in Figure 5.39, Cr containing $Al_{13}Cr_2$ (s) phases are expected to be present in alloy 3 up to ~ 500 ^oC. The slightly higher strength of alloy 3 in comparison to alloy 2 may be due to the role of these Cr containing particles which serve as obstacles to dislocation movement. Lee et al. [135] also reported that Mn containing particles contribute to an increase in strength of Al-Mg-Si alloys by restricting dislocation motion. Figures 5.35 and 5.37 show that alloy 3 (0.9 Mg, 0.6 Si 0.2 Cr) possess the highest and lowest UTS and ductility respectively for all extrusion temperatures. The higher strength of alloys 2 and 3 in comparison to alloy 1 is believed to be due to the higher Mg-Si dissolved in solution. This indicates that an increase in the Mg-Si content results in an increase in the tensile strength of the Al-Mg-Si alloys. Also, an increase in the Mg-Si content was observed to result into lower ductility for all test extrusion temperature. For example, ductility was observed to reduce from

24 % in alloy 1 to 18 % in alloy 3 after extrusion at 500 °C. However, there exists no obvious effect of 0.2 wt % Cr addition on ductility in the T4 condition as alloys 2 and 3 exhibit nearly equivalent ductility after extrusion at 480, 500 and 520 °C.

The tensile properties of alloys 1 and 2 extruded at 500 °C and artificially aged without solutionizing i.e. T5 condition are shown in Figure 5.40.

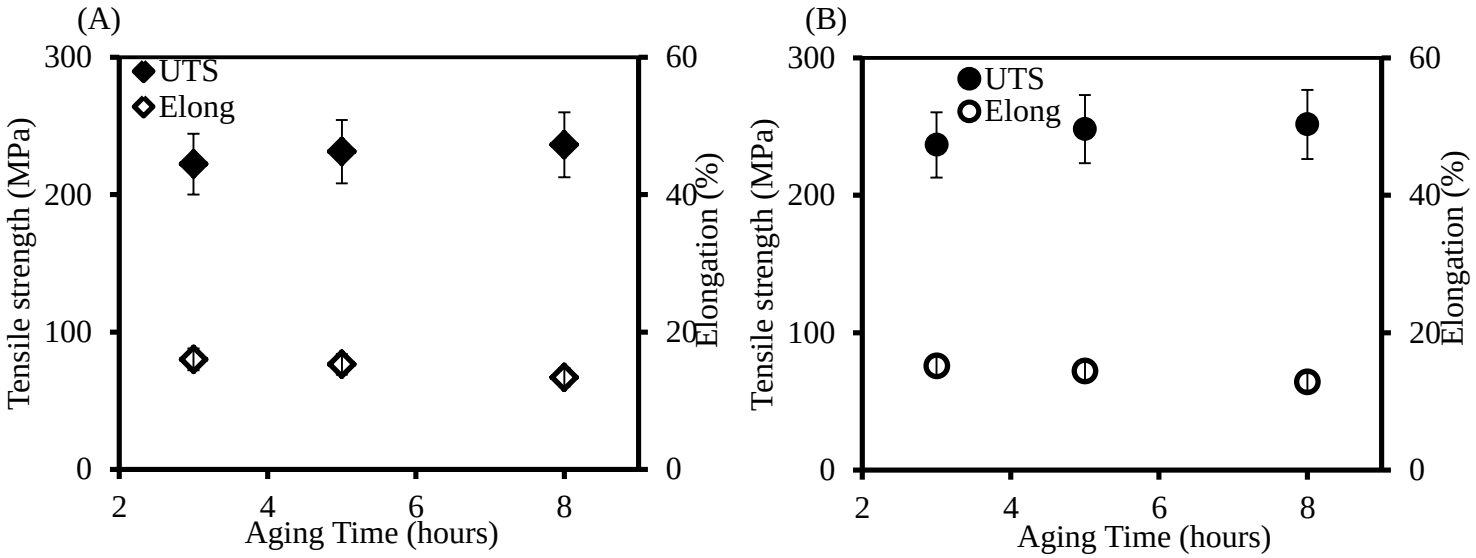

Figure 5.40: Tensile properties as a function of aging time after extrusion at 500 °C (T5) (A): alloy 1, (B): alloy 2

After aging for 3, 5 and 8 hours, alloy 1 was observed to exhibit lower UTS and higher ductility in comparison with alloy 2.

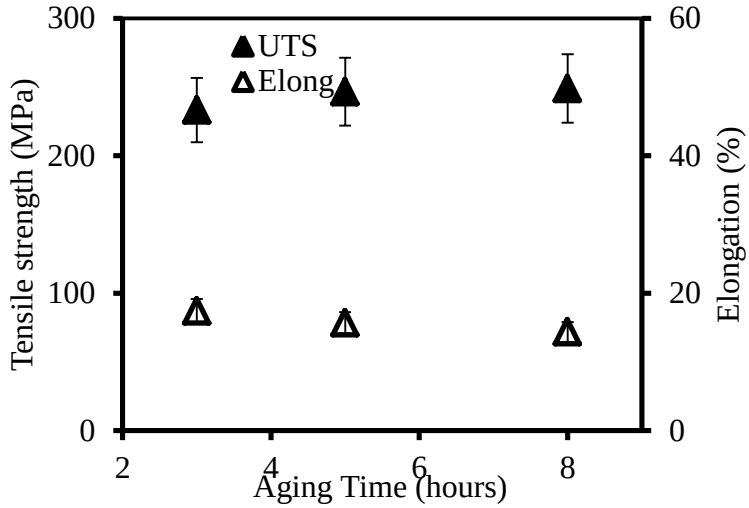

Figure 5.41: Tensile properties of alloy 3 (T5) as a function of aging time (extrusion at 500 °C)

Figure 5.41 shows the tensile property evolution of alloy 3 after aging to T5 condition. As seen in Figures 5.40 and 5.41, alloys 2 and 3 exhibited equivalent tensile strength. In the T5 condition, the UTS for all three alloys was observed to increase with an increase in the aging time. This indicates that 0.2 wt % Cr addition has only negligible effect on the strength of the Al-Mg-Si alloys after aging to the T5 condition.

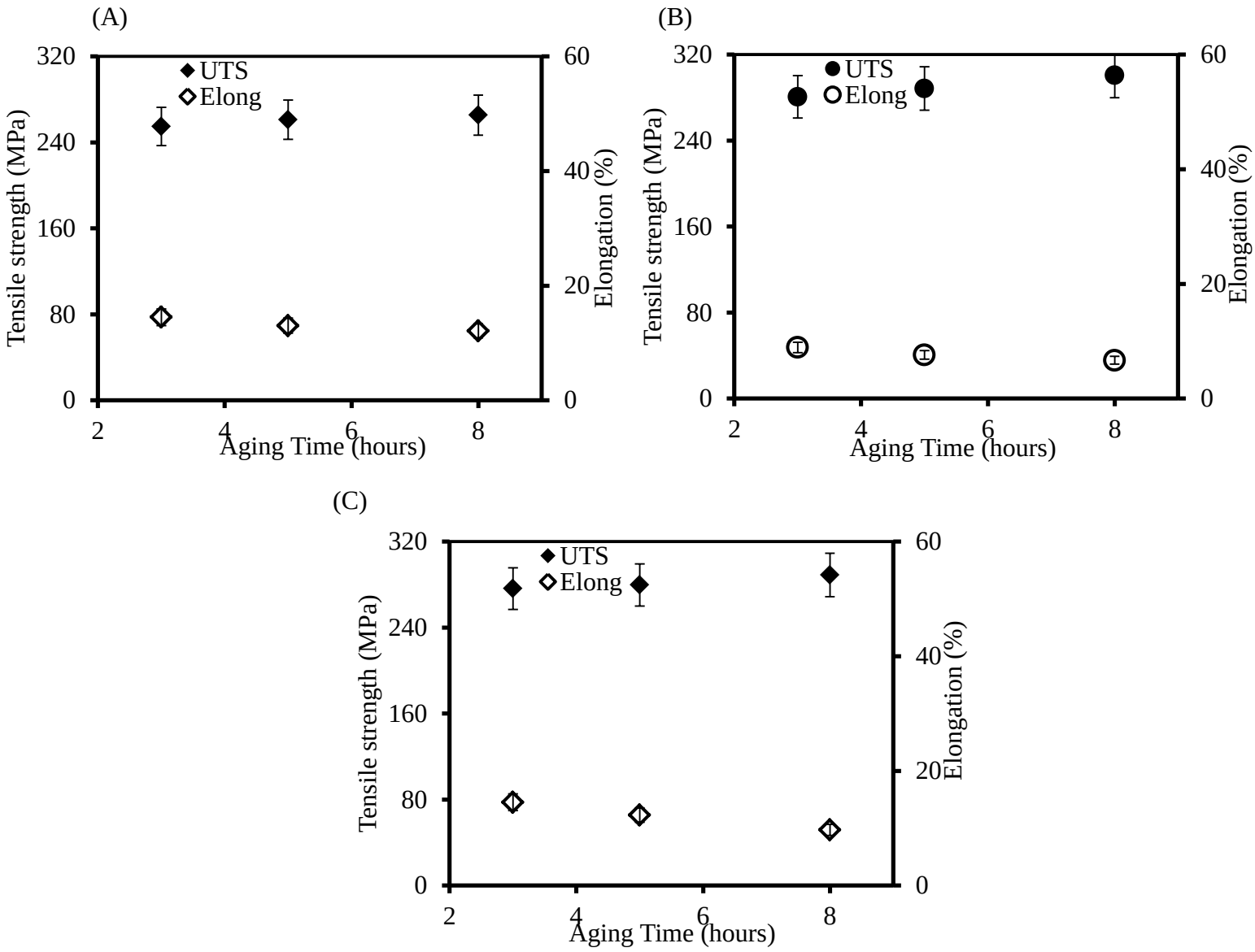

Figure 5.42: Tensile properties (T6) as a function of aging time after extrusion at 500 ^{o}C (A): Alloy 1, (B): Alloy 2, (C): Alloy 3

The increase in strength with aging time in the T5 condition is believed to be due to the precipitation of Mg_2Si phases that serve as obstacles to dislocation motion. The ductility of the alloys was observed to decrease with an increase in the aging time. After aging to the T5 condition; alloy 3 was observed to exhibit slightly higher ductility than alloy 2. The ductility of alloys 1 and 3 were observed to be equivalent for all aging conditions in the T5 temper. The tensile property evolution of alloys 1, 2 and 3 in the T6 condition are shown in Figure 5.42. The UTS of alloys 1, 2 and 3 was observed to increase with aging time in the T6 condition. Also the alloys were observed to exhibit greater strength in the T6 condition in comparison with strength properties in the T5 condition. Alloy 1 was observed to exhibit a lower ductility in the T6 condition in comparison with the T5 condition. The complete dissolution of Mg-Si phases during the solutionizing process at 540 ^oC ensures that more Mg_2Si precipitates are formed in the T6 samples in comparison with the T5 samples. For all aging times, alloy 2 was observed to exhibit slightly higher tensile strength than alloy 3. However, alloy 3 exhibited a higher ductility in comparison with alloy 2. Alloy 1 was observed to exhibit a slightly higher ductility than alloy 3. This indicates that an increase in the Mg-Si content results into a slight decrease in ductility of the Al-Mg-Si alloys in the T6 condition.

Fracture Morphology of laboratory scale extrusions

The secondary electron microscope (SEM) images of the fracture surface for alloys 1, and 3 extruded at 500^oC in the laboratory scale extruder then aged at 185 ^oC for 5 hours without solutionizing i.e. T5 condition are shown in Figure 5.43.

(A) (B)

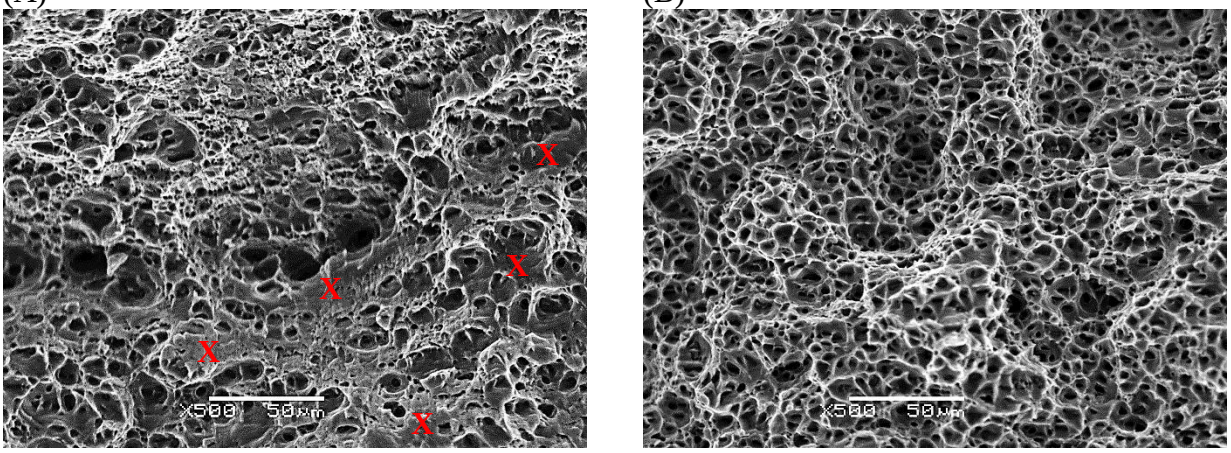

Figure 5.43: Fracture morphology of samples extruded at 500°C and aged for 5 hours (T5) (A): Alloy 1, (B): Alloy 3

The fracture surface of alloy 1 (Figure 5.43A) exhibits mixed fracture mode with ductile dimple fracture in the centre region and sheared fracture morphology (labeled X in image) towards the edge of the specimen. The dimple structure of the fracture surface is known to form by nucleation, growth and coalescence of micro-voids formed due to large plastic deformation in the process zone [136]. The fracture surface of alloy 3 (shown in Figure 5.43B) is observed to exhibit a ductile fracture mode devoid of sheared fracture morphology. The fracture surface was observed to be filled with smooth well-arranged uniform sized dimples.

(A) (B)

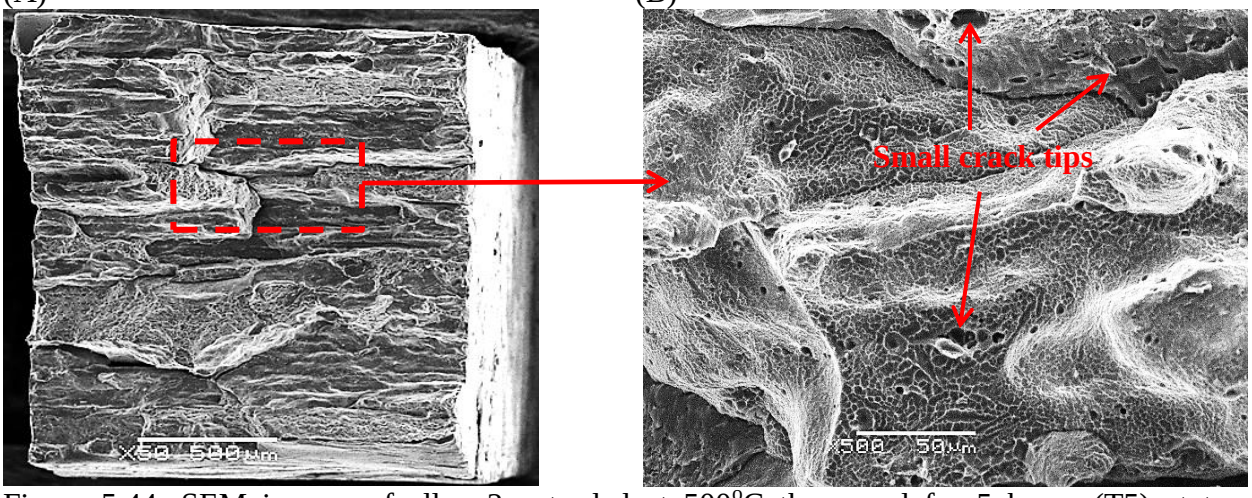

Figure 5.44: SEM images of alloy 2 extruded at 500°C then aged for 5 hours (T5) at two magnifications

The fracture morphology of alloy 2 extruded at 500 ^{o}C and heat treated to T5 condition is shown in Figure 5.44. As seen in the low magnification image shown in Figure 5.44A, alloy 2 exhibits intergranular fracture morphology. At higher magnification (Figure 5.44B), small size dimple structures were observed on the surface of the extruded profile. The presence of small crack tips indicates the attainment of a critical local strain required for intergranular crack nucleation. Intergranular fracture is known to occur due to impingement of grain boundaries by slip bands resulting into increased local strain concentrations that nucleate voids at coarse particles [101]. Alloys 1 and 3 were observed to exhibit no intergranular fracture morphology after aging for 5 hours. This could be due to the presence of Cr containing dispersoids present in these alloys. Unlike the Mg_2Si precipitation hardening phases, dispersoids are not sheared by dislocations [100]. The accumulation of dislocations at dispersoids cause slip to be transferred to adjacent planes and hence slip homogenization results [136]. This prevents attainment of critical local strain required for intergranular crack nucleation [39]. This therefore explains the lower ductility of alloy 2 in comparison to that exhibited by alloys 1 and 3 after aging at 185^{o}C for 5hours. The fracture morphologies of alloys 1 and 3 extruded at 500 ^{o}C and aged to T6 condition after 5 hours are shown in Figure 5.45.

(A) (B)

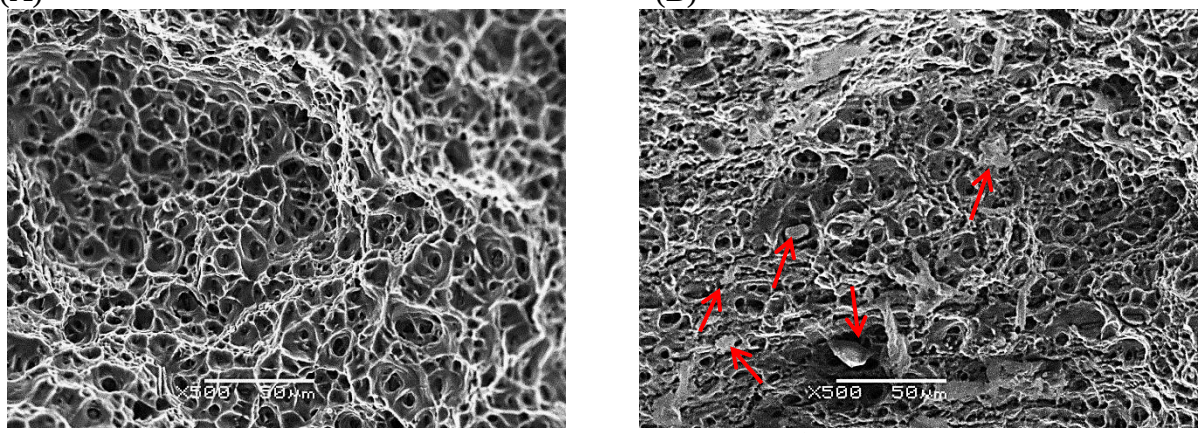

Figure 5.45: Fracture morphology of samples extruded at 500^{o}C (T6) (A): Alloy 1, (B): Alloy 3

As seen in Figure 5.45, alloys 1 and 3 were observed to exhibit ductile dimple fracture morphology after aging for 5 hours to T6 condition. Alloy 1 fracture surface was observed to be filled with fairly uniform size dimples. In the fracture surface of alloy 3 shown in Figure 5.45B, the presence of round particles (arrow) were confirmed within some of the dimples. These round particles were however not observed in alloy 3 sample aged to T5 condition. Figure 5.46 shows the fracture surface of alloy 2 extruded at 500 ^{o}C followed by aging for 5 hours to T6 condition.

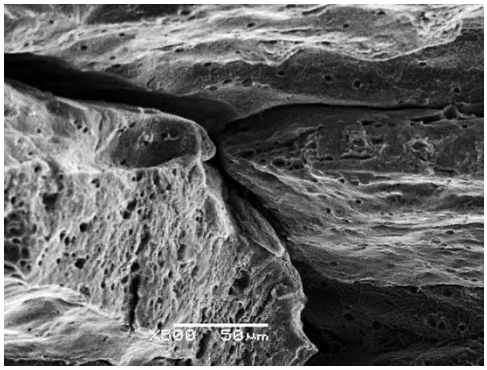

Figure 5.46: High magnification SEM image of alloy 2 (aged for 5 hours to T6)

Figure 5.46 shows that alloy 2 exhibits intergranular fracture morphology after aging to at 185 ^{o}C for 5 hours to T6 condition. The fracture surface is characterized by the presence of small crack tips and crack paths formed by coalescence of small crack tips.

5.4.2 Industrially extruded material

The tensile properties of alloys 1-3 after industrial extrusion and heat treatment to T6 condition (solutionizing at 540 ^{o}C for 90 minutes followed by aging at 171 ^{o}C for 10 hrs.) are presented and discussed in this section. Also, data on the plastic anisotropy and strain rate sensitivity behavior of industrially extruded alloy 4 in the T5 and T6 conditions are presented. The tensile strength and ductility properties of alloys 1-3 are shown in Figure 5.47. The tensile properties presented are an average of three repetitions for each condition. Alloy 1 was observed

to exhibit the lowest strength while alloys 2 and 3 exhibited equivalent strength in the T6 condition.

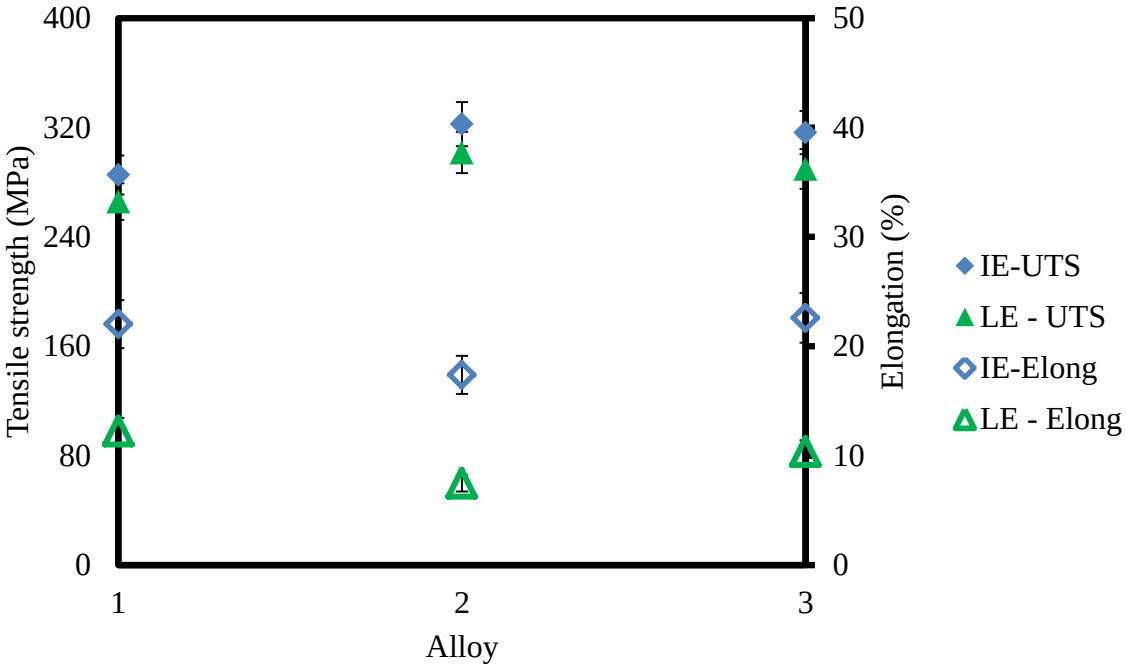

Figure 5.47: Tensile properties of industrial and laboratory extruded alloys 1-3 (after heat treatment to T6 condition)

Alloy 2 was observed to exhibit the lowest ductility while alloys 1 and 3 possess equivalent ductility. The industrial extrusion alloys were observed to exhibit equivalent strength but higher ductility than the laboratory extruded profiles that were aged at 185 ^{o}C for 8 hrs. The higher ductility of the industrial extrusion profiles may be due to a more recrystallized microstructure resulting from the higher stored energy (in comparison with laboratory extrusion) possessed by the profile during the industrial extrusion process. As also observed in the laboratory extruded profiles, the strength and ductility properties of industrial extrusion Al-Mg-Si alloys were observed to increase with increase in Mg-Si content and addition of 0.2 wt % Cr respectively. The microstructure of the industrially extruded alloy 4 in the T4 condition is shown in Figure 5.48.

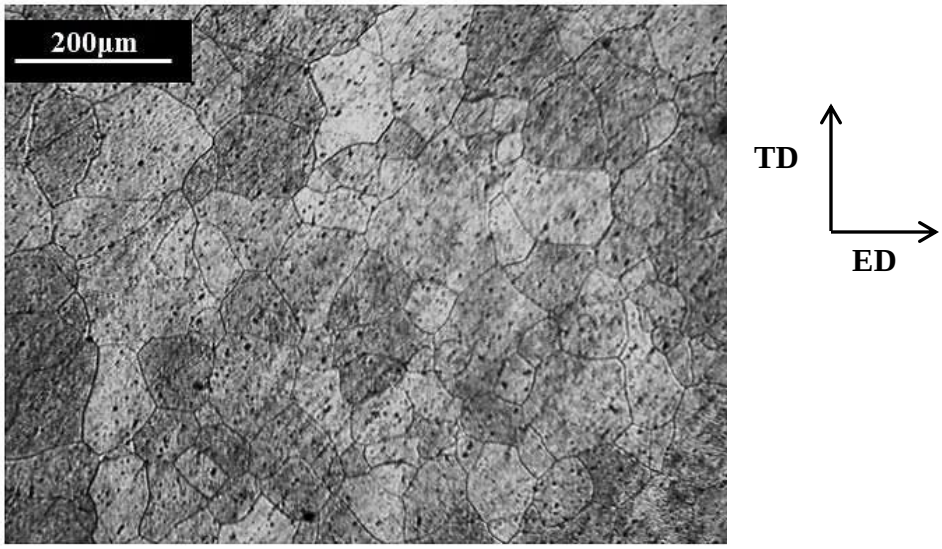

Figure 5.48: Microstructure of alloy 4 after industrial extrusion (T4)

The sample for optical examination was taken from the outer web of the extruded profile. The microstructure of the T4 sample presented in Figure 5.48 reveals a grain structure containing grains whose size are smaller (average grain size of 138 µm) than those found in the homogenized billet shown in Figure 4.3 (D).

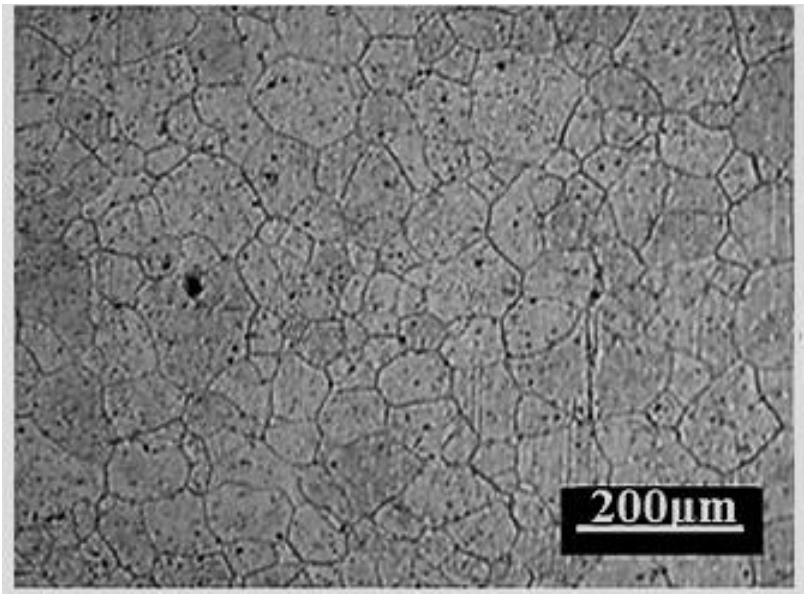

Figure 5.49: Microstructure of alloy 4 after industrial extrusion and heat treatment (T6)

The microstructure of the T6 sample shown in Figure 5.49 reveals the presence of small recrystallized grains.

The true stress vs. effective plastic strain just before necking occurs during uniaxial tensile test at different strain rates for alloy 4 (T6) samples extracted along the extrusion (0^o), 45^o and 90^o directions are shown in Figure 5.50. The average of repeat tests for the true stress vs. effective plastic strain data obtained for the three sample orientations is reported. The effective plastic strain is obtained as:

$$\varepsilon_p = \varepsilon - \frac{\sigma_t}{E} \qquad (5.15)$$

With ε being the true (or logarithmic) strain and σ_t the true (Cauchy) stress while E refers to Young's modulus measured for alloy 4.

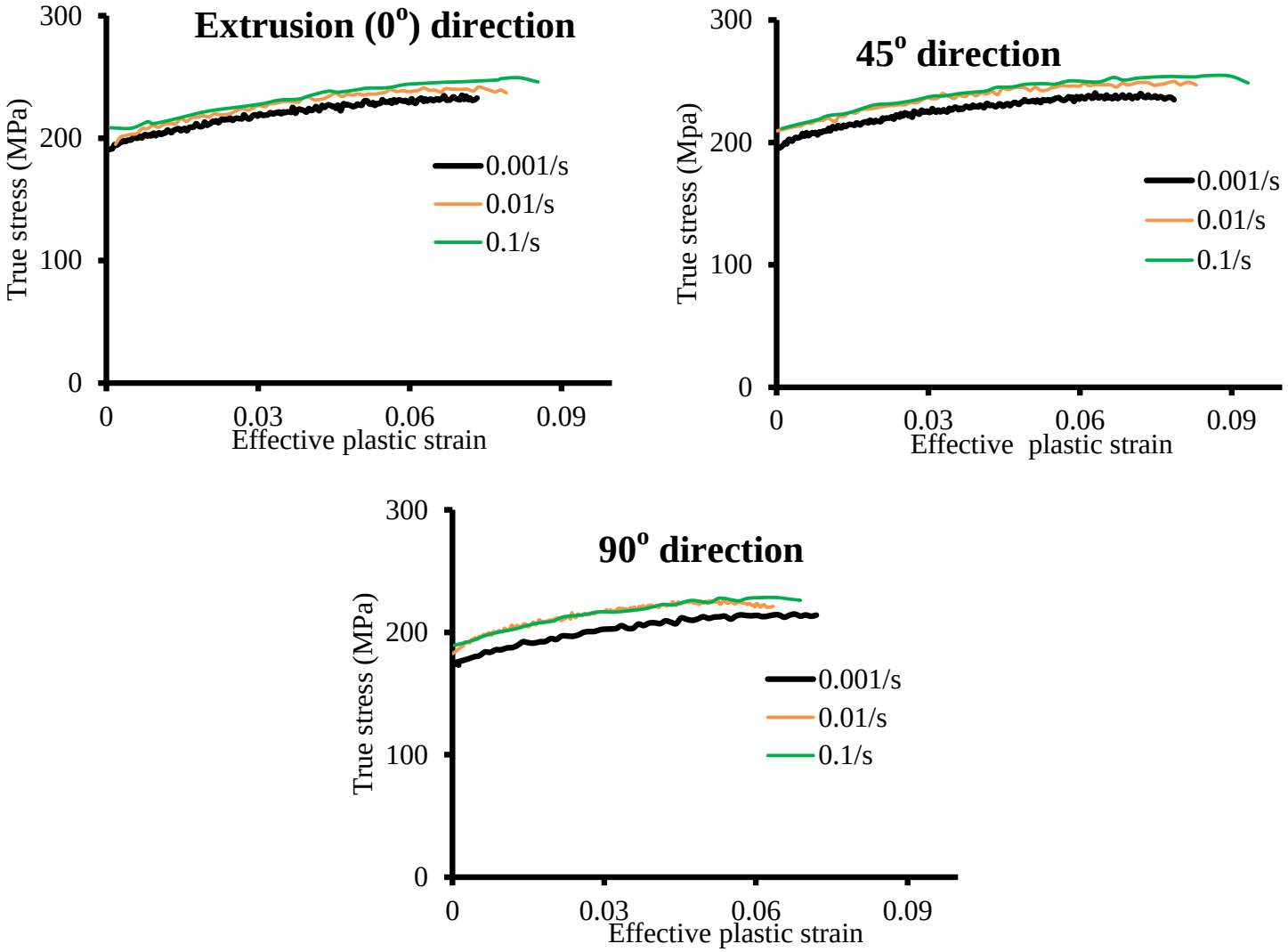

Figure 5.50: True stress vs. effective plastic strain curve alloy 4 (T6)

As seen in Figure 5.50, alloy 4 exhibits positive strain rate sensitivity in all three orientations. For the sample extracted along the extrusion direction and tested at $0.001s^{-1}$, it was observed that the maximum true stress was 235 MPa. The maximum true stress was observed to increase to 252.6 MPa for test performed at 0.1 s^{-1}. Similar trends were observed for the 45^o (increasing from 240 MPa at $0.001s^{-1}$ to 255 MPa at $0.1s^{-1}$) and the 90^o orientation samples. The maximum true stress value for all test strain rates was found to be greatest in the 45^o orientation samples and lowest in the 90^o orientation. In order to characterize the plastic anisotropy behavior of alloy 4, the flow stress ratio for each orientation was calculated. The flow stress ratio r_α in direction α is defined as [8]:

$$r_\alpha = \frac{\sigma_f^\alpha}{\sigma_f^0} \qquad (5.16)$$

where σ_f^α is the flow stress along direction α in a tensile test and σ_f^0 is the flow stress in the extrusion direction evaluated at the same strain as in direction α.

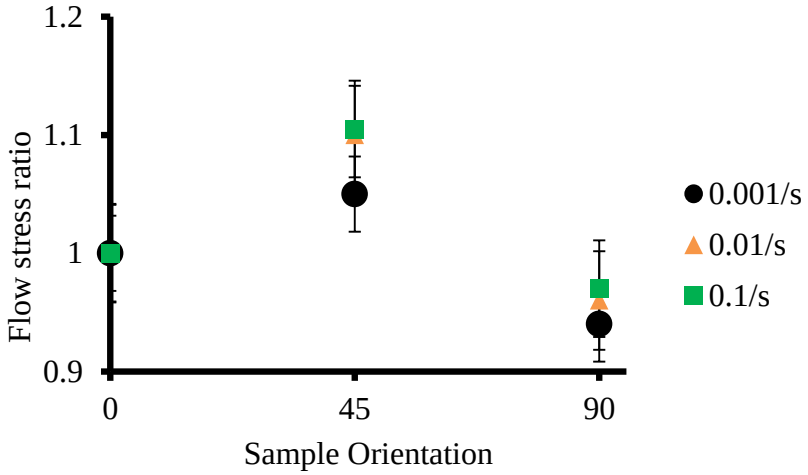

Figure 5.51: Flow stress ratio as a function of sample orientation and strain rate (alloy 4 T6)

Figure 5.51 is a plot of the flow stress ratio as a function of the sample orientation and strain rate determined at 5% strain. It is observed that the 45^o orientation samples exhibited a higher flow stress ratio than the 0^o samples for all test strain rates. This indicates that hardening is higher in

the 45^o direction than in the extrusion direction. Alloy 4 (T6) was observed to exhibit significant anisotropy in strength and has its strength increasing with increase in test strain rate. The Lankford coefficient or R-value defined as the ratio of plastic strain rates in the width and thickness directions under uniaxial tension was determined for each of the sample orientations. The average R-values for alloy 4 in the T6 condition were calculated over the range of 5-8% strain and are given in Table 5.6. The 90^o orientation samples were observed to have the highest R-value at the test strain rates. Alloy 4 (T6) exhibited anisotropic behavior in plastic flow as evidenced by the strong variation in R-value with material direction.

Table 5.6: Measured R-value as a function of sample orientation and strain rate (T6)

Sample Orientation	$0.001\ s^{-1}$	$0.01\ s^{-1}$	$0.1\ s^{-1}$
0	0.31	0.29	0.28
45	0.84	0.81	0.77
90	0.95	0.92	0.80

The R-value is a measure of the material's resistance to thinning; for the tested strain rates, the extrusion direction was observed to be the direction most prone to thinning. The true stress vs. effective plastic strain curves at different strain rates for alloy 4 samples in the T4 condition are shown in Figure 5.52.

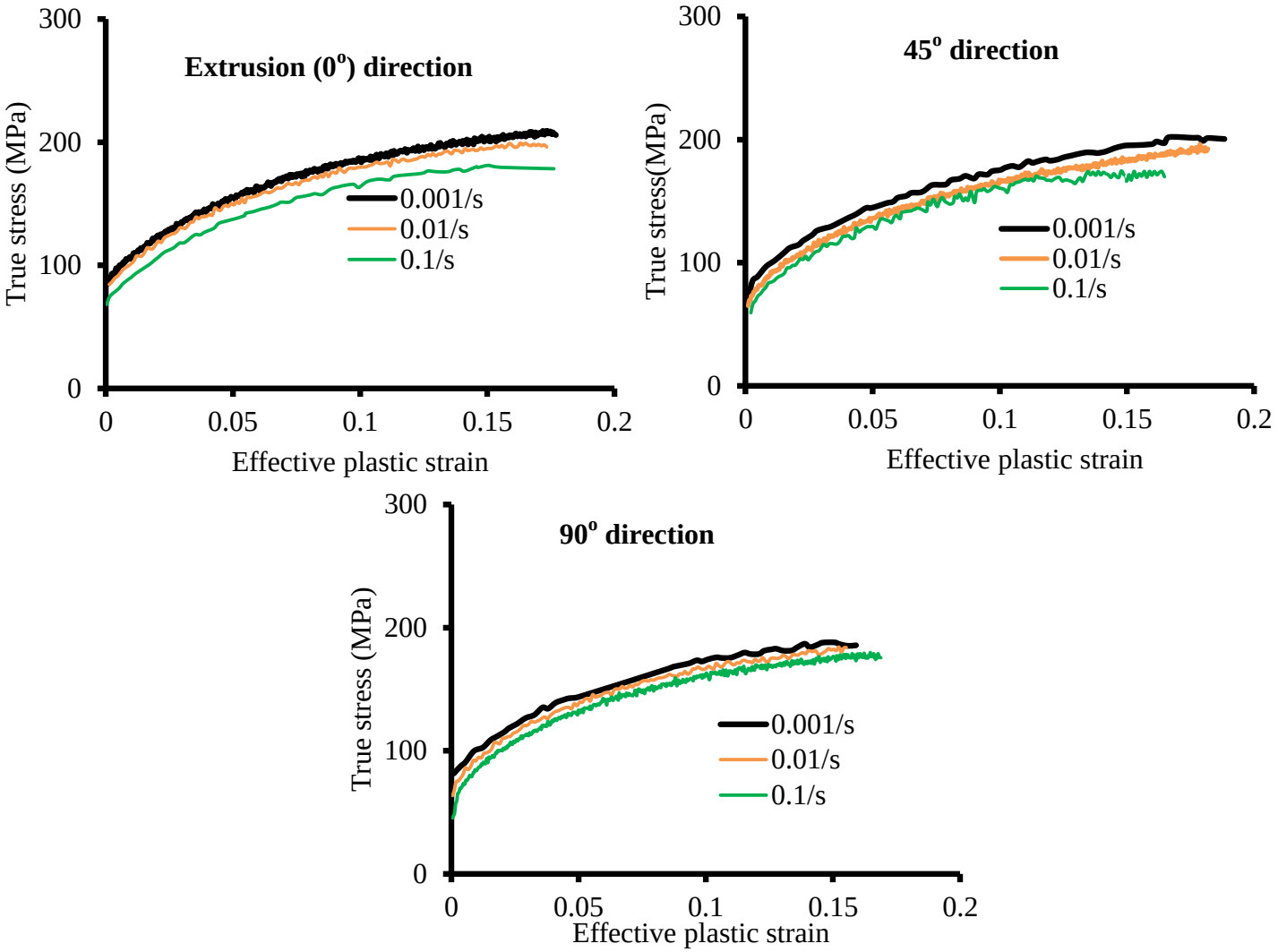

Figure 5.52: True stress vs. effective plastic strain curves alloy 4 (T4)

Alloy 4 exhibits negative strain rate sensitivity in the T4temper condition i.e. the strength reduces with higher deformation strain rate. However, the change in tensile strength with increasing strain rate is very minimal and can therefore be said to be within error margins. For the T4 sample, the strength level is highest along the extrusion direction (0^o) and lowest in the 90^o direction samples. In order to characterize the anisotropic behavior of alloy 4 in the T5 condition, the flow stress ratio and R-value for the three orientations were determined as a function of strain rate. Figure 5.53 is a plot of the flow stress ratio as a function of the sample orientation and strain rate at 5 % strain.

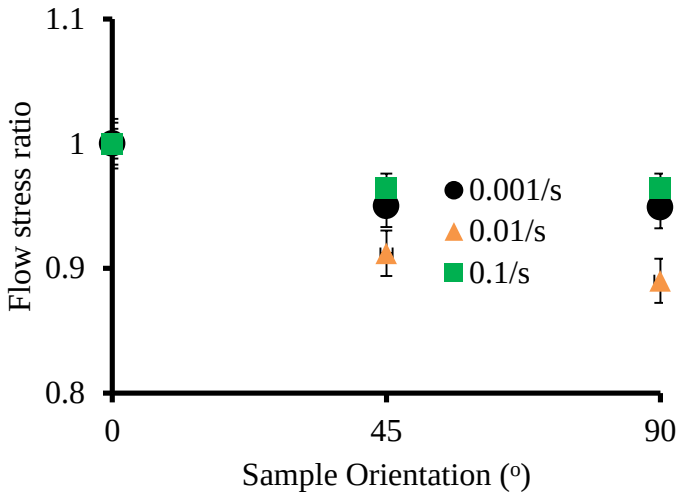

Figure 5.53: Flow stress ratio as a function of sample orientation and strain rate (alloy 4 T4)

As shown in Figure 5.53, alloy 4 exhibits reduced anisotropic behavior in the T4 condition in comparison with the T6 alloy (Figure 5.51). The 45^o and 90^o orientation samples had almost equal flow stress ratio values. The lower flow stress ratio of the 45^o and 90^o orientation samples indicates that hardening is greatest in the extrusion direction samples. The average R-value at 5-8 % strain for alloy 4 (T4) is given in Table 5.7.

Table 5.7: Measured R-value as a function of sample orientation and strain rate (T4)

Sample Orientation	0.001 s^{-1}	0.01 s^{-1}	0.1 s^{-1}
0	0.52	0.34	0.43
45	0.96	0.73	0.94
90	0.54	1.38	1.25

From Table 5.7, it is observed that the R-value had no clearly defined trend with respect to strain rate for alloy 4 in the T4 condition. However, the extrusion direction (0^o direction) had the lowest R-values and therefore has the lowest resistance to thinning implying that this direction is most prone to necking. Figure 5.54 shows the effect of temper condition on the tensile behavior of alloy 4.

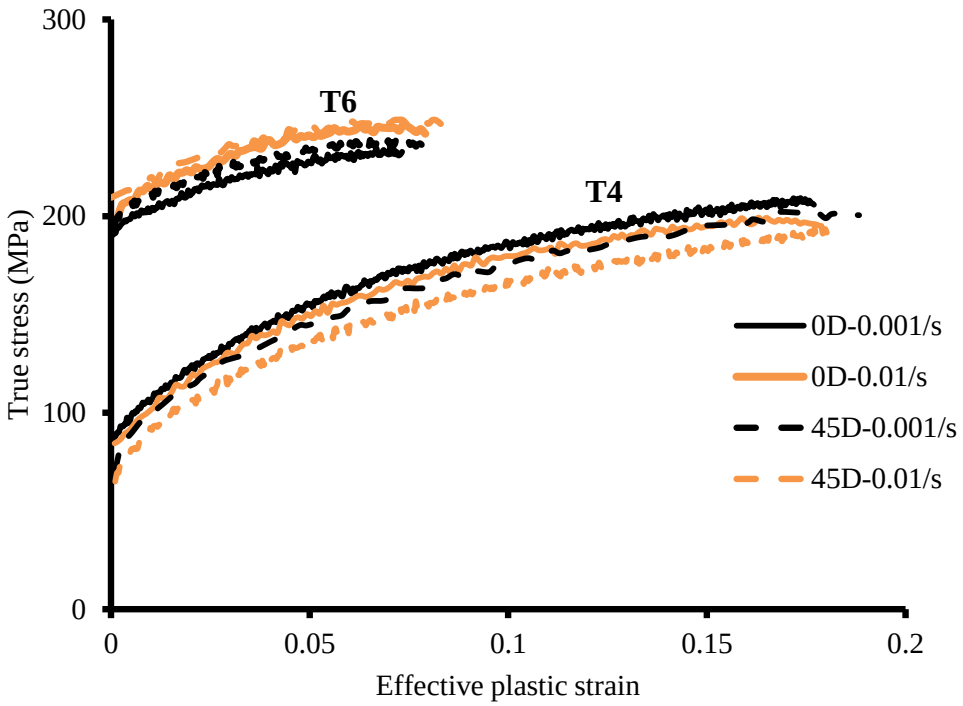

Figure 5.54: Effect of temper condition on tensile behavior of alloy 4

From Figure 5.54, it is observed that the T6 alloy exhibits greater strength than the naturally aged T4 alloy. This may be due to the amount of Mg_2Si particles that precipitated out of solution during the artificial aging of the T6 alloy. These Mg_2Si particles serve as obstacles to the movement of dislocations and therefore the T6 alloy is strengthened by solid solution precipitation hardening in comparison with the T4 material. Also, alloy 4 in the T4 condition possesses greater ductility than the T6 sample due to the fact that the Mg_2Si particles while improving strength has adverse effect on ductility. As the aging process proceeds, the force needed for precipitate shearing becomes larger resulting in increased strength and lower elongation.

The tensile properties of the laboratory and industrial extrusions of Al-Mg-Si alloys (after heat treatment to T6 condition) studied in this research were compared to the tensile properties of

other known aluminum alloys. Figure 5.55 shows the yield strength and elongation of the alloys relative to other AA6xxx, AA7xxx and AA2xxx aluminum alloys.

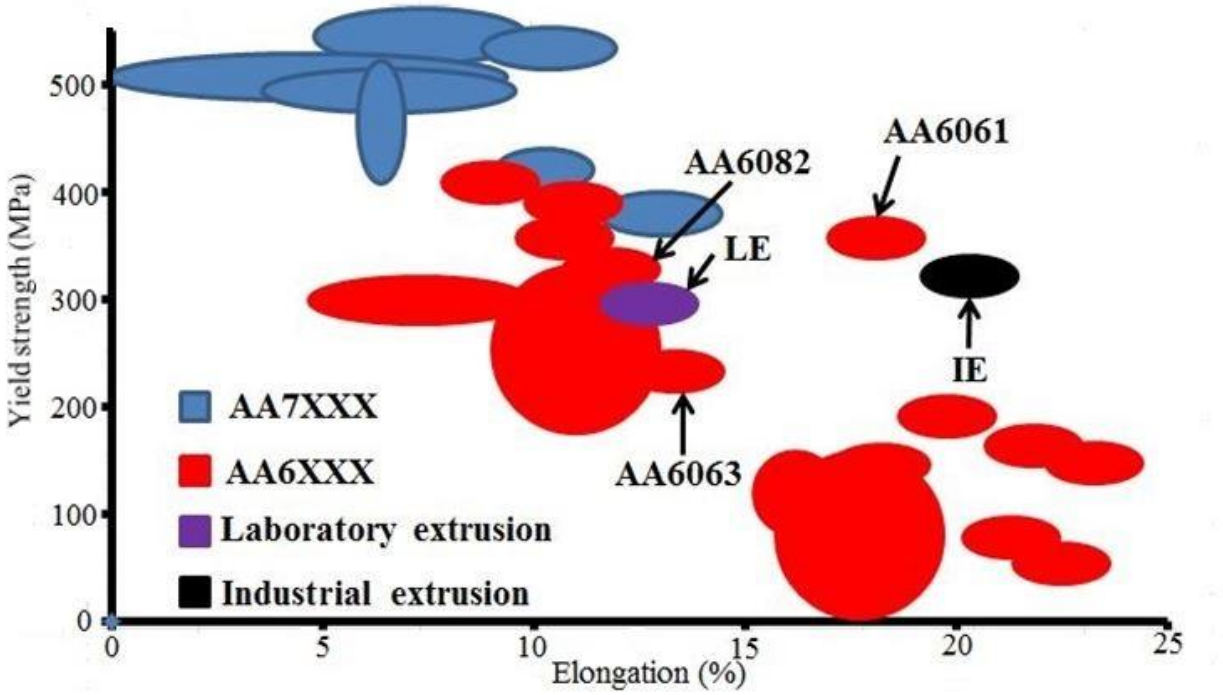

Figure 5.55: Tensile properties of extruded Al-Mg-Si alloys relative to other aluminum alloys

As seen in Figure 5.55, the laboratory extruded profiles exhibited equivalent ductility and higher strength than AA6063 while the industrial extrusion alloy profiles exhibited an improved ductility property and equivalent tensile strength in comparison with AA6082 alloy.

CHAPTER 6

Summary, Conclusions and Future Work

6.1. Summary

Increased effort towards manufacture of environmentally friendly automobiles that boast improved fuel efficiency and lightweight has led to the steady rise in the application of aluminum alloys as the materials of choice in the automotive industry. In this research, effort has been taken to better understand how processing conditions and alloy composition influence the mechanical properties of extruded Al-Mg-Si alloys. The specific objectives of this research included understanding the role of alloy composition on the hot flow stress behavior and extrudability, effect of extrusion process parameters and alloy composition on surface to surface microstructure of extruded profiles as well as influence of alloy composition, extrusion processing parameters and post extrusion heat treatment on the mechanical properties of Al-Mg-Si alloys.

The influence of changes in the Mg-Si content and the addition of 0.2 wt. % Cr on the hot flow stress behavior of Al-Mg-Si alloys was determined by performing hot deformation compression experiment on AA6xxx alloys. Using the hyperbolic sine equation, constitutive models were developed for predicting the hot flow stress behavior of these alloys. The effects of alloy composition on average steady flow stress, activation energy and the strain rate sensitivity parameter were explained by solid solution strengthening mechanism which involves solute atoms serving as obstacles to dislocation movement.

In order to determine the influence of increased Mg-Si in solution on the hot flow strength behaviour of Al-Mg-Si alloys, hot deformation compression tests were performed on samples after holding at test temperature for different times to allow for different levels of Mg-Si

in solid solution. Using a one-dimensional particle dissolution model based on Fick's second law, the Mg-Si solute content was determined as a function of hold time and deformation temperature. The particle dissolution model was verified by correlating the resistivity measurement of samples held at 450 ^{o}C with the predicted solute content through Matthiessen's law. A new constitutive model was developed which involved accounting for the Mg-Si solute content (as a function of hold time and temperature) on the hot flow stress behavior using the well-known Sellars-Tegart hyperbolic sine equation. The developed constitutive model steady state flow stress predictions showed good agreement with experimental data measured in this research and also flow stress data available in literature for Al-Mg-Si alloys.

The influence of alloy composition and extrusion ratio on the microstructure of Al-Mg-Si alloys was studied by examining the through thickness microstructure of alloys extruded at extrusion ratios of E_R = 44 and 40. For the alloys extruded at low E_R, extruded profiles containing 0.2 wt % Cr were observed to exhibit a recrystallized surface layer filled with small fine grains while peripheral coarse grains were observed in the extruded profiles with no Cr content. The surface to surface microstructures of the industrial extrusion alloys revealed presence of peripheral coarse grains (PCG) irrespective of the presence of Cr. The presence of PCG may be due to the higher speed at which extrusion was performed. This implies an increase in the strain rate experienced by the alloy profiles during the extrusion process – a favorable condition for recrystallization.

The role of alloy composition on extrudability of Al-Mg-Si alloys was determined by performing laboratory scale extrusion on Al-Mg-Si with varying Mg-Si content and with/ without 0.2 wt. % Cr addition. Similar to prior research, the extrudability of the Al-Mg-Si alloys was observed to decrease with an increase in the Mg-Si content as well as the addition of 0.2 wt

% Cr. The decrease in extrudability of these alloys is believed to be due to an increase in flow stress due to addition of Cr and increase in Mg-Si content. Laboratory scale extrusion trials were performed at 480, 500 and 520 ^{o}C on these alloys and showed the strong effect of temperature on the subsequent T5 hardness property. Higher extrusion temperature ensured increased dissolution of Mg-Si in solution to ensure strengthening by precipitation during subsequent age hardening. Quasi-static tensile tests at $0.1s^{-1}$ were conducted on tensile samples extracted along the extrusion direction in order to determine the influence of extrusion temperature and aging time on the mechanical properties of these alloys. The strength and ductility properties in the T4, T5 and T6 conditions were observed to increase and decrease respectively with Mg-Si content. The addition of Cr appeared to improve ductility but had a slight influence on strength in the T4 condition. The fracture surface of the alloys was examined by scanning electron microscopy. The alloys containing Cr were observed to exhibit ductile dimple fracture and a transgranular morphology while an intergranular fracture was observed in the Al-Mg-Si alloys with no Cr content. In order to determine the strain rate sensitivity and anisotropic behavior of one of these alloys, quasi-static tensile test was performed at 0.001, 0.01 and $0.1s^{-1}$ on samples extracted along the extrusion, 45^{o} and 90^{o} orientations. The anisotropic behavior of the alloy in the T5 and T6 conditions was characterized by calculating the Lankford coefficient and flow stress ratio. Results indicate that samples extruded in the industrial scale extrusion press have equivalent strength and higher ductility than samples that were extruded in the laboratory scale extrusion equipment. This observation could be due to the higher speeds and hence higher strain rates experienced by the profiles during the industrial extrusion process which leads to a more refined microstructure.

6.2. Conclusion

The influence of alloy composition on the flow stress behavior of Al-Mg-Si alloys has been studied in this research. Also, an Mg-Si solute dependent constitutive model has been developed for prediction of the hot deformation flow stress behavior of Al-Mg-Si alloys. The major conclusions of this research are identified in four sections: effect of alloy composition on hot deformation of Al-Mg-Si alloys, prediction of the hot flow stress behavior of an Al-Mg-Si alloy including Mg_2Si dissolution, formation of peripheral coarse grains in extruded Al-Mg-Si alloys and effect of alloy composition and processing condition on the extrudability, mechanical properties and fracture morphology of extruded Al-Mg-Si alloys.

Effect of alloy composition on hot deformation of Al-Mg-Si alloys

- The activation energy for hot deformation of Al-Mg-Si alloys increase with an increase in the Mg-Si content and also due to addition of 0.2 wt. Cr. An increase in the Mg-Si content and addition of Cr were observed to result into 11 % and 15 % increase in activation energy respectively. The strain rate sensitivity parameter was observed to reduce by 16.5 % with an increase in the Mg-Si content while addition of 0.2 wt % Cr resulted into 12 % decrease in strain rate sensitivity parameter of these alloys.
- Using the Sellars-Tegart constitutive model, constitutive equations for predicting the hot deformation flow stress behavior of the Al-Mg-Si alloys were developed. Comparisons indicated that the model predicted flow stress agree well with measured values during hot deformation compression over a wide range of temperature and strain rate.

Prediction of the hot flow stress behavior of an Al-Mg-Si alloy including Mg_2Si dissolution

- An increase in the Mg and Si solute content with increasing hold time results into increase in the flow stress of an Al-Mg-Si alloy by increasing the alloy's deformation resistance.

- Accounting for the Mg and Si solute content level as a function of hold time at test temperature actually results into the development of a more accurate constitutive equation, which is a numerical tool for prediction of the hot flow stress behavior of Al-Mg-Si alloys.
- A new constitutive equation for predicting the hot flow stress behavior of an Al-Mg-Si alloy has been developed. This constitutive equation incorporates temperature and strain rate as well as amount of Mg-Si in solid solution. This constitutive model will serve as an effective tool for modeling forming processes such as extrusion in which the temperature range during the process affects the amount of Mg-Si in solution.

Formation of peripheral coarse grains in extruded Al-Mg-Si alloys

- The microstructures of Al-Mg-Si alloys that contain Cr were observed to be different from those without Cr. The Cr promotes the formation of dispersoids that prevent grain boundary migration and grain growth by Zener pinning resulting in a fibrous core. The surface layers of transition element containing extruded Al-Mg-Si alloys were observed to exhibit a more recrystallized grain structure than the core. The increase in temperature due to friction between the billet surface and die during the extrusion process is believed to result in an increase in the stored energy at the surface layer – a favorable condition for occurrence of recrystallization. However, peripheral coarse grains were observed in the surface layer of the industrial extrusion profiles irrespective of the presence of transition metal additions. The higher speed resulting into increased strain rate during the industrial scale extrusions of the alloys may be responsible for increased stored energy in the surface layer of the extruded profiles – a favorable condition for recrystallization.

Effect of alloy composition and processing condition on the extrudability and mechanical properties of extruded Al-Mg-Si alloys

- ❖ Alloy composition has an influence on the extrudability (speed and required extrusion load) of Al-Mg-Si alloys. An increase in the Mg-Si content and addition of Cr were observed to result in 44 % and 50 % decrease in ram speed respectively.
- ❖ Alloy composition has an influence on the tensile properties of extruded Al-Mg-Si alloys. The yield and ultimate tensile strengths of Al-Mg-Si alloys was observed to increase with an increase in the Mg-Si content and addition of 0.2 wt % Cr. Results show that the ductility of Al-Mg-Si alloys increase with addition of 0.2 wt % Cr but reduces with increased Mg-Si content.
- ❖ The fracture morphology of extruded and heat treated Al-Mg-Si alloys depend on the alloy composition. Extruded profiles containing 0.2 wt % Cr exhibit ductile fracture morphology while the alloy with no Cr content was observed to exhibit intergranular fracture morphology with small crack tips. This may be due to the presence of Cr dispersoids that have been previously reported to prevent attainment of critical local strain required for intergranular crack nucleation.

6.3. Future Work

Influence of alloy composition on hot flow stress behavior of Al-Mg-Si alloys

- In order to develop a universal constitutive model that is suitable for predicting the hot deformation flow stress behavior of Al-Mg-Si alloys, there exists the need to study the effect of other elemental additions on the flow stress, activation energy and strain rate sensitivity parameter of Al-Mg-Si alloys. It is believed that such universal constitutive model and other process variables can be incorporated into iterative algorithms for effective modeling of forming processes such as extrusion and rolling.

- Study the effect of deformation conditions such as temperature and strain rate on interaction of transition metal solute atoms with mobile dislocations during the hot deformation of Al-Mg-Si alloys. It is believed that deformation conditions such as strain rate and temperature can affect the diffusivity of transition metal solute atoms (such as Cr and V solute atoms) in aluminum and their dislocation blocking roles during hot deformation of Al-Mg-Si alloys.

Prediction of the hot flow stress behavior of an Al-Mg-Si alloy including Mg_2Si dissolution

- Verifying the effect of average Mg_2Si particle radius r_o on the Mg-Si solute content will be beneficial in better validating the developed model for predicting the hot deformation behavior of Al-Mg-Si alloys.
- In order to develop a more versatile tool for predicting the hot deformation flow stress behavior of Al-Mg-Si alloys, there exists the need to investigate the combined effect of heating rate and hold time at deformation temperature on the Mg-Si solute content during the hot deformation compression of Al-Mg-Si alloys.

Effect of extrusion condition on microstructure of extruded Al-Mg-Si alloys

- Study the effect of homogenization and extrusion process variables such as temperature and die geometry on the formation of peripheral coarse grains in extruded Al-Mg-Si alloys.
- Develop a model for calculating the critical stored energy for formation of coarse grains in extruded Al-Mg-Si alloys as a function of extrusion conditions such as temperature and ram speed. This will serve as a knowledge base for extruders when trying to avoid formation of coarse surface layers in extruded Al-Mg-Si alloys.

Effect of alloy composition and extrusion condition on extrudability and mechanical properties of Al-Mg-Si alloys

- Development of a mathematical relation for calculating the hardness of extruded Al-Mg-Si alloys given the extrusion condition. This will ensure that the hardness property of an extruded profile can be estimated without performing time consuming and expensive experiment. Using the hardness data measured in this work, a regression analysis model can be developed for calculating the hardness of Al-Mg-Si alloys as a function of extrusion temperature.
- Study the effect of paint bake cycle on the strength and ductility properties of the extruded and aged Al-Mg-Si alloys in order to better understand the behavior of these alloys in service conditions.
- Study area reduction as a measure of the fracture resistance behavior of the Al-Mg-Si alloys. Also, it is important to understand the effect of alloy composition on the bendability of the alloys studied in this work.
- There exists the need for thorough investigation of texture evolution during the hot compression deformation of the Al-Mg-Si alloys. This will help in providing more detailed understanding of the flow behavior of these alloys.

References

1. http://www.aluminiumleader.com/en/around/transport/cars[assessed March 7 2017]
2. 2015 Ducker Worldwide Aluminum Survey DriveAluminum.org/ducker/ [assessed March 2017]
3. Aluminum in cars –European Aluminum Association (2008) bulletin http://www.alueurope.eu[assessed March 7 2017]
4. 2015 North American light vehicle aluminum content study executive summary (2014) 1-24
5. Cuoto K.B.S, Claves S.R, Van Geertruyden W.H, Misiolek Z, Goncalves M, "Effect of homogenization treatment on microstructure and hot ductility of aluminum alloy 6063" Materials Science and Technology Vol 21 No. 2 (2005) pp 263-268
6. Zhu H, Couper M.J, Dahle A.K, "Effect of process variables on Mg-Si particles and extrudability of 6XXX series aluminum extrusions" The Journal of The Minerals, Metals & Materials Society (TMS) Vol. 63 Issue 11 (2011) pp 66-71
7. Troeger L.P, Starke E.A, "Microstructural and mechanical characterization of a superplastic 6XXX aluminum alloy" Materials Science and Engineering A Vol 277 Issue 1-2 (2000) pp 102-113
8. Chen Y, Clausen A.H, Hopperstad O.S, Langseth M., "Stress-strain behavior of aluminum alloys at a wide range of strain rates International Journal of Solids and Structures Vol 46 Issue 21 (2009) pp 3825-3835
9. Ducker Worldwide Aluminum content in cars summary report (2016) pp 1-13
10. http://blog.caranddriver.com/in-depth-with-the-2015-ford-f-150s-aluminum-presented-in-an-alloy-of-facts-and-perspective/ [Assessed March 7 2017]
11. Aluminum properties and physical metallurgy American Society for Metals, Edited by John E. Hatch Metals park Ohio (1984)
12. Prakash V, Physical metallurgy of aluminum alloyseprints.nmlindia.org/4453/1/Paper_No.16
13. Parson N.C, Yiu H.L, "The effect of heat treatment on the microstructure and properties of 6000 series alloy extrusion ingots" Light Metals (1989) pp 713-722
14. Cobden R, "Aluminum: physical properties, characteristics and alloys training in aluminum application technologies" www.alueurope.eu/talat/lectures/501.pdf
15. Mondolfo L.F, "Aluminum alloys: structure and properties" Butterworth London (1976) pp 807-817
16. Okorafor O.E, "Effect of heat treatment on the corrosion resistance of 6063 aluminum alloy" Corrosion Prevention and Control Vol 38 No 6 (1991) pp 141-144

17. www.vosbltd.com/images/matallurgy.pdf [Assessed October 13 2014]

18. Lodgaard L, Ryum N., "Precipitation of dispersoids containing Mn and/or Cr in Al-Mg-Si alloys" Materials Science and Engineering A Vol 283 Issue 1-2 (2000) pp 144-152

19. Reiso O, "Extrusion of AlMgSi alloys" Materials Forum Institute of Materials Engineering Australasia Vol 28 (2004) pp 32-46

20. Siddiqui R.A, Abdullah H.A, Al-Belushi K.R, "Influence of aging parameters on the mechanical properties of 6063 aluminum alloy" Journal of Materials Processing Technology Vol 102 Issue 1-3 (2000) pp 234-240

21. Bourget J.-P, Fafard M, Shakeri H.R, Cote T, "Optimization of heat treatment in cold-drawn 6063 aluminum tubes" Journal of Materials Processing Technology Vol 209 Issue 11 (2009) pp 5035-5041

22. www.azom.com/article.aspx?article ID=2813#application_of_aluminum [assessed October 10 2014]

23. Usta M, "The influence of thermal treatment on the cast structure of 6XXX aluminum alloys" PhD thesis Rensselaer Polytechnic Institute Troy, New York (2001)

24. http://www.aluminiumdesign.net/design-support/extrusion-process/ [assessed March 7 2017]

25. Kelesoglu E, Erarslan Y, Ozer G, "Deformation character of the aluminum alloy AA6063 depending on the homogenization state" MP Materials Testing Vol 51 No 6 (2009) pp 390-394

26. Das G, Das M, Ghosh S, Dubey P, Ray A.K, "Effect of aging on mechanical properties of 6063 Al-alloy using instrumented ball indentation technique" Materials Science and Engineering A Vol 527 Issue 6 (2010) pp 1590-1594

27. Skjerpe P, "Intermetallic phases formed during DC-casting of an Al−0.25 wt Pct Fe−0.13 wt Pct Si alloy" Metallurgical Transactions A Vol 18 Issue 2 (1987) pp 189-200

28. Birol Y, "The effect of homogenization practice on the microstructure of AA6063 billets" Journal of Materials Processing Technology Vol 148 Issue 2 (2004) pp 250-258

29. Rivas A.L, Munoz P, Camero S, Quintero-Sayago O, "Effect of the microstructure on the mechanical properties and surface finish of an extruded AA6063 aluminum alloy" Advanced Materials Science and Technology Vol 2 No 1 (1999) pp 15-23

30. Karamis M.B, Halici I, "The effects of homogenization and recrystallization heat treatments on low-grade cold deformation properties of AA6063 aluminum alloy" Materials Letters Vol 61 Issue 4-5 (2007) pp 944-948

31. Dons A.L, “The Alstruc homogenization model for industrial aluminum alloys” Journal of Light Metals Vol 1 Issue 2 (2001) pp 133-149
32. Aluminum extrusion technology ASM international (2000) #06826G
33. Zhang C, Zhao G, Chen Z, Chen H, Kou F, “Effect of extrusion stem speed on extrusion process for a hollow aluminum profile” Materials Science and Engineering B Vol 177 Issue 19 (2012) pp 1691-1697
34. Zhao Y, Song B, Pei J, Jia C, Li B, Linlin G, “Effect of deformation speed on the microstructure and mechanical properties of AA6063 during continuous extrusion process” Journal of Materials Processing Technology Vol 213 Issue 11 (2013) pp 1855-1863
35. Aytac A, Dascilar B, Usta A, “The effect of extrusion speed on the structure and corrosion properties of aged and non-aged 6063 aluminum alloy” Materials Chemistry and Physics Vol 130 Issue 3 (2011) pp 1357-1360
36. Parson N, Barker S, Shalanski A, Jowett C, “Control of grain structure in Al-Mg-Si extrusions” Proceedings of the Eighth International Aluminum Extrusion Technology Seminar Orlando Florida 1 (2004) pp 11-22
37. Ishikawa T, Sano H, Yoshida Y, Yukawa N, Sakamoto J, Tozawa Y, “Effect of Extrusion Conditions on Metal Flow and Microstructures of Aluminum Alloys” CIRP Annals - Manufacturing Technology Vol 55 Issue 1 pp 275-278
38. Sweet E.D, Caraher S.K, Danilova N.V, Zhang X, “Effects of Extrusion Parameters on Coarse Grain Surface Layer in 6xxx-Series Extrusions” Proceedings of International Aluminum Extrusion Technology Seminar Florida 1 (2004) pp 115-126
39. Ihara K, Shikama T, Morita K, “The effect of extrusion temperature on the recrystallization texture of an extruded AA6005C alloy” Research and Development Kobe Steel Engineering Reports Vol 62 Issue 2 (2012) pp 43-47
40. Bryant A.J, “Effect of extrusion temperature on the toughness of aluminum alloys in extruded form” Journal of the Institute of Metals Vol 100 (1972) pp 191-196
41. Karabay S, Zeren M, Yilmaz M, “Investigation of extrusion ratio effect on mechanical behavior of extruded alloy AA6063” Journal of Materials Processing Technology Vol 135 Issue 1 (2003) pp 101-108
42. Demirci H.I, Evlen H, “Effect of extrusion ratio on the wear behavior of Al-Si and Al-Mg alloys” Journal of Alloys and Compounds Vol 510 Issue 1 (2012) 26-32
43. Tomovic-Petrovic S, Jensrud O, “Extrusion of silicon-rich AlMgSi alloys” Journal of Materials Processing Technology Vol 212 Issue 6 (2012) pp 1437-1442

44. Langerweger J, "How casting billet methods can affect the quality of 6063 extrusion billet" Proceedings of the 4th International Aluminum Extrusion Technology Seminar Washington DC Vol 2 (1988) pp 381-384

45. Evangelista E, McQueen H.J, Kassner M.E, Spigarelli S, "Hot Deformation and Processing of Aluminum Alloys" CRC Press Taylor and Francis (2011)

46. Lang G, Castle A.F, "Influence of copper, manganese and chromium additions on the extrudability of AlMgSi alloys" Proceedings of Second International Aluminum Extrusion Technology Seminar Dusseldorf Vol 1 (1977) pp 293-296

47. Zajac, S, Gullman L.O, Johnson A, Proceedings of the Third International Conference on Aluminum Alloys Trondheim, Vol 2 (1992) pp 133-l 38

48. Meng Y, Cui J, Zhao Z, He H, "Effect of Zr on microstructures and mechanical properties of an Al-Mg-Si-Cu-Cr alloy prepared by low frequency electromagnetic casting" Materials Characterization Vol 92 (2014) pp 138 – 148

49. Guemini R, Boubertakh A, Lorimer G.W, "Study of the recrystallization process of AlMgSi alloys containing transition elements" Journal of Alloys and Compounds Vol 486 Issues 1-2 (2009) pp 451–457

50. Fan X.H, Li M, Li D.Y, Shao Y.C, Zhang S.R, Peng Y.H, "Dynamic recrystallization and dynamic precipitation in AA6061 aluminum alloy during hot deformation" Materials Science and Technology Vol 30 Issue 11 (2014) pp 1263-1272

51. Deschamps A, Niewczas M, Bley F, Brechet Y, Embury J.D, Le Sinq L, Livet F, Simon J.P, "Low-temperature dynamic precipitation in a supersaturated Al-Zn-Mg alloy and related strain hardening" Philosophical Magazine A, Vol 79 No. 10 (1999) pp 2485-2504

52. Humphreys F.J, Hatherly M, "Recrystallization and related annealing phenomena" 2nd Edition (2004) Elsevier Ltd UK

53. Yamagata H, "Dynamic recrystallization of single-crystalline aluminum during compression tests" Scripta Metallurgica et Materialia Vol 27 Issue 2 (1992) pp 727–732

54. Sheppard T, Tutcher M.G, "Development of duplex deformation substructure during extrusion of a commercial Al-5Mg-0.8 Mn Alloy" Metal Science Vol 14 Issue 12 (1980) pp 579-590

55. Yamagata H, "Multipeak stress oscillations of five-nine-purity aluminum during a hot compression test" Scripta Metallurgica et Materialia Vol 27 Issue 2 (1992) pp 201-203

56. Perdrix C, Perrin M.Y, Montheillet F, “Comportement mecanique et evolution structural de l'aluminium au cours d'une deformation a chaud de grande amplitude” Mem. Sci. Rev. Metall, Vol 78 (1981) pp 309-20

57. Montheillet F, “Les traitements thermomecaniques” (ed.) P. Costa et. al., INSTN Paris, (1981) pp. 57-70

58. Shi C, Lai J, Chen X.-G, “Microstructural evolution and dynamic softening mechanisms of Al-Zn-Mg-Cu Alloy during hot compressive deformation” Materials Vol 7 (2014) Materials pp 244-264

59. Foydl A, Segatori A, Ben Khalifa N, Donati L, Brosius A, Tomesani L, TekkayaA.E, “Grain size evolution simulation in aluminum alloys AA 6082 and AA 7020 during hot forward extrusion process” Materials Science and Technology Vol 29 Issue 1 pp 100-110

60. Gourdet S, Montheillet F, “An experimental study of the recrystallization mechanism during hot deformation of aluminum” Materials Science and Engineering A Vol 283 (2000) pp 274–288

61. Guzel A, Jager A, Parvizian E, Lambers H.G, Tekkaya A.E, Svendsen B, Maier H.J, “A new method for determining dynamic grain structure evolution during hot aluminum extrusion” Journal of Materials Processing Technology Vol 212 Issue 1 (2012) pp 323–330

62. Pari L.D, Misiolek W.Z, “Theoretical predictions and experimental verification of surface grain structure evolution for AA6061 during hot rolling” Acta Materialia Vol 56 Issue 20 (2008) pp 6174–6185

63. McQueen H.J, Knustad O, Ryum N, Solberg J.K, “Microstructural evolution in al deformed to strains of 60 at 400°C” Scripta Metallurgica Vol. 19 (1985) pp 73-78Pergamon Press Ltd

64. Solberg J.K, MCQueens H.J, Ryum N, Nes E, “Influence of ultra-high strains at elevated temperatures on the microstructure of aluminum” Part I Philosophical Magazine A, Vol 60 No 4 (1989) pp 447-471

65. Polettia C, Rodriguez-Hortalá M, Hauser M, Sommitsch C, “Microstructure development in hot deformed AA6082” Materials Science and Engineering A Vol 528, Issue 6, (2011) pp 2423–2430

66. Wang M, Zhao H, Wu X, Li C, Li G, “Deformation simulation of low temperature high-speed extrusion for 6063 Al alloy” Journal of Central South University of Technology Vol 17 Issue 5 (2010) pp 881-887

67. McQueen H.J, Ryan N.D, “Constitutive analysis in hot working” Materials Science and Engineering A Vol 322 Issue 1-2 (2002) pp 43-63

68. Tello K.E, Gerlich A.P, Mendez P.F, “Constants for hot deformation constitutive models for recent experimental data” Institute of Materials, Minerals and Mining Vol 15 No 3 (2010) pp 260-266

69. Sellars C.M, McTegart W.J, “On the mechanism of hot deformation” Acta Metallurgica Vol 14 Issue 9 (1966) 1136-1138

70. Sah J.P, Richardson G.J, Sellars J, “Recrystallization during hot deformation of nickel” Journal of Australian Institute of Metals Vol 14 Issue 4 (1969) pp 292-297

71. Van de Langkruis J, Bergwerf R, Van der Zwaag S, Kool W, "Linking plane strain compression tests on AA6063 to laboratory scale extrusion via constitutive equations" Materials Science Forum Vol 331-337 (2000) pp 565-570

72. Anjabin N, Taheri A, Kim H, "Constitutive modeling of hot deformation behavior of the AA6063 alloy with different precipitates" Metallurgical and Materials Transaction A Vol 44 Issue 13 (2013) pp 5853-5860

73. Espedal H, Gjestland H, Ryum N, McQueen H, "Hot deformation of Al-Mg-Si alloys" Scandinavian Journal of Metallurgy Vol 18 (1989) pp 131-136

74. Van de Langkruis J, Kool W, Van der Zwaag S, "Modification of a thermomechanical model to predict constitutive behavior of Al-Mg-Si alloys" Journal of Materials Engineering and Performance Vol 15 Issue 6 (2006) pp 632-639

75. Van de Langkruis J, Kool W, Sellars C, Van der Winden M, Van der Zwaag S, "The effect of β, β^{I} and β^{II} precipitates in a homogenized AA6063 alloy on the hot deformability and the peak hardness" Materials Science and Engineering A Vol 299 No 1-2 (2001) pp 105-115.

76. Kocks U, Chen S, “Constitutive laws for deformation and dynamic recrystallization in cubic metals” 7th Japan Institute of metals International Symposium on Aspects of High Temperature Deformation and Fracture in Crystalline Materials Nagoya (1993) pp 1-9

77. Liao H, Wu Y, Zhou K, Yang J, “Hot deformation behavior and processing map of Al-Mg-Si alloys containing different amount of silicon based on Gleeble 3500 hot compression simulation” Materials and Design Vol 65 (2015) pp 1091-1099

78. Wang C, Yu F, Zhao D, Zhao X, Zuo L, “Effect of Si content on deformation behavior of DC cast Al-Si alloys” Advanced Materials Research Vol 652-654 (2013) pp 1080-1083

79. Odoh D, Mahmoodkhani Y, Whitney M, Wells M, "Prediction of the Hot Flow Stress Behavior of AA6063 Including Mg_2Si Dissolution" Journal of Materials Engineering and Performance Vol 26 Issue 3 (2017) pp 1186-1194

80. Nes E, Marthinsen K, Ronning B, "Modeling the evolution in microstructure and properties during processing of aluminum alloys" Journal of Materials Processing Technology Vol 117 Issue 3 (2001) pp 333-340

81. Zhang B, Baker T.N, "Effect of the heat treatment on the hot deformation behavior of AA6082 alloy" Journal of Materials Processing Technology Vol 153-154 (2004) pp 881-885

82. Shakiba M, "Effect of homogenization and alloying elements on hot deformation behaviour of 1xxx series aluminum alloys" PhD Thesis University of Quebec at Chicoutimi

83. Shakiba M, Parson N, Chen X.-G, "Effect of iron and silicon content on the hot compressive deformation behavior of dilute Al-Fe-Si alloys" Journal of Materials Engineering and Performance Vol 24 Issue 1 (2015) pp 404-415

84. Shi C, Chen X.-G, "Effect of vanadium on hot deformation and microstructural evolution of 7150 aluminum alloy" Materials Science and Engineering A Vol 613 (2014) pp 91-102

85. Panigrahi S.K, Jayaganthan R, Pancholi V, "Effect of plastic deformation conditions on microstructural characteristics and mechanical properties of Al6063 alloy" Materials and Design Vol 30 Issue 6 (2009) pp1894-1901

86. Gavgali M, Totik Y, Sadder R, "The effects of artificial aging on wear properties of AA6063 alloy" Materials Letters Vol 57 Issue 24-25 (2003) pp 3713-3721

87. Zuo X, Jing Y, "Investigation of the age hardening behavior of 6063 aluminum alloys refined with Ti, RE and B" Journal of Materials Processing Technology Vol 209 Issue 1 (2009) pp 360-366

88. Munitz A, Cotler C, Talianker M, "Aging impact on mechanical properties and microstructure of Al-6063" Journal of Materials Science Vol 35 Issue 10 (2000) pp 2529-2538

89. Jiang D.M, Hong B.D, Lei T.C, Downham D.A, Lorimer G.W, "Influence of aging condition on tensile and fatigue fracture behavior of aluminum alloy 6063" Materials Science and Technology Vol 7 Issue 11 (1991) pp 1010-1014

90. Ozturk F, Esener E, Toros S, Picu C, "Effects of aging parameters on formability of 6061-O alloy" Materials and Design Vol 31 Issue 10 (2010) pp 4847-4852

91. Ceresara S, Di Russo E, Fiorini P, Giarda A, "Effect of Si excess on the ageing behaviour of Al-Mg_2Si 0.8% alloy" Materials Science and Engineering Vol 5 Issue 4 (1970) pp 220-227

92. Ding X.P, Cui H, Zhang J.X, Li H.X, Gui M.X, Lin Z, Zhuang L.Z, Zhang J.S, "The effect of Zn on the age hardening response in an Al-Mg-Si alloy" Materials and Design Vol 65 (2015) pp 1229-1235

93. Hirth S.M, Marshall G.J, Court S.A, Lloyd D.J, "Effect of Si on the aging behavior and formability of aluminum alloys based on AA6016" Materials Science and Engineering A Vol 319-321 (2001) pp 452-456

94. Miao W.F, Laughlin D.E, "Effects of Cu content and pre-aging on precipitation characteristics in aluminum alloy 6022" Metallurgical and Materials Transaction A Vol 31A (2000) pp 361-371

95. Fiawoo M, Gao X, Bourgeois L, Parson N, Zhang X.Q, Couper M, Nie J.F, "Formation of multiple orientation relationships of *Q* precipitates in Al–Mg–Si–Cu alloys" Scripta Materialia Vol 88 (2014) pp 53-56

96. Camero S, Puchi E.S, Gonzalez G, "Effect of 0.1% vanadium addition on precipitation behavior and mechanical properties of Al-6063 commercial alloy" Journal of Materials Science Vol 41 Issue 22 pp 7361-7373

97. Wang Y, Liao H, Wu Y, Yang J, "Effect of Si content on microstructure and mechanical properties of Al-Si-Mg alloys" Materials and Design Vol 53 (2014) pp 634-638

98. Dorward R.C, Bouvier C, " A rationalization of factors affecting strength, ductility and toughness of AA6061-type Al-Mg-Si-(Cu) alloys" Materials Science and Engineering A Vol 254 Issue 1-2 (1998) pp 33-44

99. Yildirim M, Ozyurek D, " The effects of Mg amount on the microstructure and mechanical properties of Al-Si-Mg alloys" Materials and Design Vol 51 (2013) pp 767-774

100. Dowling J.M, Martin J.W, "The influence of Mn additions on the deformation behavior of an Al-Mg-Si alloy" Acta Metallurgica Vol 24 Issue 12 (1976) pp 1147-1153

101. Busby A.K, Edwards L, Martin J.W, "Effect of aging and dispersoid content on tensile properties of Al-0.6Mg-1Si alloys" Materials Science and Technology Vol 2(4) (1986) pp 363-367

102. Jenski R.A, "Effects of Cr addition on the microstructure and mechanical behavior of 6061-T6 continuously cast and rolled redraw rod" Materials Science and Engineering A Vol 237(1) (1997) pp 52-64

103. Wagner J.A, Shenoy R.N, "The effect of copper, chromium and zirconium on the microstructural and mechanical properties of Al-Zn-Mg-Cu alloys" Metallurgical Transactions A Vol 22 Issue 11 (1991) pp 2809-2818

104. Wong K.C, Daud A.R, Jalar A, "Microhardness and tensile properties of a 6XXX alloy through minor additions of Zr" Journal of Materials Engineering and Performance Vol 18(1) (2009) pp 62-65

105. Ji S, Yang W, Gao F, Watson D, Fan Z, "Effect iron on the microstructure and mechanical property of Al–Mg–Si–Mn and Al–Mg–Si die cast alloys" Materials Science and Engineering A Vol 564 (2013) pp 130-139

106. Shabestari S.G, Moemeni H, "Effect of copper and solidification conditions on the microstructure and mechanical properties of Al–Si–Mg alloys" Journal of Materials Processing Technology Vol 153-154 (2004) pp 193-198

107. Xu C, Xiao W, Hanada S, Yamagata H, Ma C, "The effect of scandium addition on microstructure and mechanical properties of Al–Si–Mg alloy: A multi-refinement modifier" Materials Characterization Vol 110 (2015) pp 160-169

108. Sheppard T, Extrusion of aluminum alloys Kluwer academic publishers 1999

109. Smerd R, Winkler S, Salisbury C, Worswick M, Lloyd D, Finn M, "High strain rate tensile testing of automotive aluminum alloy sheet" International Journal of Impact Engineering Vol 32 Issue 1-4 (2005) pp 541-560

110. Vermolen F, Vuik K, Van der Zwaag S, "A mathematical model for the dissolution kinetics of Mg2Si-phases in Al–Mg–Si alloys during homogenization under industrial conditions" Materials Science Engineering A Vol 254 Issues 1-2 (1998) pp 13-32

111. Van de Langkruis J, Kuijpers N, Kool W, Vermolen F, Van der Zwaag S, "Modelling Mg_2Si dissolution in an AA6063 alloy during pre-heating to the extrusion temperature" Proceedings of International Aluminum Extrusion Technology Seminar, Chicago IL (2000) pp 119-124

112. Davies R, Dinsdale A, Gisby J, "MTDATA-Thermodynamic and phase equilibrium software from the National Physical Laboratory" Calphad Vol 26 Issue 2 (2002) pp 229 – 271

113. Jonas J.J, Sellars C.M, McG. Tegart W.J, "Strength and structure under hot working conditions" Metallurgical Reviews Vol 14 Issue 1 (1969) pp 1-24

114. Van de Langkruis J, Kool W, Van der Zwaag S, "Assessment of constitutive equations in modelling the hot deformability of some overaged Al-Mg-Si alloys with varying solute contents" Materials Science and Engineering A Vol 266 Issue 1-2 (1999) pp 135-145

115. Wei H, Liu G, Xiao X, Zhao H, Ding H, Kang R, "Characterization of hot deformation behavior of a new microalloyed C-Mn-Al high strength steel" Materials Science and Engineering A Vol 564 (2013) pp 140-146

116. Sellars C.M, McG. Tegart W.J, "Hot workability" International Metallurgical Reviews Vol 17 Issue 1 (1972) pp 1–24

117. Puchi E, Staia M, "Mechanical behavior of aluminum under hot working conditions" Metallurgical and Materials Transactions A Vol 26A (1995) pp 2895-2910

118. Kashyap K.T, Chandrashekar T, "Effects and mechanisms of grain refinement in aluminum alloys" Bulletin of Materials Science Vol 24 Issue 4 (2001) pp 345-353

119. Li H, Sritharan T, Lam Y.M, Leng N.Y, "Effects of processing parameters on the performance of Al grain refinement master alloys Al-Ti and Al-B in small ingots" Journal of Materials Processing Technology Vol 66 Issue 1-3 (1997) pp 253-257

120. Sritharan T, Li H, "Influence of titanium to boron ratio on the ability to grain refine aluminum-silicon alloys" Journal of Materials Processing Technology Vol 63 Issue 1-3 (1997) pp 585-589

121. Neumann G, Tuijn C, "Self-diffusion and impurity diffusion in pure metals" Handbook of experimental data (2008) Hardcover ISBN: 9781856175111, 1st Ed. Cornelis Tuijn Pergamon Materials Series 14

122. Sherby O, Goldberg A, Ruano O, "Solute-diffusion-controlled dislocation creep in pure aluminium containing 0.026 at. % Fe" Philosophical Magazine Vol 84 Issue 23 (2004) pp 2417-2434

123. Sherby O, Ruano O, "Rate-controlling processes in creep of subgrain containing aluminum materials" Materials Science and Engineering A Vol 410-411 (2005) pp 8-11

124. Rummel G, Zumkley T, Eggersmann M, Freitag K, Mehrer H, "Diffusion of implanted 3d-transition elements in aluminium. I: Temperature dependence" International Journal of Materials Research (formerly Z. Metallkd.) Vol 86 No 2 (1995) pp 122-130

125. Schmidt C.G, “Modeling the solute strengthening–deformation strengthening interaction” International Journal of Engineering Science Vol 22 Issue 8-10 (1984) pp 1055-1063

126. Jin N, Zhang H, Han Y, Wu W, Chen J, “Hot deformation behavior of 7150 aluminum alloy during compression at elevated temperature” Materials Characterization Vol 60 Issue 6 (2009) pp 530-536

127. Fujikawa S.I, “Impurity diffusion of scandium in aluminum” Defect and Diffusion Forum Vol 143-147 (1997) pp 115-120

128. Stanford N, Sabirov I, Sha G, La Fontaine A, Ringer S.P, Barnett M.R, “Effect of Al and Gd Solutes on the Strain Rate Sensitivity of Magnesium Alloys” Metallurgical and Materials Transactions A Vol 41 Issue 3 (2010) pp 734–743

129. Ozturk F, Esener E, Toros S, Picu C, “Effects of aging parameters on formability of 6061-O alloy” Materials and Design Vol 31 Issue 10 (2010) pp 4847-4852

130. Tangen S, “Deformation and annealing behavior of commercial non-heat treatable aluminum alloys: an experimental investigation” Trondheim: Norges 123 (2004) teknisk-naturvitenskapelige universitet.X 266 s: ill.

131. Olaffson P, Sandstrom S, Karlsson A, “Comparison of experimental, calculated and observed values for electrical and thermal conductivity of aluminum alloys” Journal of Materials Science Vol 32 Issue 16 (1997) pp 4383-4390

132. Humphreys F.J, “The nucleation of recrystallization at second phase particles in deformed aluminum” Acta Metallurgica Vol 25 Issue 11 (1977) pp 1323-1344

133. Forbord B, Auran L, Kang J, Lefevbre W, Hallem H, Mathinesen K, “Rapid precipitation of dispersoids during extrusion of an Al–0.91 wt.% Mn–0.13 wt.% Zr–0.17 wt.% Sc-alloy” Materials Science and Engineering A Vol 424 Issues 1-2 (2006) pp 174- 180

134. Jung I, “Extrusion failure analysis – alloy composition vs heat treatment” Automotive Partnership Canada (APC) 2014 Fall meeting CanmetMATERIALS

135. Lee D.H, Park J.H, Nam S.W, “Enhancement of mechanical properties of Al–Mg–Si alloys by means of manganese dispersoids” Materials Science and Technology Vol 15 Issue 4 (1999) pp 450-455

136. Kuna M, “Finite elements in fracture mechanics Theory-Numerics-Applications” Springer Publishing Vol 201 (2013) pp 13-20

137. Odoh D.O, Mahmoodkhani Y, Wells M, Worswick W, Mishra R.K, “Prediction of AA6063 hardness during extrusion” America’s Conference of Al alloys (AMCAA) Toronto Canada Paper No: 8978

138. Duan X, Sheppard T, “Simulation and control of microstructure evolution during hot extrusion of hard aluminum alloys” Materials Science and Engineering A, Vol. 351 (2003) pp 282-292

139. Donati L, Tomesani L, Schikorra M, Ben Khalifa N, Tekkaya A. E, “Friction model selection in FEM simulations of aluminum extrusion” International Journal of Surface Science and Engineering, Vol. 4 (2010) pp 27-41

Appendix A
Mg_2Si particle dissolution model and predictions [79]

A computer code developed using the MATLAB environment was utilized to simulate the dissolution of Mg_2Si particles in the alloy matrix during the heat up and hold period prior to deformation. The details of the Mg_2Si particle dissolution model are presented in Appendix A. Following the method proposed by Langkruis et al. [111], the dissolution model was developed based on the one dimensional diffusion law assuming a spherical coordinate system (Fick's second law):

$$\frac{\partial c_i}{\partial t} = \frac{D_i}{r^2}\frac{\partial}{\partial r}\left(r^2 \frac{\partial c_i}{\partial r}\right) \qquad (1)$$

where i=Mg, Si; D_i denotes the temperature dependent diffusion coefficient of the dissolving element in the aluminum matrix (m^2/s), c_i is the concentration of the element (wt. %), t is time (s) and r (μm) is the distance from the centre of the dissolving particle. In this model, Mg_2Si particles are assumed to be spherical with an average initial radius of r_o (Figure A1) which was determined experimentally from SEM image of alloy 4 used in this study.

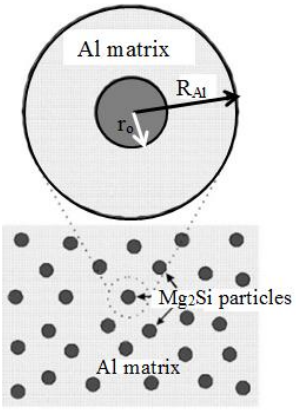

Figure A1: Schematic of an Mg_2Si spherical particle in the aluminum matrix [111]

The aluminum matrix cell is also considered to be spherical (as shown in Figure A1) with radius of R_{Al} such that the volume fraction of the Mg_2Si particles is $f_v = (r_o^3/R_{Al}^3)$. The initial Mg and Si solute concentrations in the as-homogenized condition were determined using thermodynamic

software package FACTSAGE where c_{Mg}^{init} = 0.193 wt. % and c_{Si}^{init} = 0.225 wt. %. The aluminum cell radius R_{Al} was subsequently calculated based on an average measured radius of r_o= 0.5 μm for the Mg_2Si particles in aluminum matrix. The volume fraction f_v of spherical Mg_2Si phases in Al-Mg-Si alloys homogenized at 560 ^oC has been determined as a function of heating rate during homogenization [110, 112]. For a heating rate $h_r \approx 0.1$ K/s during the homogenization process, f_v = 0.65 vol. % while Mg_2Si particle size $r_o = 0.4 \pm 0.2$ μm and R_{Al} = 2.14 μm [110]. Two main boundary conditions were applied in the model, the first being a relation between the concentration of Mg and Si at the particle/matrix interface ($r = r_p$):

$$(c_i)\, r = r_p = c_i^{sol} \qquad (2)$$

The concentration c_i^{sol} refers to the solute concentration of element *i* after time t and changes with time. We assumed a local equilibrium at the interface of the particle where these concentrations (wt. %) are related by the equation [111] :

$$(c_{Si}^{sol})^{\frac{1}{3}}.\,(c_{Mg}^{sol})^{\frac{2}{3}} = k_o \exp\left(\frac{-Q_{sol}}{RT}\right) \qquad (3)$$

k_o and Q_{sol} are the pre-exponential factor (wt. %) and activation energy (kJ/mol) for solubility respectively. The values of these parameters as well as diffusion coefficient parameters D_i were taken from [111]. The second boundary condition is applied at the matrix cell boundary ($r = R_{Al}$) where there is no flux through the boundary. Hence for both Mg and Si concentrations:

$$\left(\frac{\partial c_i}{\partial r}\right)_{r=R_{Al}} = 0 \qquad (4)$$

The particle/matrix interfacial velocity can be calculated from the local concentration gradients of Mg and Si in the aluminum matrix using conservation of mass and stoichiometry of Mg_2Si particles [111]:

$$\frac{dr_p}{dt} = \frac{D_{Si}}{c_{Si}^{p} - c_{Si}^{sol}} \left(\frac{\partial c_{Si}}{\partial r}\right)_{r=r_p} = \frac{D_{Mg}}{c_{Mg}^{p} - c_{Mg}^{sol}} \left(\frac{\partial c_{Mg}}{\partial r}\right)_{r=r_p} \qquad (5)$$

c_{Mg}^{p} and c_{Si}^{p} are the stoichiometric concentrations of Mg and Si particles respectively. The numerical algorithm is summarized as follows:

0- Discretize the matrix cell radius into small elements starting from particle radius (r_p) to cell radius (R_{Al})
1- Calculate the concentration profiles using equations (1) to (4)
2- Predict the position of particle/matrix interface at the new time step (t + Δt) using equation (5)
3- Redistribute elements such that r_p is the nodal point and use linear interpolation to approximate the concentration profile at the end of the previous time step on the new nodal point
4- Return to step 1

Steps 2 and 3 predict the Mg-Si solute content after an initial time t and time Δt afterwards.

Mg_2Si dissolution predictions

The Mg solute content after pre-heating was determined as a function of initial Mg_2Si particle size and hold time prior to deformation based on the particle dissolution model. The Mg dissolution diagrams constructed for three deformation temperatures: 400 ^{o}C, 450 ^{o}C and 500 ^{o}C at different hold times are shown in Figure A2. The initial particle size and hold time are observed to influence the solute Mg content. The initial particle size and hold time are observed to influence the solute Mg content. For specific particle size and deformation temperature, the amount of Mg solute content is observed to increase with hold time. Also, an increase in the deformation temperature is observed to increase the amount of Mg solute content that dissolves within the Al matrix.

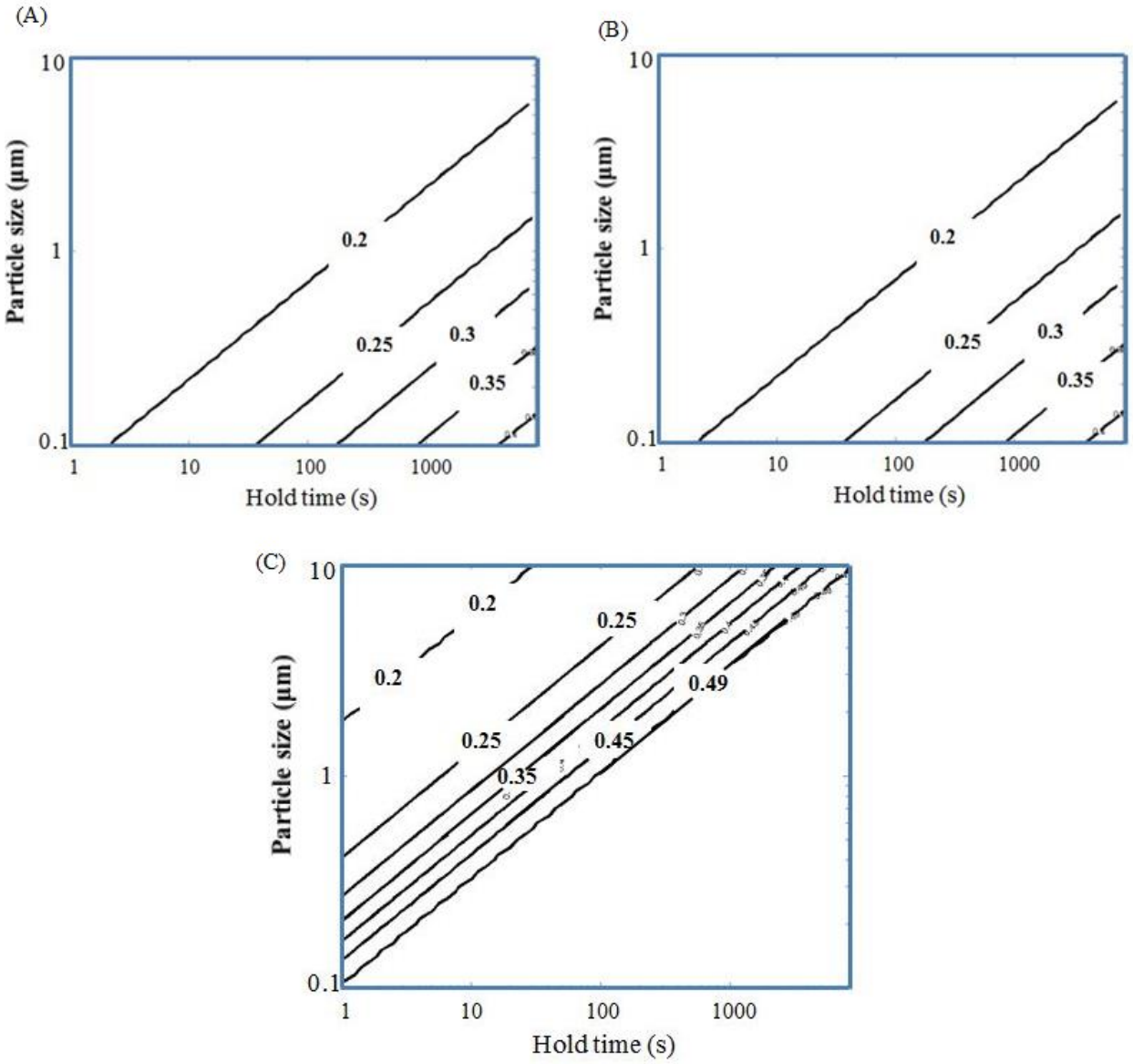

Figure A2: Mg solute content after pre-heating as a function of initial particle size and hold time (A): 400 ^{o}C, (B): 450 ^{o}C, (C): 500 ^{o}C

Figure A3 shows the Mg solute content for different hold times and deformation temperature as a function of initial particle size r_o = 0.5 μm and 0.3 μm.

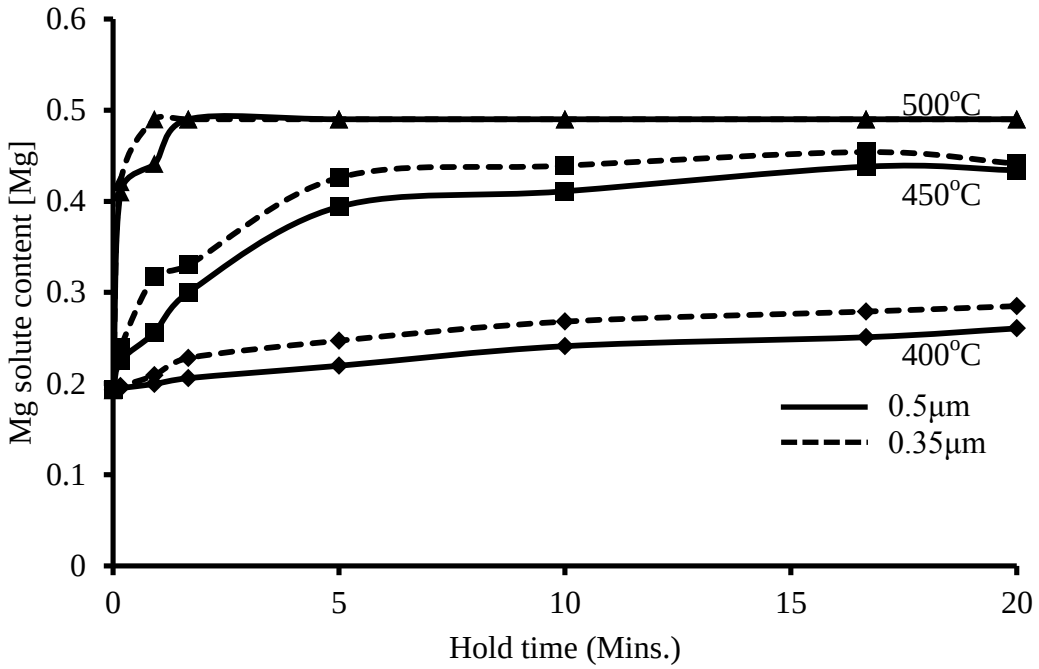

Figure A3: Model predicted Mg solute content at different temperatures for two particle sizes

Appendix B

Extrusion modeling of alloy 4 [137]

To predict the thermo-mechanical history of alloy 4 during the extrusion process, the commercial Finite Element package, DEFORM-2D was used to model the laboratory scale extrusion process. The experimental detail about the extrusion of alloy 4 sample into round bar is discussed in section 4.3.2.The model consisted of four objects to be simulated: billet, ram, container and die, as schematically shown in Figure B1.

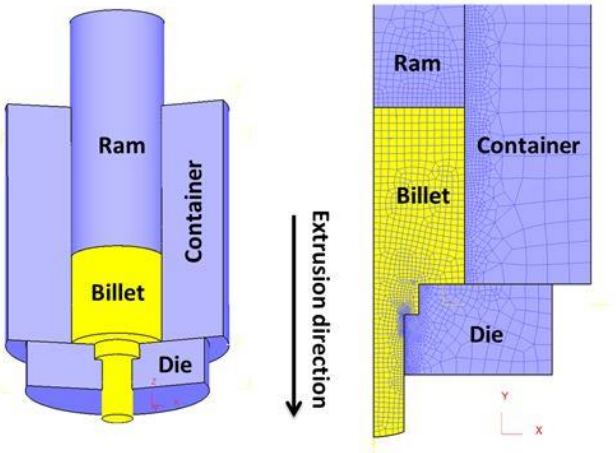

Figure B1: Schematic of the DEFORM model showing the billet being extruded into a round bar: 3D presentation of the model (left), FEM mesh used in the billet and tooling (right)

The billet material was assumed to behave as a rigid-viscoplastic material. The other objects were defined as being rigid during deformation; only the billet was involved in deformation to which the flow formulation applies. Referring to Figure B1, the geometry was modeled as a two-dimensional axisymmetric extrusion set-up with a series of four-node, tetrahedral, isoparametric elements. The effects of temperature and strain rate on the material flow stress were captured using the standard hyperbolic-sine type equation as shown in Eqn. (5.1). Alloy 1 constitutive parameters given in Table 6.1 were utilized for the modeling process. To model the friction between the billet and tooling, an interface shear factor approach was used with the equation of $f_s=mk$, where f_s is the frictional stress, k is the shear yield stress of the material and m is the

interface shear factor which is considered to be 1.0 in this simulation and represents a sticking friction condition as no lubricant was applied [138]. The heat transfer coefficient between the billet and tooling was assumed to be 25 $kWm^{-2}K^{-1}$[139]. The initial temperature of the container, die and billet were set to 500°C, 480°C and 485°C, respectively, based on thermocouple measurements during the extrusion. It was assumed that 99% of the work done during deformation was converted to heat. Using the model predicted thermo-mechanical history; the average strain rate and temperature experienced by the material at a discrete location during the extrusion process were calculated using equations (1) and (2) respectively:

$$\dot{\boldsymbol{\varepsilon}}_{avg} = \frac{\int_0^{\boldsymbol{\varepsilon}} \dot{\boldsymbol{\varepsilon}} d\boldsymbol{\varepsilon}}{\boldsymbol{\varepsilon}} \quad (1)$$

$$T_{avg} = \frac{\int \boldsymbol{T} d\boldsymbol{\varepsilon}}{\boldsymbol{\varepsilon}} \quad (2)$$

The thermomechanical history of a point 10 mm from the centre and 508 mm from the end of the extruded rod is shown in Figure B2.

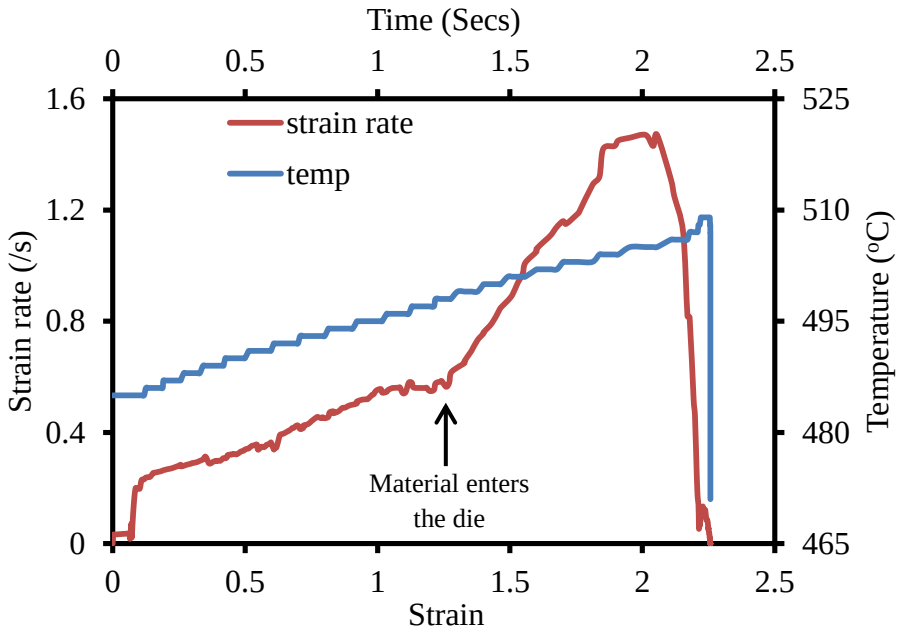

Figure B2: Thermomechanical history of a point on alloy 4: 10 mm from the centre and 508 mm from the end of the extruded rod

Figure B3 shows the comparison of the model predicted and experimental measurements of temperature and load during the extrusion of alloy 4.

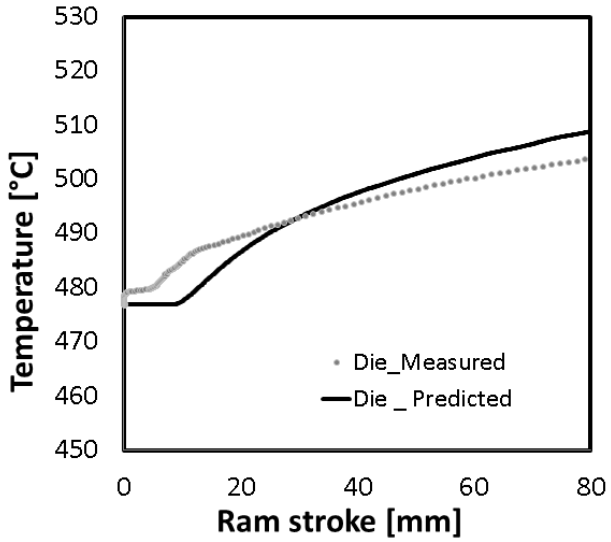

Figure B3: Comparison of DEFORM 2D predictions and experimental measurement of temperature and load during extrusion of alloy 4

As seen in Figure B3, the model utilized in determining the thermomechanical history of locations on the extrudate profile can effectively predict the flow stress behavior of alloy 4 during hot deformation processes such as extrusion.